Study on Insertion Devices as Vacuum-Ultraviolet and Soft X-ray Sources(Dissertation_全文)

AUTHOR(S):

Tanaka, Takashi

Study on Insertion Devices as Vacuum-Ultraviolet and Soft X-Ray Sources

1996

Takashi Tanaka

Acknowledgements

I would like to thank Professor N. Imanishi of Kyoto University for providing me a chance to study on insertion devices at RIKEN and for his advice. I also wish to thank Assistant Professor A. Itoh for his encouragement and helpful suggestions.

I am grateful to Professor M. Wakatani and Professor K. Yoshikawa of Kyoto University for their meaningful comments.

I am deeply indebted to Professor H. Kitamura of KEK for his continuous guidance and valuable comments throughout this study.

Thanks are due to the members of Imanishi Laboratory in Kyoto University, especially Mr. T. Awata for his continuous study on transition radiation, which was the subject of my Master's degree.

I am thankful to the members of RIKEN SPring-8 Project Team, especially the members of Beamline Group for their advice and many fruitful discussions on synchrotron radiation and its techniques.

Finally, I would like to thank my mother and brother for their encouragement and support.

Contents

Chapter 1

Introduction

Synchrotron radiation (SR) is an electromagnetic wave emitted from a charged particle moving along a curved orbit caused by the acceleration by a magnetic field, which is usually observed in a synchrotron accelerator [1]-[3]. Since this phenomenon limits the achievable energy of a charged particle, in particular, an electron accelerated in a synchrotron, it is merely an annoyance for accelerator designers. For many kinds of scientist utilizing an electromagnetic wave as a tool for research, however, SR has two major advantages over any other conventional x-ray sources, such as x-ray tubes. One is the fact that the spectral range of SR is quite broad, from far infrared to x ray [4]-[6]. Because of this characteristic, monochromatic light with an arbitrary energy can be obtained by using an appropriate monochromator. The other is the fact that the brilliance, not the total power, is much higher than conventional x-ray sources. This is due to the fact that SR has two-dimensional directionality, while radiation from an x-ray tube is isotropic.

The broad spectral range of SR means, in other words, that there are many photons to be abandoned for a researcher who uses a limited range of monochromatized photons. The unwanted photons, in turn, causes an undesirable heat load and can damage the monochromator and other optical elements. Such kind of heat load is called "unreasonable", because it is brought by the photons in the unnecessary spectral range [7]. Unfortunately, optical elements superior in the resistance to heat has not yet developed sufficiently, therefore monochromatic light sources to avoid such

an unreasonable heat load are urgently required for SR techniques. In addition, the monochromatic light should be tunable over a wide range of energies.

So-called insertion devices (IDs), in particular, undulators, are devices that meet such requirements [8]-[13]. The word "insertion" originates from the fact that the device is to be inserted in a straight section in a synchrotron or a storage ring. In general, IDs have periodic magnetic field(s), in which electrons move along a periodic trajectory. Since the radiation waves emitted from each period are superimposed, the intensity is expected to be significantly higher compared to that of bending-magnet sources. IDs are classified into two types according to the way of superimposing of the radiation emitted from each period [14].

One is a wiggler. Radiation waves emitted from each period of the trajectory are superimposed incoherently, meaning no interference between the waves. Therefore, the intensity is multiplied simply by the number of periods and of course the spectrum is not monochromatized. The reason why wigglers are utilized as SR sources is that they not only intensify the radiation but make the available (critical) energy of the spectrum higher than that obtained from the bending magnet. Nevertheless, use of wigglers never becomes a solution of the heat load problem.

The other is an undulator. Radiation waves emitted from each period are superimposed coherently, therefore intense monochromatic light is obtained. In addition, radiation emitted from the undulator has one-dimensional directionality, so that the intensity is much higher than that of bending-magnet sources. In fact, the intensity is proportional to the square of the number of periods. This is because the amplitude of radiation is multiplied by the number of periods, and the intensity is proportional to the square of the amplitude. Undulators are also classified into two types according to the trajectory of electrons inside.

One is a planar type, inside which electrons move along a sinusoidal trajectory which lies in a plane. Since the electron motion lies in the plane, the polarization of radiation emitted from the planar undulator is linear when observed on (the

undulator) axis. The other is an elliptical or a helical type, where electrons move along a trajectory rotating along the undulator axis. It is easily understood that the polarization of radiation emitted from the elliptical or the helical undulator is elliptical or circular when observed on axis.

As described later in chapter 2, the characteristics of radiation emitted from the planar undulator is affected strongly by the so-called K value, or the deflection parameter, which represents the strength of the magnetic field in an ID. When the K value is much lower than unity, only the fundamental radiation is contained in the spectrum. As the K value increases, the contribution of higher harmonics to the spectrum becomes larger. When the K value is much higher than unity, the spectrum is dominated mainly by higher harmonics and the envelope of the spectrum becomes similar to that of bending-magnet radiation. If users want to use only the fundamental radiation, all the other higher harmonics cause the unreasonable heat load. On the other hand, the spectrum of radiation emitted from the helical undulator does not contain any higher harmonics when observed on axis [15]. Therefore, one can expect the ideal utilization of undulator radiation without being annoyed by any unreasonable heat load.

Recently, many SR facilities have been proposed and some of them are now operating or under construction. The largest one is the Super Photon ring-8GeV, or the SPring-8, which stores an 8-GeV electron/positron beam for supplying the high brilliant photon beam over a wide range of energies. Other than this, SR facilities using medium-energy (1-2 GeV) electron are now planned also. In these facilities, various kinds of experiment are to be made using photons in the energy region between infrared and x ray. In particular, vacuum ultraviolet (VUV) and soft x ray (SX) are quite useful for many users. For example, solid state physics, photochemistry, atomic and molecular physics, and so on. Therefore, supplying high-brilliant photons in this energy range is one of the most important target for such SR facilities. Moreover, it is preferable to supply photons with both circular

and linear polarizations.

In an SR facility using an electron beam with an extremely high energy (large SR facility) like the SPring-8, K values much higher than unity are necessary to supply VUV and SX. In this case, use of the planar undulator is impractical since the on-axis power density is quite high due to the contribution of higher harmonics. On the other hand, helical undulators do not have such a problem. Therefore, it is reasonable to use a helical undulator for supplying VUV and SX. It should be noted, however, that only circularly-polarized radiation is available. In an SR facility using medium-energy electron (medium SR facility), VUV and SX cannot be covered by the fundamental radiation obtained from conventional undulators. In the case of the planar undulator, higher harmonics such as the 3rd, 5th and so on are available. On the other hand, radiation from the helical undulator does not contain higher harmonics when observed on axis, which becomes an obstacle to obtain higher-energy photons. In this case, only linearly-polarized radiation is available. The above discussions can be summarized as follows:

Table 1.1. Available polarization of VUV and SX in SR facilities.

SR facility	Polarization	
	Circular	Linear
Large	○	×
Medium	×	○

In this thesis, two novel IDs are proposed. One is a "figure-8" undulator to obtain linearly-polarized radiation with a low on-axis power density. Using this device, linearly-polarized VUV and SX can be available in the large SR facility. The other is a "rhombus" undulator to obtain higher harmonics with a circular polarization. Using higher harmonics obtained from this device, circularly-polarized VUV and SX will be available in a medium SR facility. Here, the words "figure-8" and "rhombus" represent the electron orbit in each device, projected on the transverse plane. In

order to investigate the performances, the figure-8 and rhombus undulators are compared to ordinary undulators. In addition, various characteristics of radiation are investigated for the effective utilization of the proposed IDs. It should be noted that all equations in this thesis are written in MKSA units.

In chapter 2, general theories of IDs are described in order to clarify disadvantages of ordinary IDs. Equations on radiation emitted from electrons moving in an ID with an arbitrary field are derived. In addition, characteristics of undulator radiation such as the power density, spectrum, polarization, and so on are investigated.

In chapter 3, the "figure-8" undulator is proposed. A detailed description is given of the principle and the equations on radiation emitted from the figure-8 undulator. In order to investigate the performances of the figure-8 undulator, a comparison is made between the ordinary planar undulator and the figure-8 undulator with respect to the power density and the photon flux density.

In chapter 4, various characteristics of figure-8-undulator radiation, such as the polarization, the electric field and the K dependence are investigated.

In chapter 5, the design of the figure-8 undulator is described. In order to install an ID in the storage ring, the structure of the ID should be a "planar" one, such that the magnet arrays exist only above and below the undulator axis. Taking this fact into account, the structure of the figure-8 undulator is determined. In addition, the size of the magnet block is discussed with respect to the spectral performances such as the brilliance and the heat load or the on-axis power density. Some effects of the figure-8-undulator magnetic field on the storage-ring operation are also discussed.

In chapter 6, the "rhombus" undulator is proposed. Discussions are made on various IDs to supply circularly-polarized VUV and SX in the medium SR facility. After that, the principle of the rhombus undulator is given and the equations on radiation are derived. By comparing with ordinary circularly-polarized IDs, the performances of the rhombus undulator are investigated with respect to the degree of polarization and the photon flux density. In addition, the design such as the

magnet structure and the size of the magnet block are discussed.

In chapter 7, various characteristics of rhombus-undulator radiation are investigated for the effective utilization of rhombus-undulator radiation.

A summary of this thesis is given in chapter 8.

Chapter 2

General Theory of an Insertion Device

2.1 Introduction

The so-called insertion devices (IDs) are apparatus inside which periodic magnetic fields are generated and an electron moves along a periodic trajectory. The emitted waves at various positions of the trajectory are superimposed, which results in much higher intensity of radiation. In general, IDs are classified into two types according to whether the superposition of waves is coherent or incoherent. The former is called an undulator and the latter a wiggler.

In most experiments using SR, what is necessary for users is that the brilliance of the photon beam, not the total flux, is high. The brilliance (usually expressed as photons/sec/mrad^2/mm^2/0.1%B.W.) is a quantity representing the photon flux per unit phase space area, i. e., per unit source area per unit solid angle into which the radiation is emitted. In order to obtain the high brilliance, two approaches are considered. One is to improve the quality of the electron beam and the other is to improve the quality of the photon beam.

Improving the electron beam means the improvement of the storage ring. In fact, the recent progress of the accelerator technology has made it possible to construct a quite-low-emittance storage ring, resulting in the quite high brilliance of SR.

Improving the photon beam means the improvement of the light source. There

are three factors which determine the quality of the light source: the angular divergence, the photon flux density and the monochromatization with a tunability. IDs, especially undulators, have excellent characteristics with respect to these factors. First, the angular divergence of the radiation from the undulator is proportional to N^{-1}, where N is the number of periods. Second, the photon flux density is proportional to N^2. Third, the radiation is monochromatized with the peak width of N^{-1} and it is tunable by changing the strength of the magnetic field(s) inside. From these facts, we can say that undulators with a large number of periods are preferable for obtaining the high brilliance to bending-magnet sources.

In this chapter, an outline of IDs as SR sources is described and general equations on undulator radiation are derived, which are the basis of the calculation in later chapters. In addition, two types of ID, planar and helical undulators, are investigated in order to clarify the status of the ordinary IDs.

2.2 Radiation from a relativistic electron

2.2.1 Radiation cone

Let us consider the emission of photons from an electron moving with a relativistic velocity v. Let $p^i = (\varepsilon/c, \boldsymbol{p})$ be the 4-dimensional momentum of the photon observed in the rest frame and $p^{i\prime} = (\varepsilon'/c, \boldsymbol{p}')$ in the laboratory frame, as shown in Figs. 2.1 (a) and (b). θ and θ' are the angles between the direction of the electron motion and that of the emitted photon observed in the rest and laboratory frames, respectively. p^i and $p^{i\prime}$ associate with each other by the relations

$$\varepsilon' = \gamma(\varepsilon + \beta c p_{\parallel}), \tag{2.1}$$

$$p'_{\parallel} = \gamma\left(p_{\parallel} + \beta\frac{\varepsilon}{c}\right), \tag{2.2}$$

$$p'_{\perp} = p_{\perp}, \tag{2.3}$$

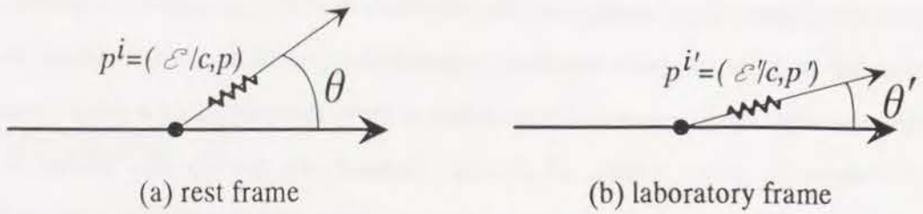

(a) rest frame (b) laboratory frame

Figure 2.1. Observation of photons emitted from a relativistic electron in the (a) rest and (b) laboratory frames.

where subscripts $\parallel$ and $\perp$ show the components parallel and vertical to the direction of the electron motion, respectively. β is the relative velocity of the electron, or $\beta = v/c$. γ is the Lorentz factor of the electron defined by

$$\gamma = \frac{E}{mc^2}, \tag{2.4}$$

where E is the energy of the electron and m the electron rest mass (0.511MeV). θ' is calculated as

$$\begin{aligned} \tan\theta' &= \frac{p'_\perp}{p'_{\parallel'}} \\ &= \frac{1}{\gamma}\frac{p_\perp}{p_\parallel + \beta\mathcal{E}/c} \\ &= \frac{1}{\gamma}\frac{\sin\theta}{\cos\theta + \beta}. \end{aligned} \tag{2.5}$$

Since the velocity is relativistic, β is almost close to unity. Therefore, it is found from equation (2.5) that the radiation power emitted from the relativistic electron is condensed to a narrow forward cone with the vertical angle of $1/\gamma$. This is an important feature of radiation from the relativistic electron and applies not only to SR but to other radiation processes such as Bremsstrahlung, Cherenkov radiation and transition radiation.

2.2.2 Radiation field

Let us consider a relativistic electron moving along an arbitrary trajectory, as shown in Fig. 2.2. $\boldsymbol{R}_0$ and $\boldsymbol{r}$ are the vectors directing from the origin to an observer and to the moving electron, respectively. $\boldsymbol{R}$ is the vector directing from $\boldsymbol{r}$ to $\boldsymbol{R}_0$, or $\boldsymbol{R} = \boldsymbol{R}_0 - \boldsymbol{r}$. $\boldsymbol{n}$ is a unit vector in the direction of $\boldsymbol{R}$. The potential generated by the electron is known as the Liénard-Wiecherd potential given by

$$\phi(t) = \frac{1}{4\pi\epsilon_0}\frac{e}{R(t') - \boldsymbol{R}(t')\cdot\boldsymbol{v}(t')/c}, \tag{2.6}$$

$$\boldsymbol{A}(t) = \frac{\mu_0}{4\pi}\frac{e\boldsymbol{v}(t')}{R(t') - \boldsymbol{R}(t')\cdot\boldsymbol{v}(t')/c}, \tag{2.7}$$

where ϕ and $\boldsymbol{A}$ represent the scalar and vector potentials, respectively. t' is the so-called retarded time and associates with t by the relation

$$t' + R(t')/c = t. \tag{2.8}$$

It is well known that the electric and magnetic fields are associated with the scalar and vector potentials by the relations

$$\boldsymbol{E} = -\nabla\phi - \frac{\partial\boldsymbol{A}}{\partial t}, \tag{2.9}$$

$$\boldsymbol{B} = \nabla\times\boldsymbol{A}. \tag{2.10}$$

Substituting equations (2.6) and (2.7) into (2.9) and (2.10), we obtain the electric and magnetic fields

$$\boldsymbol{E} = \boldsymbol{E}_v + \boldsymbol{E}_a, \tag{2.11}$$

$$\boldsymbol{E}_v = \frac{e}{4\pi\epsilon_0}\left[\frac{1-\beta^2}{R^2}\frac{\boldsymbol{n}-\boldsymbol{\beta}}{(1-\boldsymbol{n}\cdot\boldsymbol{\beta})^3}\right]_{\text{ret}}, \tag{2.12}$$

$$\boldsymbol{E}_a = \frac{e}{4\pi\epsilon_0 c}\left[\frac{\boldsymbol{n}\times[(\boldsymbol{n}-\boldsymbol{\beta})\times\dot{\boldsymbol{\beta}}]}{R(1-\boldsymbol{n}\cdot\boldsymbol{\beta})^3}\right]_{\text{ret}}, \tag{2.13}$$

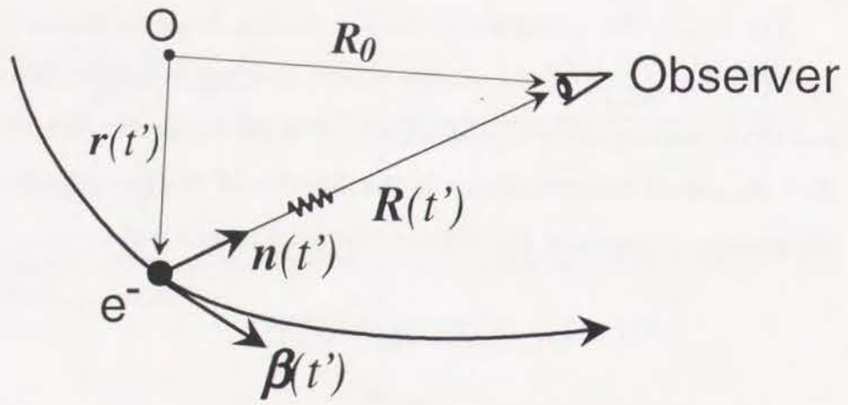

Figure 2.2. Relativistic electron moving along an arbitrary trajectory.

$$\boldsymbol{B}(t) = \frac{1}{c}\boldsymbol{n}(t')\times\boldsymbol{E}(t), \tag{2.14}$$

where the square brackets with subscript "ret" mean that the quantity in the brackets should be evaluated at the retarded time. $\boldsymbol{E}$ can be divided into "velocity field", $\boldsymbol{E}_v$, which is independent of acceleration, and "acceleration field", $\boldsymbol{E}_a$, which depends linearly on $\dot{\boldsymbol{\beta}}$. The velocity field is essentially a static field falling off as R^{-2}, while the acceleration field is a typical radiation field varying as R^{-1}. In the far-field limit of R being infinity, the velocity field, $\boldsymbol{E}_v$, can be neglected. In addition, the equation (2.8) is simplified to

$$t' = t + \boldsymbol{n}\cdot\boldsymbol{r}(t')/c - \boldsymbol{n}\cdot\boldsymbol{R}_0/c. \tag{2.15}$$

From the above equation, we obtain

$$\frac{dt}{dt'} = 1 - \boldsymbol{n}\cdot\boldsymbol{\beta}. \tag{2.16}$$

2.2.3 Angular distribution of radiation power

The radiated power is calculated from the Poynting vector. The Poynting vector is given by

$$\boldsymbol{S} = \boldsymbol{E}\times\boldsymbol{H}. \tag{2.17}$$

From equation (2.14), we obtain

$$\boldsymbol{S}(t) = \epsilon_0 c|\boldsymbol{E}(t)|^2\boldsymbol{n}. \tag{2.18}$$

The power per unit solid angle per unit time is calculated as

$$\begin{aligned}\frac{dW(t)}{d\Omega} &= R^2\boldsymbol{S}\cdot\boldsymbol{n} \\ &= \epsilon_0 c|\boldsymbol{F}(t)|^2,\end{aligned} \tag{2.19}$$

with

$$\boldsymbol{F}(t) = R\boldsymbol{E}(t). \tag{2.20}$$

The total power per unit solid angle is the time integral of equation (2.19) calculated as

$$\begin{aligned}\frac{dP}{d\Omega} &= \int_{-\infty}^{\infty}\frac{dW(t)}{dt}dt, \\ &= \epsilon_0 c\int_{-\infty}^{\infty}|\boldsymbol{F}(t)|^2 dt.\end{aligned} \tag{2.21}$$

2.2.4 Frequency spectrum of radiation

The total power represented by equation (2.21) can be expressed alternatively as an integral over a frequency spectrum by use of Fourier transformation. We introduce the Fourier transformation $\boldsymbol{F}_\omega$ of $\boldsymbol{F}(t)$

$$\boldsymbol{F}_\omega = \int_{-\infty}^{\infty}\boldsymbol{F}(t)\,\mathrm{e}^{-i\omega t}dt, \tag{2.22}$$

and its inverse

$$\boldsymbol{F}(t) = \frac{1}{2\pi}\int_{-\infty}^{\infty} \boldsymbol{F}_\omega \, \mathrm{e}^{i\omega t} d\omega. \tag{2.23}$$

Then equation (2.21) is rewritten as

$$\frac{dP}{d\Omega} = \frac{\epsilon_0 c}{2\pi}\int_{-\infty}^{\infty} |\boldsymbol{F}_\omega|^2 d\omega = \frac{\epsilon_0 c}{\pi}\int_{0}^{\infty} |\boldsymbol{F}_\omega|^2 d\omega. \tag{2.24}$$

Therefore, the power per unit solid angle per unit frequency interval (photon flux density) is calculated as

$$\frac{d^2P}{d\Omega d\omega} = \frac{\epsilon_0 c}{\pi}|\boldsymbol{F}_\omega|^2. \tag{2.25}$$

2.2.5 Radiation from an electron with a periodic motion

When an electron moves periodically with a frequency of ω, photons with a frequency of ω are radiated from the electron. If the energy of the electron is relativistic, the frequency of the photon observed in the laboratory frame is shifted to ω' due to the Doppler effect [16]

$$\omega' = \omega \frac{\gamma^{-1}}{1 - \frac{v}{c}\cos\alpha}, \tag{2.26}$$

where v is the speed of the electron and α the angle between the direction of the electron motion and the observer. If $\alpha = 0$, equation (2.26) is rewritten as

$$\omega' = 2\gamma\omega. \tag{2.27}$$

Since γ is much larger than unity, the frequency of radiation observed in the laboratory frame is much higher than that observed in the rest frame.

If the electron motion is completely a harmonic oscillation, only the photons with a frequency of ω' are observed. If not so, but the motion is periodic, then not only photons with a frequency of ω' but photons with frequencies of $2\omega', 3\omega', \ldots, n\omega'$ are observed. Here, n is an integer. The photons with frequencies of $2\omega', 3\omega', \ldots, n\omega'$ are called higher harmonics.

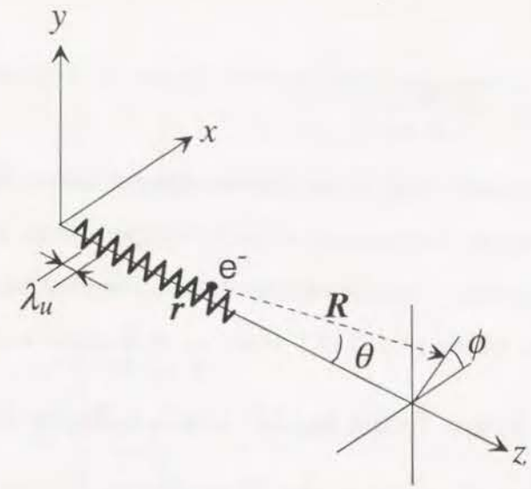

Figure 2.3. ID with arbitrary fields.

2.3 Radiation from an ID with arbitrary field

Let us consider an ID with arbitrary but periodic fields. The coordinate is shown in Fig. 2.3. $\boldsymbol{r}$ is the position of the electron, $\boldsymbol{R}$ the vector from $\boldsymbol{r}$ to the observer, θ the angle between $\boldsymbol{R}$ and the z axis, ϕ the azimuth relative to the x-z plane and λ_u the period length of the ID. In this device, electrons move along an arbitrary but periodic trajectory.

2.3.1 Wavelength of the fundamental radiation from an ID

In the rest frame of the electron, the period length of the field contracts by a factor of γ^{-1} due to the Lorentz contraction. Therefore, the frequency of the electron motion is

$$\omega_0 = 2\pi\gamma v_z/\lambda_u, \tag{2.28}$$

where v_z is the z component of the velocity. The frequency observed in the laboratory frame, ω_1, is calculated by using equation (2.26) as

$$\omega_1 = \frac{2\pi v_z/\lambda_u}{1-\beta_z\cos\theta}, \tag{2.29}$$

where β_z is the z component of the relative velocity. Since the electron is observed to radiate photons with a frequency of ω_1 in the laboratory frame, we can say that ω_1 is also a frequency of an apparent motion of the electron, i. e., the electron is observed to move with a period of $T = 2\pi/\omega_1$ in the laboratory frame.

2.3.2 Radiation from an ID with infinite periods

If the number of periods of the ID is infinite, $\boldsymbol{F}$(t) can be expanded into a Fourier series as

$$\boldsymbol{F}(t) = \sum_{k=-\infty}^{\infty} \boldsymbol{F}_k \, \mathrm{e}^{i\omega_1 kt}, \tag{2.30}$$

$$\boldsymbol{F}_k = \frac{1}{T}\int_0^T \boldsymbol{F}(t)\, \mathrm{e}^{-i\omega_1 kt} dt, \tag{2.31}$$

where ω_1 is the frequency of the apparent motion of the electron, given by equation (2.29) and $T = 2\pi/\omega_1$. Substituting equations (2.20) and (2.13), equation (2.31) is rewritten as

$$\boldsymbol{F}_k = \frac{1}{T}\frac{e}{4\pi\epsilon_0 c}\int_0^T \left[\frac{\boldsymbol{n}\times([\boldsymbol{n}-\boldsymbol{\beta}]\times\dot{\boldsymbol{\beta}})}{(1-\boldsymbol{n}\cdot\boldsymbol{\beta})^3}\right]_{t'} \mathrm{e}^{-i\omega_1 kt} dt. \tag{2.32}$$

Using equations (2.15) and (2.16), $\boldsymbol{F}_k$ is calculated as follows

$$\begin{aligned}
\boldsymbol{F}_k &= \frac{1}{T}\frac{e}{4\pi\epsilon_0 c}\int_0^{T'} \left[\frac{\boldsymbol{n}\times([\boldsymbol{n}-\boldsymbol{\beta}]\times\dot{\boldsymbol{\beta}})}{(1-\boldsymbol{n}\cdot\boldsymbol{\beta})^2}\right]_{t'} \mathrm{e}^{-i\omega_1 kt} dt' \\
&= \frac{1}{T}\frac{e}{4\pi\epsilon_0 c}\int_0^{T'} \frac{d}{dt'}\left[\frac{\boldsymbol{n}\times(\boldsymbol{n}\times\boldsymbol{\beta})}{1-\boldsymbol{n}\cdot\boldsymbol{\beta}}\right]_{t'} \mathrm{e}^{-i\omega_1 k(t'+R_0/c-\boldsymbol{n}\cdot\boldsymbol{r}(t')/c} dt' \\
&= \frac{ik\omega_1^2 e}{8\pi^2\epsilon_0 c}\, \mathrm{e}^{-i\omega_1 kR_0/c}\boldsymbol{n}\times(\boldsymbol{n}\times\boldsymbol{Q}_k),
\end{aligned} \tag{2.33}$$

with

$$\boldsymbol{Q}_k = \int_0^{T'} \boldsymbol{\beta}(t')\, \mathrm{e}^{-i\omega_1 k(t'-\boldsymbol{n}\cdot\boldsymbol{r}(t')/c)}. \tag{2.34}$$

T' is the period of the electron motion observed in the rest frame and calculated as $T' = 2\pi/\omega_0$.

In this case, photons with energies of only $\hbar\omega_1$, $2\hbar\omega_1$, $3\hbar\omega_1, \ldots,$ $n\hbar\omega_1$, are observed as described in section 2.2.5.

The radiated power per unit period is calculated as

$$\begin{aligned}
\frac{dP}{d\Omega} &= \epsilon_0 c\int_0^T |\boldsymbol{F}(t)|^2 dt \\
&= \epsilon_0 c\int_0^T \sum_m\sum_n F_m F_n\, \mathrm{e}^{i\omega_1(m+n)t} dt \\
&= \epsilon_0 cT\sum_{n=-\infty}^{\infty} |\boldsymbol{F}_n|^2.
\end{aligned} \tag{2.35}$$

2.3.3 Radiation from an ID with finite periods

Next, the case is considered that the number of periods is not infinite but a finite number of N. In this case, the method of Fourier expansion cannot be used to calculate the spectrum, since the electron motion is not completely periodic. We should calculate $\boldsymbol{F}_\omega$ to calculate the spectrum. $\boldsymbol{F}_\omega$ is calculated as follows

$$\begin{aligned}
\boldsymbol{F}_\omega &= \int_0^{NT} \boldsymbol{F}(t)\, \mathrm{e}^{-i\omega t} dt \\
&= \int_0^{NT} \left[\sum_{k=-\infty}^{\infty} \boldsymbol{F}_k\, \mathrm{e}^{i\omega_1 kt}\right] \mathrm{e}^{-i\omega t} dt \\
&= \sum_{k=-\infty}^{\infty} \boldsymbol{F}_k \frac{\exp[i(k-\omega/\omega_1)\pi N]-1}{i(k\omega_1-\omega)}.
\end{aligned} \tag{2.36}$$

Substituting equation (2.36) into (2.25), we obtain the photon flux density

$$\begin{aligned}
\frac{d^2P}{d\Omega d\omega} &= \frac{4\epsilon_0 c}{\pi\omega_1^2}\sin^2\frac{\pi N\omega}{\omega_1}\times \\
&\quad \left[\sum_{k=-\infty}^{\infty}\frac{|\boldsymbol{F}_k|^2}{(\omega/\omega_1-k)^2} + \sum_{k\neq j}\frac{\boldsymbol{F}_k\boldsymbol{F}_j^*}{(\omega/\omega_1-k)(\omega/\omega_1-j)}\right].
\end{aligned} \tag{2.37}$$

If N is sufficiently large, the second term in equation (2.37) can be neglected compared to the first one. In this case, equation (2.37) is rewritten as

$$\frac{d^2P}{d\Omega d\omega} = \sum_{k=-\infty}^{\infty} \frac{d^2P_k}{d\Omega d\omega}, \tag{2.38}$$

$$\frac{d^2P_k}{d\Omega d\omega} = \frac{4\pi\epsilon_0 c}{\omega_1^2} N^2 |\boldsymbol{F}_k|^2 P_N^2, \tag{2.39}$$

$$P_N = \frac{\sin \pi N\omega/\omega_1}{\pi N(\omega/\omega_1 - k)}. \tag{2.40}$$

As well as the infinite-period case, the spectrum is expanded into harmonics. Since ω is contained only in the term P_N, P_N determines the shape of the spectrum. The intensity of each harmonic is proportional to $|\boldsymbol{F}_k|^2$ calculated by equation (2.33).

2.3.4 Flux and power density for two polarization components

The electric field can be decomposed into two polarization components. We introduce two unit vectors $\boldsymbol{m}_\parallel$ and $\boldsymbol{m}_\perp$. The triad $\boldsymbol{m}_\parallel$, $\boldsymbol{m}_\perp$ and $\boldsymbol{n}$ forms an orthogonal set. Choosing $\boldsymbol{m}_\parallel$ to lie in the horizontal plane as shown in Fig. 2.4, we have

$$\boldsymbol{n} = (\theta\cos\phi,\ \ \theta\sin\phi,\ \ \cos\theta), \tag{2.41}$$

$$\boldsymbol{m}_\parallel = (1,\ \ 0,\ \ -\theta\cos\phi), \tag{2.42}$$

$$\boldsymbol{m}_\perp = (0,\ \ 1,\ \ -\theta\sin\phi). \tag{2.43}$$

Here, we have used the approximation that θ is much smaller than unity. Decomposing $\boldsymbol{F}(t)$ into two polarization components, we have

$$F_{\parallel,\perp}(t) = \frac{e}{4\pi\epsilon_0} \frac{(\theta_{x,y} - \beta_{x,y})(\boldsymbol{n}\cdot\dot{\boldsymbol{\beta}}) - (1 - \boldsymbol{n}\cdot\boldsymbol{\beta})\dot{\beta_{x,y}}}{(1 - \boldsymbol{n}\cdot\boldsymbol{\beta})^3}, \tag{2.44}$$

where $F_{\parallel,\perp}(t)$ represent the components parallel to $\boldsymbol{m}_{\parallel,\perp}$, respectively. $\theta_{x,y}$ are horizontal and vertical observation angles defined as

$$\theta_x = \theta\cos\phi, \tag{2.45}$$

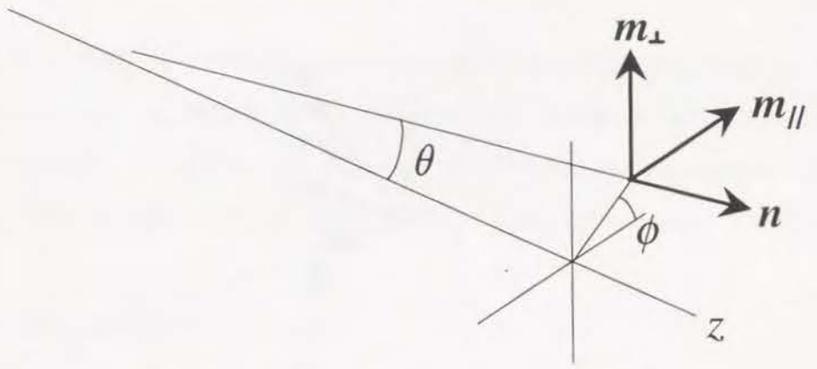

Figure 2.4. Two polarization vectors.

$$\theta_y = \theta\sin\phi. \tag{2.46}$$

From equation (2.21), the power radiated per unit solid angle (power density) is calculated as

$$\frac{dP_{\parallel,\perp}}{d\Omega} = \frac{e^2}{16\pi^2\epsilon_0 c}\int dt' \frac{[(\theta_{x,y} - \beta_{x,y})(\boldsymbol{n}\cdot\dot{\boldsymbol{\beta}}) - (1 - \boldsymbol{n}\cdot\boldsymbol{\beta})\,\dot{\beta_{x,y}}]^2}{(1 - \boldsymbol{n}\cdot\boldsymbol{\beta})^5}. \tag{2.47}$$

As well as $\boldsymbol{F}(t)$, $\boldsymbol{F}_k$ is also decomposed. Using the relation

$$\boldsymbol{a}\times(\boldsymbol{b}\times\boldsymbol{c}) = (\boldsymbol{a}\cdot\boldsymbol{c})\boldsymbol{b} - (\boldsymbol{a}\cdot\boldsymbol{b})\boldsymbol{c}, \tag{2.48}$$

we have

$$F_{k\parallel,\perp} = \frac{ik\omega_1^2 e}{8\pi^2\epsilon_0 c}\, e^{-i\omega_1 kR_0/c}(-Q_{kx,ky} + Q_{kz}\theta_{x,y}). \tag{2.49}$$

Substituting into equation (2.39), we obtain the photon flux density for each polarization component

$$\frac{d^2P_{\parallel,\perp}}{d\Omega d\omega} = \frac{\gamma^2 e^2 N^2}{4\pi\epsilon_0 c}|f_{x,y}|^2, \tag{2.50}$$

with

$$f_{x,y} = -i\, e^{i\omega_1 kR_0/c}\frac{4\pi\epsilon_0 c}{\gamma\omega_1 e} P_N F_{k\parallel,\perp}. \tag{2.51}$$

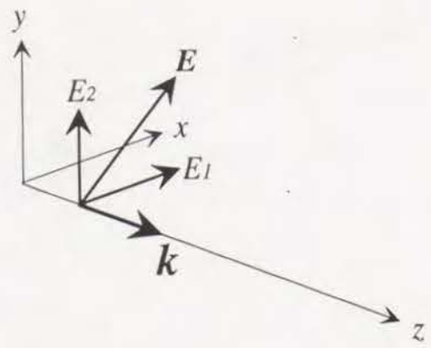

Figure 2.5. Plane electromagnetic wave propagating in the z direction.

2.3.5 Linear and circular polarization

Let us consider a plane electromagnetic wave propagating in the z direction as shown in Fig. 2.5. In this case, the electric field is given by

$$\boldsymbol{E} = (E_1\boldsymbol{e}_x + E_2\boldsymbol{e}_y)\,\mathrm{e}^{i\omega t - i\boldsymbol{k}\cdot\boldsymbol{x}}, \tag{2.52}$$

where $\boldsymbol{e}_{x,y}$ are the unit vectors in the x and y directions, $\boldsymbol{k}$ the wave vector and ω the frequency. In order to consider the phase difference between waves of different polarizations, the amplitudes E_1 and E_2 are assumed to be complex.

When $E_1 = iE_2 = E_0$, where E_0 is real, equation (2.52) is rewritten as

$$\boldsymbol{E} = E_0(\boldsymbol{e}_x - i\boldsymbol{e}_y)\,\mathrm{e}^{i\omega t - i\boldsymbol{k}\cdot\boldsymbol{x}}. \tag{2.53}$$

Taking the real part of equation (2.53), the components of the actual electric field are obtained as

$$E_x(\boldsymbol{x}, t) = E_0\cos(\omega t - kz), \tag{2.54}$$

$$E_y(\boldsymbol{x}, t) = E_0\sin(\omega t - kz). \tag{2.55}$$

At a fixed point in space, the fields expressed by equations (2.54) and (2.55) are such that the electric vector is constant in magnitude, but sweeps around in a circle

at a frequency ω. Such an electromagnetic wave is called circularly polarized. In particular, the rotation is counter-clockwise when the observer is facing into the oncoming wave, therefore the wave is called left-handed circularly polarized. On the contrary, if $E_1 = -iE_2 = E_0$, then the wave is called right-handed circularly polarized.

Equation (2.53) can be rewritten as

$$\boldsymbol{E} = E_0\boldsymbol{e}_x\,\mathrm{e}^{i(\omega t - \boldsymbol{k}\cdot\boldsymbol{x})} + E_0\boldsymbol{e}_y\,\mathrm{e}^{i(\omega t - \boldsymbol{k}\cdot\boldsymbol{x}t - \pi/2)}. \tag{2.56}$$

Therefore, a circularly-polarized wave is regarded as the superposition of two linearly-polarized waves with the relative phase difference of $\pi/2$.

Next, let us consider the case that $E_1 = E_2^* = E_{0r} + iE_{0i}$, where E_{0r} and E_{0i} are real. The electric field is calculated as

$$\boldsymbol{E} = 2E_{0r}(\boldsymbol{e}_x + \boldsymbol{e}_y)\,\mathrm{e}^{i(\omega t - \boldsymbol{k}\cdot\boldsymbol{x})}. \tag{2.57}$$

This is obviously a linearly-polarized wave. Therefore, the linear polarization is considered as the superposition of two circular polarizations with different helicities. In general, an arbitrary polarization is considered as the superposition of two linear or circular polarizations.

2.3.6 Stokes parameters and degree of polarization

The polarization content of a plane electromagnetic wave is known if it can be written in the form of equation (2.52) with known coefficients (E_1, E_2). Useful vehicles for determining the polarization state of an electromagnetic wave are the so-called Stokes parameters, proposed by G. G. Stokes in 1852. These parameters are quadratic in the field strength and can be determined only through the intensity measurements.

The Stokes parameters are given by

$$
\begin{aligned}
s_0 &= |\boldsymbol{e}_x \cdot \boldsymbol{E}|^2 + |\boldsymbol{e}_y \cdot \boldsymbol{E}|^2, \\
s_1 &= |\boldsymbol{e}_x \cdot \boldsymbol{E}|^2 - |\boldsymbol{e}_y \cdot \boldsymbol{E}|^2, \\
s_2 &= 2\mathrm{Re}[(\boldsymbol{e}_x \cdot \boldsymbol{E})^*(\boldsymbol{e}_y \cdot \boldsymbol{E})], \\
s_3 &= 2\mathrm{Im}[(\boldsymbol{e}_x \cdot \boldsymbol{E})^*(\boldsymbol{e}_y \cdot \boldsymbol{E})].
\end{aligned} \tag{2.58}
$$

s_2 and s_3 can be rewritten as

$$
s_2 = |\boldsymbol{e}_+ \cdot \boldsymbol{E}|^2 - |\boldsymbol{e}_- \cdot \boldsymbol{E}|^2, \tag{2.59}
$$

$$
s_3 = |\boldsymbol{e}_l \cdot \boldsymbol{E}|^2 - |\boldsymbol{e}_r \cdot \boldsymbol{E}|^2, \tag{2.60}
$$

with

$$
\boldsymbol{e}_\pm = \frac{\boldsymbol{e}_x \pm \boldsymbol{e}_y}{\sqrt{2}}, \tag{2.61}
$$

and

$$
\boldsymbol{e}_{l,r} = \frac{\boldsymbol{e}_x \pm i\boldsymbol{e}_y}{\sqrt{2}}. \tag{2.62}
$$

It is found from above equations that $\boldsymbol{e}_\pm$ are the $\pm 45°$-linear polarization vectors and that $\boldsymbol{e}_{l,r}$ are the left- and right-handed circular polarization vectors. Therefore, the meanings of the Stokes parameters are considered to be

$$
\begin{aligned}
s_0 &= I_x + I_y, \\
s_1 &= I_x - I_y, \\
s_2 &= I_+ - I_-, \\
s_3 &= I_l - I_r,
\end{aligned} \tag{2.63}
$$

where $I_{x,y}$ are the intensities of x- and y-linear polarizations, $I_\pm$ the intensities of $\pm 45°$-linear polarizations and $I_{r,l}$ the intensities of the left- and right-handed circular polarizations.

The degree of linear polarization, P_L, is defined as

$$
P_L = s_1/s_0. \tag{2.64}
$$

The degree of circular polarization, P_C, is defined as

$$
P_C = s_3/s_0. \tag{2.65}
$$

The meanings of these values are clear from interpretations of the Stokes parameters, (2.63). Using $f_{x,y}$ given by equation (2.51), $P_{L,C}$ are calculated as

$$
P_L = \frac{|f_x|^2 - |f_y|^2}{|f_x|^2 + |f_y|^2}, \tag{2.66}
$$

$$
P_C = \frac{2\mathrm{Im}(f_x^* f_y)}{|f_x|^2 + |f_y|^2}. \tag{2.67}
$$

2.4 Radiation from a planar undulator

In the previous section, we considered the radiation from an ID with arbitrary field. Using equations (2.47) and (2.50), we can investigate the properties of radiation from any types of ID. First, we consider a planar undulator, which is the most popular ID.

2.4.1 Configuration of magnets

Figure 2.6 shows a schematic cross section of a planar undulator. This configuration of magnets is called a Halbach type, because it was first proposed by Halbach [17]-[20]. Each period contains four magnet blocks. The direction of magnetization of each block is rotated by $\pi/2$ when it goes from one block to the next. Two-dimensional calculation shows that the magnetic field in this device is given by

$$
\begin{aligned}
B_z - iB_y &= 2iB_r \sum_{\mu=0} \sin[nk_u(z+iy)]\, \mathrm{e}^{-n\pi g/\lambda_u} \\
&\quad \times \frac{\sin(n\pi/4)}{n\pi/4}(1 - \mathrm{e}^{-2n\pi L/\lambda_u}),
\end{aligned} \tag{2.68}
$$

where B_r is the remanent field of each magnet and

$$
n = 1 + 4\mu, \tag{2.69}
$$

$$
k_u = \frac{2\pi}{\lambda_u}. \tag{2.70}
$$

On axis, equation (2.68) is reduced to

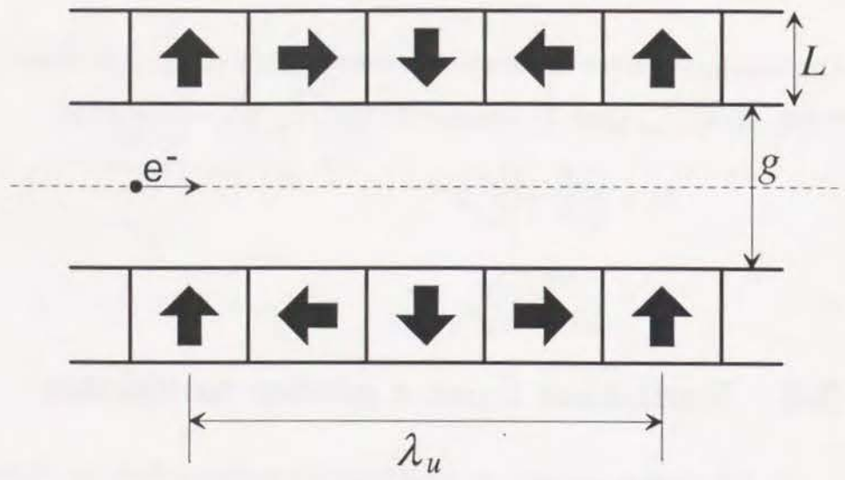

Figure 2.6. Schematic cross section of a planar undulator. The arrow shows the direction of the magnetization of each magnet.

$$B_z = 0,$$

$$B_y = 2B_r \sum_{\mu=0} \sin(nk_u z)\, \mathrm{e}^{-n\pi g/\lambda_u} \frac{\sin(n\pi/4)}{n\pi/4} (1 - \mathrm{e}^{-2n\pi L/\lambda_u}). \tag{2.71}$$

From the above equation, it is found that not only the fundamental component but harmonics of n =5, 9, 13,... are contained. Nevertheless, the strength of the field due to those harmonics are negligibly small. Therefore, we can approximate as follows

$$B_y = B_0 \sin k_u z, \tag{2.72}$$

where B_0 represents the peak field given by

$$B_0 = 1.8 B_r\, \mathrm{e}^{-\pi g/\lambda_u} (1 - \mathrm{e}^{-2\pi L/\lambda_u}). \tag{2.73}$$

2.4.2 Deflection parameter

Let us consider the motion of the electron moving in the magnetic field expressed by equation (2.72). The equation of motion of an electron moving in an arbitrary

field is given by

$$\frac{d\boldsymbol{p}}{dt} = e\boldsymbol{v} \times \boldsymbol{B}. \tag{2.74}$$

Substituting

$$\boldsymbol{B} = (0, \quad B_0 \sin k_u z, \quad 0),$$

into equation (2.74), we have

$$\begin{aligned} m\gamma\, \dot{v_x} &= -eB_0 v_z \sin k_u z, \\ m\gamma\, \dot{v_y} &= 0, \\ m\gamma\, \dot{v_z} &= eB_0 v_x \sin k_u z. \end{aligned} \tag{2.75}$$

Integrating the x component, we obtain

$$\beta_x = v_x/c = \frac{K}{\gamma} \cos k_u z, \tag{2.76}$$

where the dimensionless parameter K is defined as

$$K = \frac{eB_0 \lambda_u}{2\pi mc}. \tag{2.77}$$

K is often called a deflection parameter. We define a deflection angle δ as

$$\delta = \sqrt{\beta_x^2 + \beta_y^2}. \tag{2.78}$$

The deflection angle is the angle between the direction of the electron motion and the undulator axis. In this case, δ is simply equal to β_x because $\beta_y = 0$. Therefore, the maximum deflection angle, $\delta_{\max}$, is found to be K/γ. In Figs. 2.7 (a)$\sim$(c), the radiation cone with the vertical angle of γ^{-1} and the trajectory are shown for three cases of K. When $K \ll 1$, all the trajectory contributes equally to the radiation because the deflection angle is always much smaller than γ^{-1}. Therefore, the electron motion observed in the laboratory frame (apparent motion) looks a harmonic oscillation, which means that the radiation contains only the fundamental.

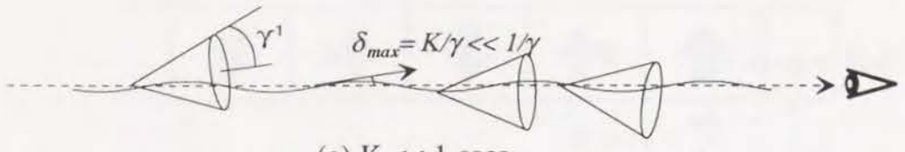

(a) K << 1 case

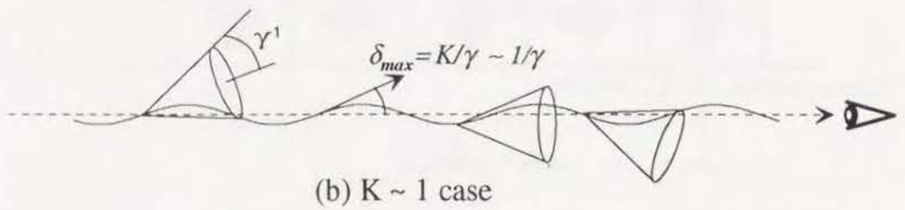

(b) K ~ 1 case

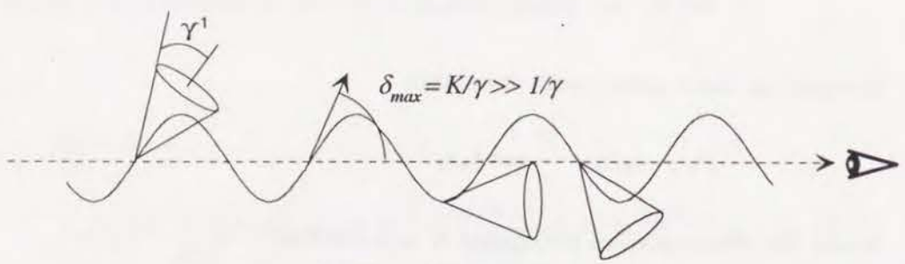

(c) K >> 1 case

Figure 2.7. Trajectory and radiation cone in the case of (a)$K \ll 1$, (b)$K \sim 1$ and (c)$K \gg 1$.

When $K \sim 1$, the contribution is large where $\delta \sim 0$, while it is small where $\delta \sim K/\gamma$. Therefore, the apparent motion does not look a harmonic oscillation any longer, which means that the radiation contains higher harmonics. When $K \gg 1$, only a limited part of the trajectory with $\delta \sim 0$ contributes to the radiation. Therefore, the apparent motion looks far from a harmonic oscillation, which means that so many higher harmonics are contained in the spectrum.

2.4.3 Electron motion

Since the electron is relativistic, the z component of the velocity is calculated as

$$\beta_z = \sqrt{\beta^2 - \beta_x^2 - \beta_y^2}. \tag{2.79}$$

Substituting equation (2.76) and $\beta_y = 0$, β_z is calculated as follows

$$\begin{aligned} \beta_z &\simeq \beta\left(1 - \frac{K^2}{2\gamma^2}\cos^2 k_u z\right) \\ &= \beta\left(1 - \frac{K^2}{4\gamma^2} - \frac{K^2}{4\gamma^2}\cos 2k_u z\right) \\ &= \beta_z^* - \frac{\beta K^2}{4\gamma^2}\cos 2k_u z, \end{aligned} \tag{2.80}$$

where β_z^* is the average of β_z and given by

$$\beta_z^* = \beta\left(1 - \frac{K^2}{4\gamma^2}\right). \tag{2.81}$$

Using β_z^*, $k_u z$ is calculated as follows

$$k_u z \sim k_u c\beta_z^* t = \frac{2\pi\beta c}{\lambda_u}\left(1 - \frac{K^2}{4\gamma^2}\right)t \equiv \omega_0 t, \tag{2.82}$$

with

$$\omega_0 = \frac{2\pi\beta c}{\lambda_u}\left(1 - \frac{K^2}{4\gamma^2}\right). \tag{2.83}$$

From above equations, β is expressed as

$$\boldsymbol{\beta} = \beta\left[\frac{K}{\gamma}\cos\omega_0 t, \quad 0, \quad \left(1 - \frac{K^2}{4\gamma^2} - \frac{K^2}{4\gamma^2}\cos 2\omega_0 t\right)\right]. \tag{2.84}$$

Integrating over time, we obtain the position of the electron

$$\boldsymbol{r} = \beta c\left[\frac{K}{\gamma\omega_0}\sin\omega_0 t, \quad 0, \quad \left(1 - \frac{K^2}{4\gamma^2}\right)t - \frac{K^2}{8\omega_0\gamma^2}\sin 2\omega_0 t\right]. \tag{2.85}$$

2.4.4 Frequency of the fundamental radiation

Substituting β_z^* into (2.29), we obtain the frequency of the fundamental radiation from the planar undulator

$$\omega_1 = \frac{4\pi c\gamma^2/\lambda_u}{1 + K^2/2 + \gamma^2\theta^2}. \tag{2.86}$$

Here we have used the approximations

$$\beta \simeq 1 - \frac{1}{2\gamma^2}, \tag{2.87}$$

and

$$\cos\theta \simeq 1 - \frac{\theta^2}{2}. \tag{2.88}$$

From equation (2.86), it is found that the frequency of the fundamental radiation is varied by changing the K value, or the peak magnetic field. According to equation (2.73), the peak magnetic field is varied by changing the parameter g or the magnet gap. Therefore, we can say that the radiation from the planar undulator is tunable.

2.4.5 Spectrum

The photon flux density for the k-th harmonic obtained from the planar undulator is calculated as

$$\frac{d^2P_k}{d\Omega d\omega} = \frac{e^2\gamma^2}{4\pi\epsilon_0 c}(f_x^2 + f_y^2), \tag{2.89}$$

with

$$f_x(\gamma\theta,\phi) = \xi[2S_0\gamma\theta\cos\phi - K(S_1 + S_{-1})]P_N, \tag{2.90}$$

$$f_y(\gamma\theta,\phi) = 2\xi S_0\gamma\theta\sin\phi P_N. \tag{2.91}$$

(See appendix A.1 for details and the definition of the symbols.) When observed on axis, f_y is found to be zero. Therefore, the radiation is horizontally polarized for

each harmonic. In addition, $S_{\pm1}$ is calculated as follows

$$\begin{aligned} S_{\pm1} &= \sum_p J_p\left(\frac{kK^2/4}{1+K^2/2}\right) J_{2p+k\pm1}(0) \\ &= \begin{cases} J_{-(k\pm1)/2}\left(\dfrac{kK^2/4}{1+K^2/2}\right); & k = \text{odd number}, \\ 0; & k = \text{even number}. \end{cases} \end{aligned} \tag{2.92}$$

Here we have used the well known formula of the Bessel functions

$$J_n(0) = \begin{cases} 1; & n = 0, \\ 0; & n \geq 1. \end{cases} \tag{2.93}$$

From above equations, it is found that only the odd-number harmonics are observed on axis. The on-axis photon flux density is calculated as

$$\begin{aligned} \frac{d^2P}{d\Omega d\omega}_{\theta=0} &= \frac{e^2\gamma^2}{4\pi\epsilon_0 c}\frac{K^2}{1+K^2/2}P_N^2 \\ &\quad \sum_{\text{k=odd}} \xi_0^2\left[J_{\frac{k-1}{2}}\left(\frac{K^2\xi_0}{4}\right) - J_{\frac{k+1}{2}}\left(\frac{K^2\xi_0}{4}\right)\right]^2, \end{aligned} \tag{2.94}$$

with

$$\xi_0 = \frac{k}{1+K^2/2}. \tag{2.95}$$

Examples of on-axis spectra obtained from the planar undulator for various K values are shown in Figs. 2.8 (a)$\sim$(d). We have assumed that the electron energy is 8 GeV, the average current 100 mA, the period length of the undulator 5 cm and the number of periods 90. When $K = 0.1$, only the fundamental radiation appears in the spectrum. As the K value increases, the fundamental radiation is shifted to the lower energy. Simultaneously, more and more higher harmonics appear in the spectrum, as is already discussed in section 2.4.2. If one wants to use only the fundamental, all other harmonics cause the unreasonable heat load.

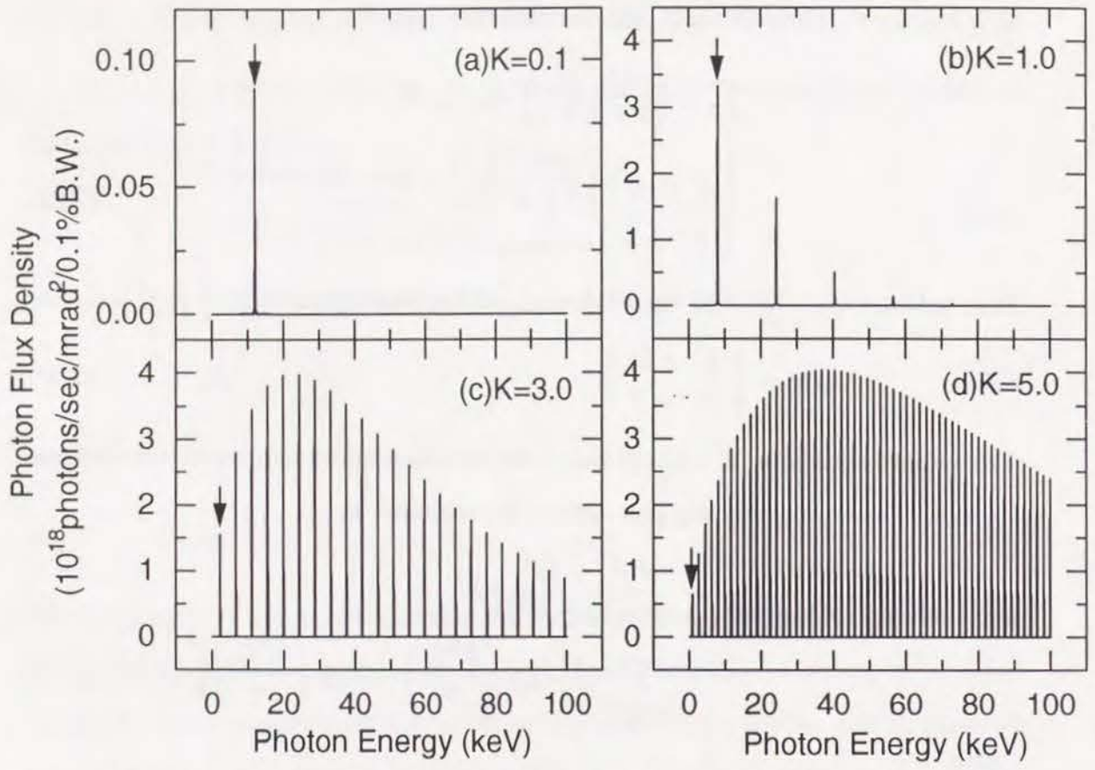

Figure 2.8. Examples of spectra obtained from the planar undulator. Four cases of the K value are shown. (a)K=0.1, (b)K=1.0, (c)K=3.0 and (d)K=5.0. The arrows show the fundamental radiation.

2.4.6 Wiggler as a large K limit of the planar undulator

There is another type of ID called a wiggler. This is considered as a large K limit of the planar undulator. The general explanation of the wiggler is described below.

When K is much larger than unity, the spectrum obtained from the planar undulator contains so many higher harmonics, as shown in Fig. 2.8 (d). Because of some errors of the magnetic field, the finite size of the aperture to extract the photon beam and the finite angular divergence of the electron beam, the sharp peak for each harmonic is broadened and the spectral shape reduces to the envelope of

that of the ideal spectrum. In this case, the device is called a wiggler. The spectral shape of the wiggler is similar to that of bending-magnet radiation, which means that the wiggler radiation is considered as the incoherent sum of SR emitted from each pole in the device.

According to the above explanation, it seems that only the K value determines whether an ID is a wiggler or an undulator. However, this is a little mistake. Although the peak of the higher harmonics is broadened, that of the fundamental radiation remains sharp, as described later. Therefore, if one uses the fundamental radiation, this device should be regarded as an undulator. On the other hand, if one uses the energy range in the envelope part, the device should be regarded as a wiggler.

2.4.7 Power density

Substituting $\beta_x = (K/\gamma)\cos\omega_0 t$ and $\beta_y = 0$ into equation (2.47), we obtain the power density obtained from the planar undulator for two polarization components

$$\begin{pmatrix} \frac{dP_\parallel}{d\Omega} \\ \frac{dP_\perp}{d\Omega} \end{pmatrix} = \frac{\gamma^4\omega_0 e^2 N K^2}{2\pi^2\epsilon_0 c}\int_{-\pi}^{\pi}\frac{\sin^2\eta}{D^5} \times \begin{pmatrix} (1-X^2+Y^2)^2 \\ 4X^2Y^2 \end{pmatrix}, \tag{2.96}$$

with

$$X = \gamma\theta_x - K\cos\eta, \tag{2.97}$$

$$Y = \gamma\theta_y, \tag{2.98}$$

$$D = 1 + X^2 + Y^2. \tag{2.99}$$

The total power density is calculated as

$$\frac{dP}{d\Omega} = \frac{\gamma^4\omega_0 e^2 N K^2}{2\pi^2\epsilon_0}\int_{-\pi}^{\pi}\left[\frac{1}{D^3} - \frac{4X^2}{D^5}\right]\sin^2\eta d\eta. \tag{2.100}$$

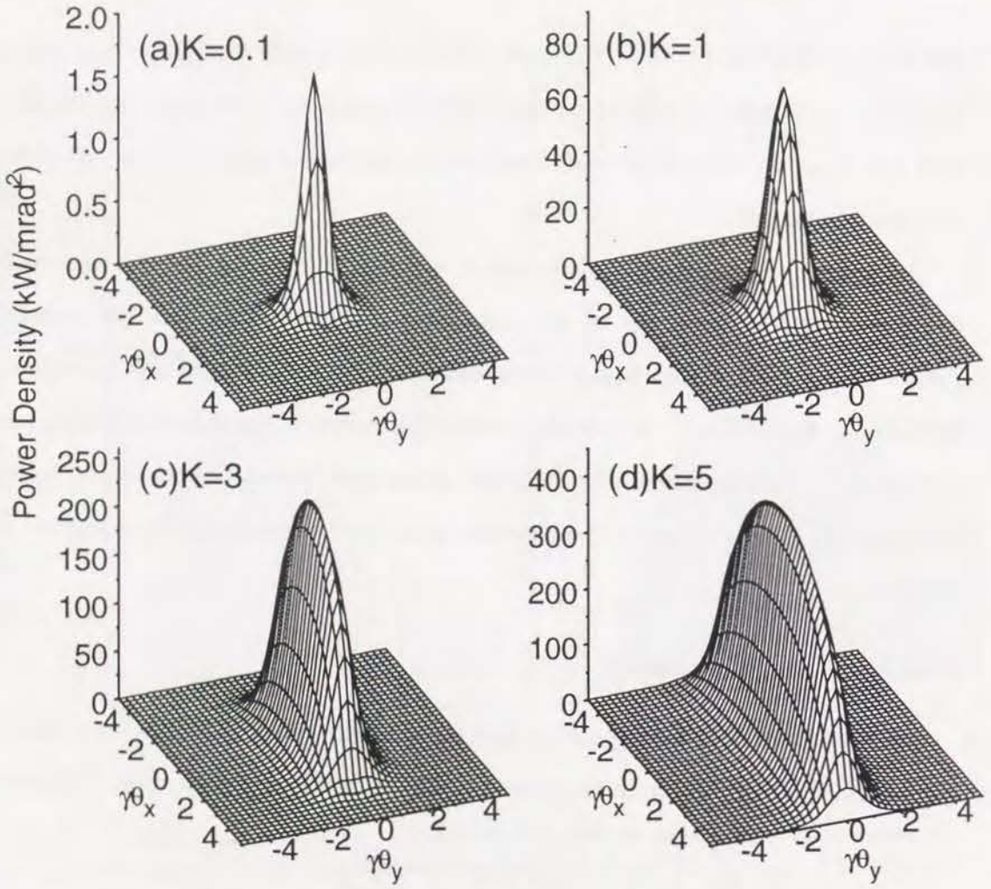

Figure 2.9. Examples of the spatial distribution of the power density.

Figures 2.9 (a)∼(d) show examples of the spatial distribution of the power density. The parameters used in the calculation are correspondent to those in Figs. 2.8 (a)∼(d). In each case, the on-axis value is the maximum. The peak width of the distribution along θ_y axis is almost the same in each case, however, that along θ_x axis becomes larger with increasing of K. This is due to the fact that β_x varies from $-K/\gamma$ to K/γ, while β_y is always equal to zero.

2.4.8 Effects due to the angular divergence

So far, we have ignored the angular divergence of the electron beam. In practice, the electron beam has the finite angular divergence. The photon flux density including the effect of the angular divergence of the beam is calculated as (see appendix B for details)

$$\frac{d^2P_k}{d\Omega d\omega} = \frac{e^2\gamma^2N^2}{4\pi\epsilon_0 c}(S_{xx}+S_{yy}), \tag{2.101}$$

$$\begin{aligned} S_{xx,yy} &= \frac{1}{2\pi\gamma^2\sigma_{x'}\sigma_{y'}}\int_0^\infty udu\int_{-\pi}^{\pi}d\alpha f_{x,y}^2(u,\alpha) \\ &\quad\times\exp\left[-\frac{(u\cos\alpha-\gamma\theta\cos\phi)^2}{2\gamma^2\sigma_{x'}^2}\right] \\ &\quad\times\exp\left[-\frac{(u\sin\alpha-\gamma\theta\sin\phi)^2}{2\gamma^2\sigma_{y'}^2}\right]. \end{aligned} \tag{2.102}$$

Examples of spectra including the effect of the finite angular divergence of the beam calculated using equations (2.101) and (2.102) are shown in Fig. 2.10 (a)∼(d). The angular divergence, $\sigma_{x',y'}$, are assumed to be γ^{-1}. In addition to odd-number harmonics, even-number harmonics appear in the spectrum. This is due to the fact that the radiation emitted from an electron having a slope with respect to the undulator axis is observed to have some emission angle by an observer on axis.

Comparing with Figs. 2.8 (a)∼(d), it is found that the intensity of the fundamental radiation is degraded by about 1/20 due to the angular divergence for each case of the K value. For higher harmonics, the degradation is more remarkable. When $K = 5$, the spectral shape in the energy region higher than 10 keV is found to be similar to the envelope of the ideal spectrum. Therefore, if one uses the radiation in this energy region, the device should be regarded as a wiggler. On the other hand, if the fundamental radiation is used, it should be regarded as an undulator.

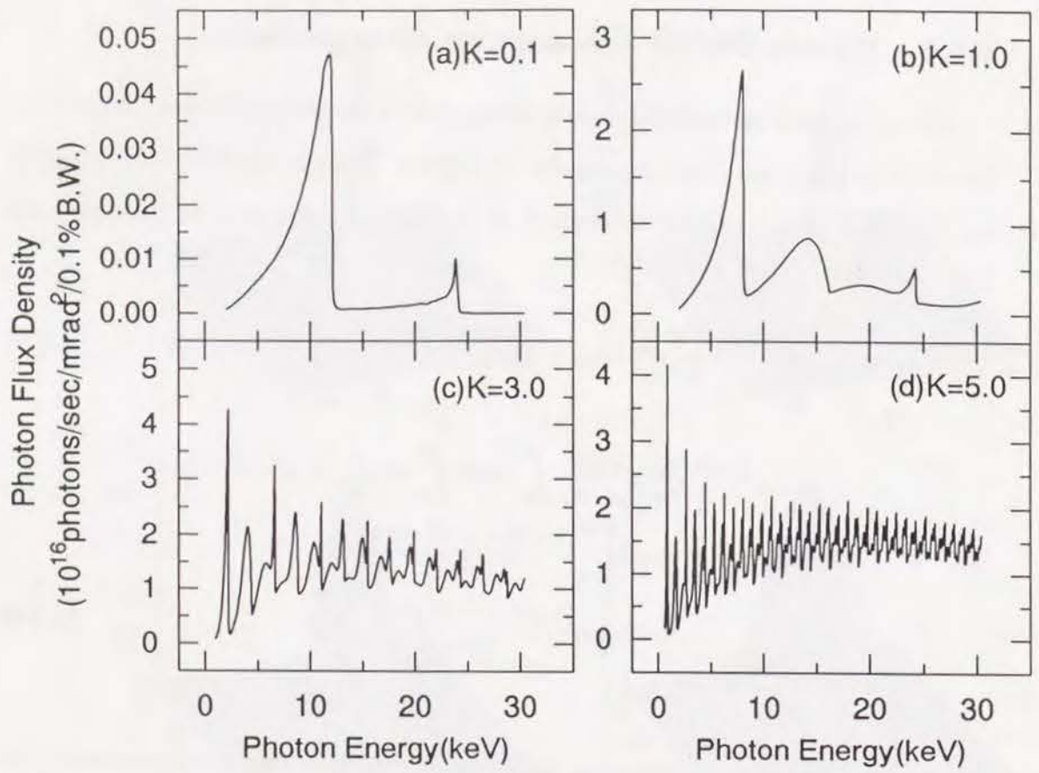

Figure 2.10. Examples of spectra obtained from the planar undulator, including the effect of the angular divergence of the beam.

2.5 Radiation from a helical undulator

In the previous section, we have investigated the radiation from the planar undulator. Another ID of great interest is a helical undulator, which is considered as a special case of an elliptical undulator.

2.5.1 Configuration of magnets

In the elliptical undulator, the magnetic field is given by

$$\boldsymbol{B} = \left[B_{x0} \cos\left(\frac{2\pi}{\lambda_u} z\right),\ B_{y0} \sin\left(\frac{2\pi}{\lambda_u} z\right),\ 0 \right]. \tag{2.103}$$

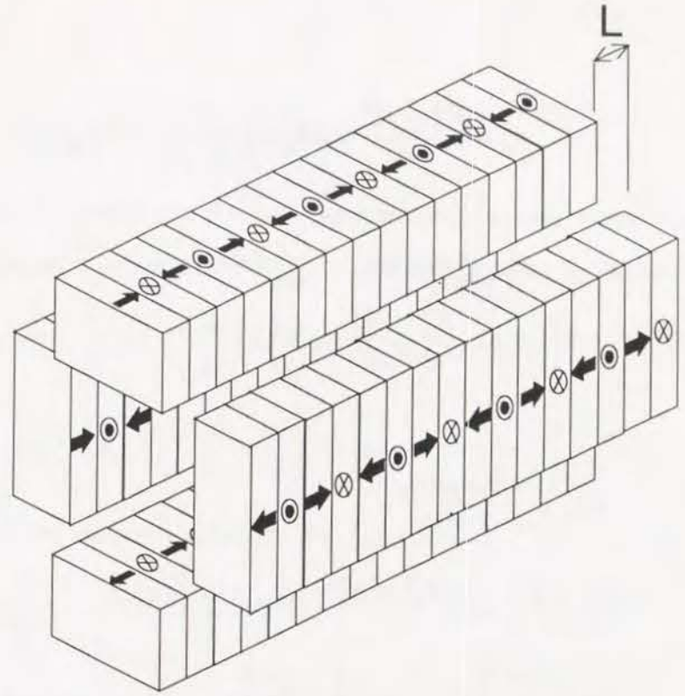

Figure 2.11. Schematic illustration of the elliptical undulator.

A simple way to realize the magnetic fields given by equation (2.103) is to superpose two planar undulators, one of which is rotated 90° along the z axis from the other, as shown in Fig. 2.11. In this case, the relative distance, L, should be set to $\lambda_u/4$. In the case of IDs to be installed in the storage ring, however, another configuration of magnets should be adopted. The reason is that the horizontal aperture should be sufficiently large for the beam life time and the beam injection. This problem will be discussed again in section 5.3.

2.5.2 Electron motion

In the same manner taken in sections 2.4.2 and 2.4.3, we obtain the position and relative velocity of the electron moving in the elliptical undulator

$$\boldsymbol{\beta} = \left(\frac{K_y}{\gamma} \cos\omega_0 t,\ \ \frac{K_x}{\gamma} \sin\omega_0 t, \right.$$

$$\beta_z^* + \frac{K_x^2 - K_y^2}{4\gamma^2}\cos 2\omega_0 t\Bigg), \tag{2.104}$$

$$\begin{aligned} \boldsymbol{r} &= c\Bigg(\frac{K_y}{\gamma\omega_0}\sin\omega_0 t, \quad -\frac{K_x}{\gamma\omega_0}\sin\omega_0 t, \\ &\quad \beta_z^* t + \frac{K_x^2 - K_y^2}{8\gamma^2\omega_0}\sin 2\omega_0 t\Bigg), \end{aligned} \tag{2.105}$$

with

$$K_{x,y} = \frac{eB_{x0,y0}/\lambda_u}{2\pi mc}, \tag{2.106}$$

$$\beta_z^* = 1 - \frac{1}{4\gamma^2}(K_x^2 + K_y^2), \tag{2.107}$$

$$\omega_0 = \frac{2\pi c}{\lambda_u}\left[1 - \frac{1}{4\gamma^2}(K_x^2 + K_y^2)\right]. \tag{2.108}$$

From equation (2.107), the frequency of the fundamental radiation is calculated as

$$\omega_1 = \frac{4\pi c\gamma^2/\lambda_u}{1 + K_x^2/2 + K_y^2/2 + \gamma^2\theta^2}. \tag{2.109}$$

Due to the horizontal magnetic field K_x, the frequency is slightly smaller than that of the planar undulator.

2.5.3 Spectrum

The photon flux density for the k-th harmonic obtained from the elliptical undulator is calculated as

$$\frac{dP_k}{d\Omega d\omega} = \frac{e^2\gamma^2 N^2}{4\pi\epsilon_0 c}(|f_x|^2 + |f_y|^2), \tag{2.110}$$

with

$$f_x(\gamma\theta,\phi) = \xi[2S_0\gamma\theta\cos\phi - K_x(S_1 + S_{-1})]P_N, \tag{2.111}$$

$$f_y(\gamma\theta,\phi) = \xi[2S_0\gamma\theta\sin\phi - iK_y(S_1 + S_{-1})]P_N, \tag{2.112}$$

$$\xi = \frac{k}{1 + K_x^2/2 + K_y^2/2 + \gamma^2\theta^2}. \tag{2.113}$$

(See appendix A.2 for details and the definition of the symbols.) When $K_x = K_y = K$, the device is called a helical undulator. In this case, f_x and f_y are rewritten as

$$f_x = 2\xi K\left[J_n(X)\left(\frac{\gamma\theta}{K} - \frac{k}{X}\right)\cos\phi - iJ_n'(X)\sin\phi\right]P_N, \tag{2.114}$$

$$f_y = 2\xi K\left[J_n(X)\left(\frac{\gamma\theta}{K} - \frac{k}{X}\right)\sin\phi + iJ_n'(X)\cos\phi\right]P_N. \tag{2.115}$$

Here we have used the recursion relations for $J_n(x)$

$$\frac{d}{dx}J_n(x) = \frac{J_{n-1}(x) - J_{n+1}(x)}{2}, \tag{2.116}$$

$$\frac{2n}{x}J_n(x) = J_{n-1}(x) + J_{n+1}(x). \tag{2.117}$$

When observed on axis, $f_{x,y}$ are rewritten as

$$f_x = \begin{cases} \dfrac{K}{(1+K^2)^2}; & k = 1, \\ 0; & k \geq 2, \end{cases} \tag{2.118}$$

$$f_y = if_x. \tag{2.119}$$

Here we have used the relation for the Bessel functions

$$J_0'(0) = \begin{cases} \dfrac{1}{2}; & k = 1, \\ 0; & k \geq 2. \end{cases} \tag{2.120}$$

From equations (2.118) and (2.119), it is found that only the fundamental radiation is observed on axis and that the radiation is circularly polarized because the phase difference between $F_{k\perp}$ and $F_{k\parallel}$ is $\pi/2$. The reason why only the fundamental radiation is observed on axis is explained as follows: From equation (2.104), the deflection angle of the electron moving in the helical undulator is found to be

$$\delta = \sqrt{\left(\frac{K_x}{\gamma}\cos\omega_0 t\right)^2 + \left(\frac{K_y}{\gamma}\sin\omega_0 t\right)^2} = \frac{K}{\gamma}. \tag{2.121}$$

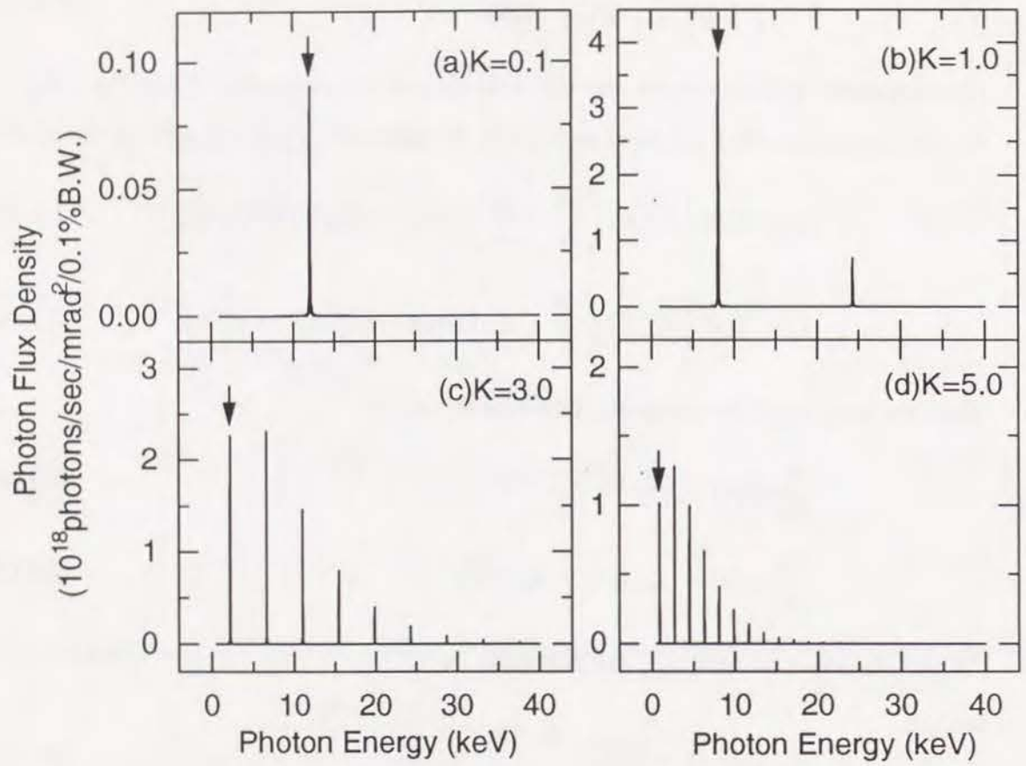

Figure 2.12. Examples of spectra obtained from the elliptical undulator. Four cases are shown. The value, $K = \sqrt{K_x^2 + K_y^2}$, is assumed to be (a)0.1, (b)1.0, (c)3.0 and (d)5.0. The ratio, K_x/K_y, is set to 0.5 in each case. The arrows show the fundamental radiation.

Namely, the deflection angle is constant. Therefore, all the trajectory contributes equally to the radiation in the case of the helical undulator. As described in section 2.4.2, the apparent motion in such a case becomes a harmonic oscillation. Therefore, the radiation from the helical undulator contains only the fundamental when observed on axis. This is a great advantage because the user is never annoyed by the unreasonable heat load caused by higher harmonics. With respect to obtaining higher-energy photons with a circular polarization, this advantage in turn becomes a disadvantage. Because no higher harmonics are contained in the radiation obtained

from an ID which has a helical trajectory, a "helical wiggler" never exists†. This problem will be discussed again in chapter 6.

The on-axis photon flux density obtained from the helical undulator is calculated as

$$\frac{dP}{d\Omega d\omega} = \frac{e^2\gamma^2 N^2}{4\pi\epsilon_0 c}\frac{2K^2}{(1+K^2)^2}P_N^2. \tag{2.122}$$

Examples of on-axis spectra obtained from the elliptical undulator for various K values are shown in Figs. 2.12 (a)∼(d). The K values are shown by the value, $K = \sqrt{K_x^2 + K_y^2}$. The parameters used in the calculation are the same as those in section 2.4.5. When $K = 0.1$, only the fundamental radiation appears in the spectrum. With increasing of the K value, higher harmonics appear, however, the contribution is not so large as that of the planar undulator.

2.5.4 Power density

Substituting $\beta_x = K_y \cos\omega_0 t$ and $\beta_y = K_x \sin\omega_0 t$ into equation (2.47), we obtain the power density obtained from the elliptical undulator

$$\frac{dP}{d\Omega d\omega} = \frac{\gamma^4\omega_0 e^2 N K^2}{2\pi^2\epsilon_0}\int_{-\pi}^{\pi}\left(\frac{E_1}{D^3} - \frac{E_2}{D^5}\right)d\eta, \tag{2.123}$$

with

$$E_1 = K_y^2 \sin^2\eta + K_x^2\cos^2\eta, \tag{2.124}$$

$$E_2 = 4(K_y X \sin\eta - K_x Y\cos\eta)^2, \tag{2.125}$$

$$X = \gamma\theta_x - K_y\cos\eta, \tag{2.126}$$

$$Y = \gamma\theta_y - K_x\sin\eta, \tag{2.127}$$

$$D = 1 + X^2 + Y^2. \tag{2.128}$$

†Of course, this depends on the definition of the ID. For some people, in particular, specialists of the FEL theory and experiment, all IDs are called wiggler.

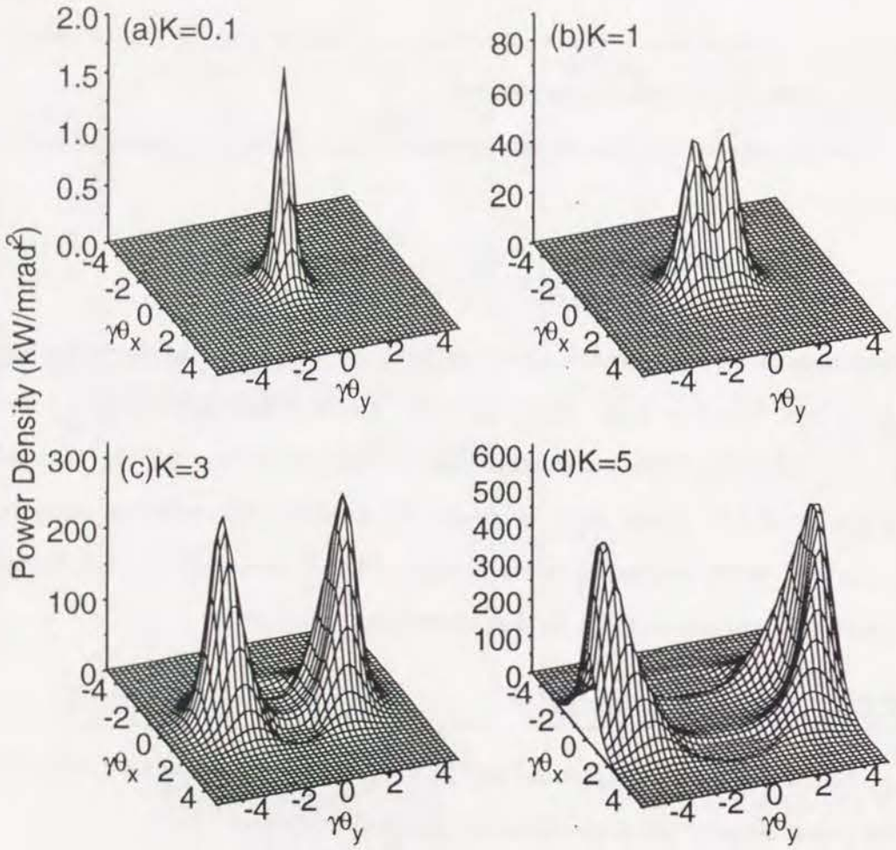

Figure 2.13. Examples of the spatial distribution of the power density obtained from the elliptical undulator.

Examples of the spatial distribution of the power density obtained from the elliptical undulator are shown in Figs. 2.13 (a)$\sim$(d). Although most of the radiated power exists on axis in the case that $K = 0.1$, that in other three cases exists off axis and the on-axis power density is extremely low compared to the maximum value. Figures 2.14 (a)$\sim$(d) show the spatial distribution of the helical undulator. As well as the elliptical undulator, most of the radiated power exists off axis when K is larger than unity.

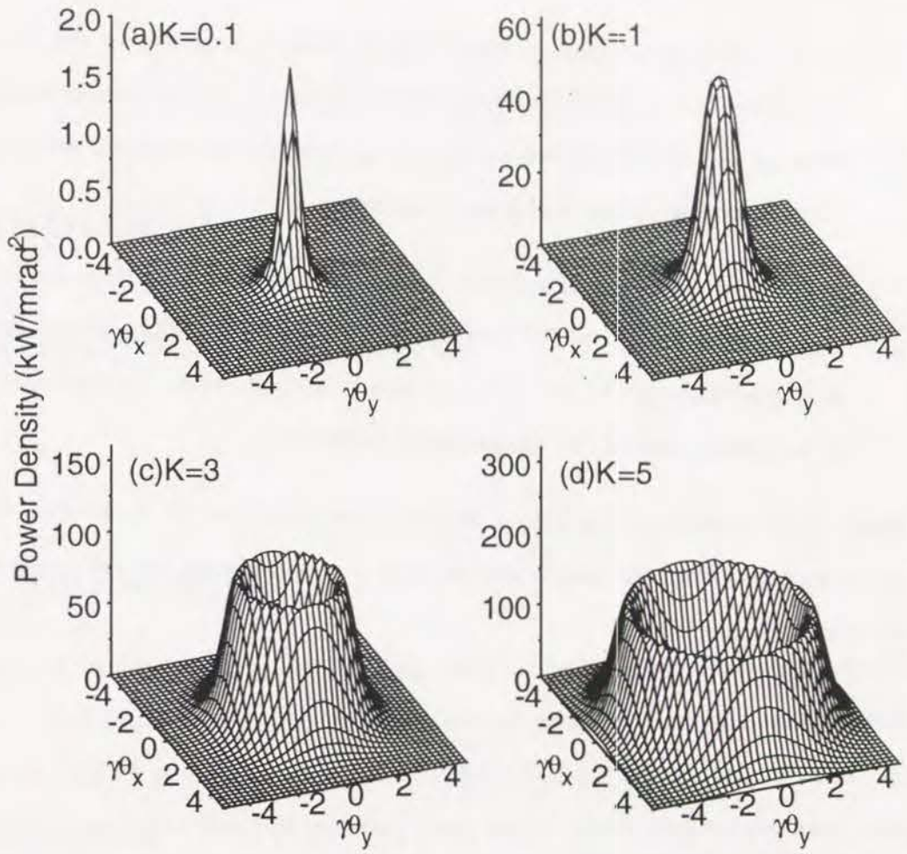

Figure 2.14. Examples of the spatial distribution of the power density obtained from the helical undulator.

2.6 Conclusions

The characteristics of radiation obtained from ordinary IDs, the planar and helical undulators, were investigated. The results are summarized below.

1. In the case of the planar undulator, the radiation characteristics are affected strongly by the so-called deflection parameter, or the K value. When K is much lower than unity, only the fundamental radiation appears in the spectrum. When K is close to unity, low-order higher harmonics such as the 3rd, 5th, 7th, appear in the spectrum in addition to the fundamental. When K is

much higher than unity, so many higher harmonics appear in the spectrum. Therefore, the unreasonable heat load brought by higher harmonics becomes more serious as the increase of the K value, while the available energy is not limited to that of the fundamental radiation.

2. In the case of the helical undulator, only the fundamental radiation is observed regardless of the K value. Therefore, the users of helical-undulator radiation are never annoyed by the unreasonable heat load, while the available energy is limited to that of the fundamental radiation.

These characteristics of undulator radiation are concerned with the fact that the power radiated from the relativistic electron concentrates on the narrow cone with the vertical angle of γ^{-1}.

Chapter 3

Figure-8 Undulator

3.1 Introduction

In an SR facility using an electron beam with an extremely high energy (large SR facility), for example 8 GeV, high K values are necessary in order to obtain vacuum ultraviolet (VUV) and soft x ray (SX). As described in the previous chapter, the planar undulator has a disadvantage that many higher harmonics are observed when high K values are applied. As a result, the on-axis power density is unreasonably high due to the contribution of those higher harmonics. On the other hand, no higher harmonics are observed on axis in the case of the helical undulator, even when the K value is high. Therefore, the reasonable way to obtain VUV and SX in the large SR facility is to use the helical undulator instead of the planar undulator. However, the polarization of radiation emitted from the helical undulator is circular, therefore use of the helical undulator does not become a best solution for obtaining VUV and SX, for users who want to use linearly-polarized radiation.

A novel undulator to be proposed in this chapter is an ID to obtain linearly-polarized VUV and SX in the large SR facility. The principle is as follows: The circular polarization is regarded as the superposition of two components of linear polarization. On the contrary, the linear polarization is regarded as the superposition

of two components of circular polarization. Therefore, the radiation emitted from an electron moving along a trajectory which contains two helical trajectories with different helicities is considered to be linearly polarized. The on-axis power density obtained from such a device may be as low as that of the helical undulator. This is the basic idea of the novel undulator and it is called a "figure-8" undulator, because the orbit projected on the transverse plane looks like a figure 8.

3.2 Principle

It is possible to obtain linearly-polarized radiation with low on-axis power density by using the ID containing two helical trajectories with different helicities. Two configurations are possible. One is a "tandem" type and the other is a "parallel" type.

3.2.1 Tandem type: similar to the crossed undulator

A simple way to make the trajectory containing two helical trajectories with different helicities is to place two helical undulators tandem. There is an ID similar to this device, which is known as a crossed undulator [22]-[24]. This ID applies the principle that an arbitrary polarization is obtained from two linear polarizations.

Figure 3.1 shows the schematic illustration of the crossed undulator. Two planar undulators are contained, one of which is rotated 90° along the z axis. The planar undulator generating the horizontal field is called a vertical undulator because the electron trajectory lies in the vertical plane and that generating the vertical field is called a horizontal undulator. By adjusting the phase difference between SR emitted from both undulators, circularly polarized radiation is obtained. The adjustment can be done by the "modulator," or the magnet inserted between the two undulators. Because the radiation emitted from each undulator contains higher harmonics, higher harmonics with a circular polarization are also available, unlike the ordinary helical undulator.

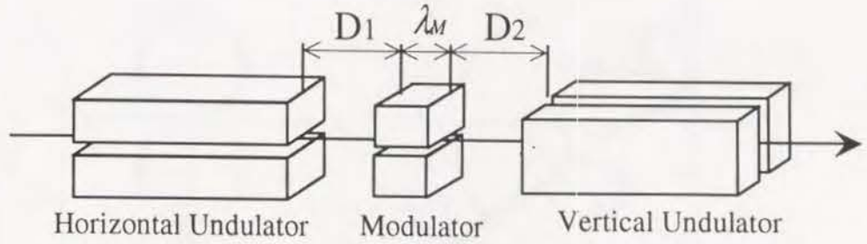

Figure 3.1. Schematic illustration of a crossed undulator.

The phase difference between radiation waves emitted from both planar undulators is given by [23]

$$\alpha = 2\pi\frac{\omega}{\omega_1}\left[N + \frac{\lambda_M(1+K_M^2/2)+D}{\lambda_u(1+K^2/2)}\right], \tag{3.1}$$

with

$$K_M = \frac{eB_M\lambda_M}{2\pi mc}, \tag{3.2}$$

$$D = D_1 + D_2, \tag{3.3}$$

where ω is the frequency of the radiation, ω_1 the frequency of the fundamental radiation, N the number of the periods of each undulator, B_M the peak magnetic field of the modulator.

The phase difference expressed by equation (3.1) is correct only in the case that the electron is parallel to the beam axis. If the electron has a slope θ with respect to the beam axis, equation (3.1) should be rewritten as

$$\alpha = 2\pi\frac{\omega}{\omega_1}\left[N + \frac{\lambda_M(1+K_M^2/2+\gamma^2\theta^2)+D}{\lambda_u(1+K^2/2+\gamma^2\theta^2)}\right]. \tag{3.4}$$

It is found from the above equation that the phase difference for an electron having a finite slope with respect to the beam axis is different from that of the electron parallel to the axis, which can cause the degradation of the degree of polarization.

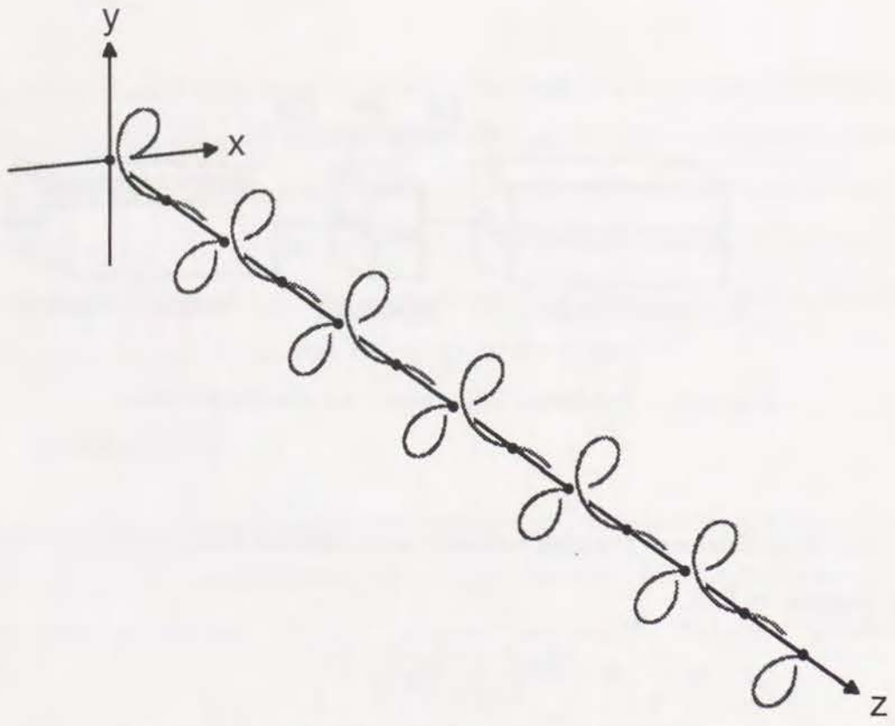

Figure 3.2. Ideal trajectory of the figure-8 undulator.

In particular, the degradation is remarkable for higher harmonics due to the term, ω/ω_1. In fact, the degree of polarization of radiation obtained from the crossed undulator is known to be quite sensitive to the angular divergence of the beam not only for the higher harmonics but for the fundamental. Therefore, the beam emittance should be quite low for obtaining the high degree of polarization when using such devices.

The discussions above also applies to an ID which contains two helical undulators tandem. Therefore, other methods for the combination of helical trajectories are preferable in order to achieve the high degree of polarization.

3.2.2 Parallel type: ideal trajectory of the figure-8 undulator

Another type of configuration for the combination of two helical trajectories is to

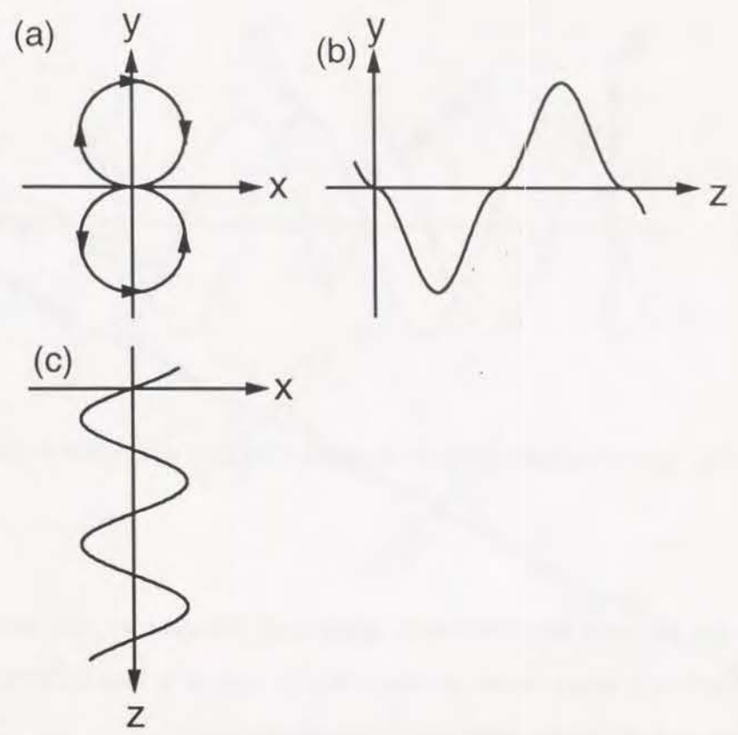

Figure 3.3. Ideal orbits in a figure-8 undulator projected on (a)x-y (b)y-z and (c)z-x planes.

place helical trajectories parallel, as shown in Fig. 3.2. The electron moves along the right- and left-handed helices alternately. Since the polarization of radiation emitted from an electron moving along the left-handed (right-handed) helix is left-handed (right-handed), the total polarization is linear. In addition, the spatial distribution of the power density is considered to be the same as that of the helical undulator, therefore the on-axis power density will be low.

When the trajectory is projected on the x-y, y-z and z-x planes, we obtain the orbits shown in Fig. 3.3 (a)$\sim$(c). In this case, the period length of the vertical undulator is twice as long as that of the horizontal undulator. As a definition, however, we consider the period length of the total device as that of the horizontal undulator.

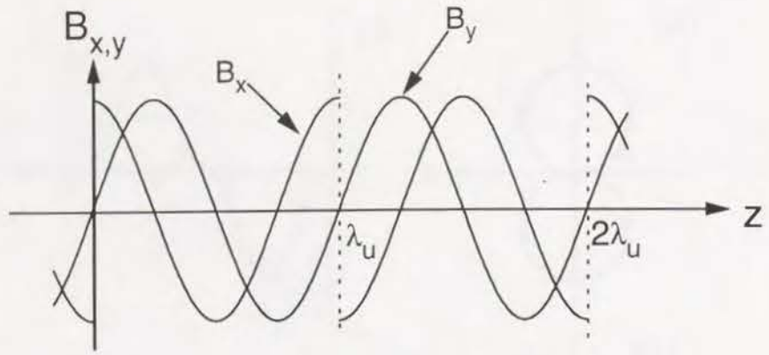

Figure 3.4. Horizontal and vertical magnetic fields in the figure-8 undulator (ideal case).

In order to make electrons move along such a trajectory, the vertical magnetic field should be discontinuous, as shown in Fig. 3.4. It is impossible to make such a field because it does not satisfy the Maxwell equations.

3.2.3 Figure-8 type: practical trajectory of the figure-8 undulator

In the previous section, the parallel configuration was found to be impractical because the magnetic field was impossible to generate. Therefore, some modification or approximation is needed.

Let us consider a trajectory as shown in Fig. 3.5. This trajectory can be considered as an approximation of the trajectory shown in Fig. 3.2. Therefore, linear polarization and low on-axis power density is expected. When the trajectory is projected on the x-y, y-z and z-x planes, we obtain the orbits shown in Figs. 3.6 (a)$\sim$(c). In order to make electrons move along such trajectories, the magnetic fields shown in Fig. 3.7 are needed. It is found from the figure that both the horizontal and vertical magnetic fields are sinusoidal, like an ordinary ID. Therefore, such magnetic fields are realized easily by a slight modification of the helical undulator.

As well as the ideal case, the period length of the vertical undulator is twice as

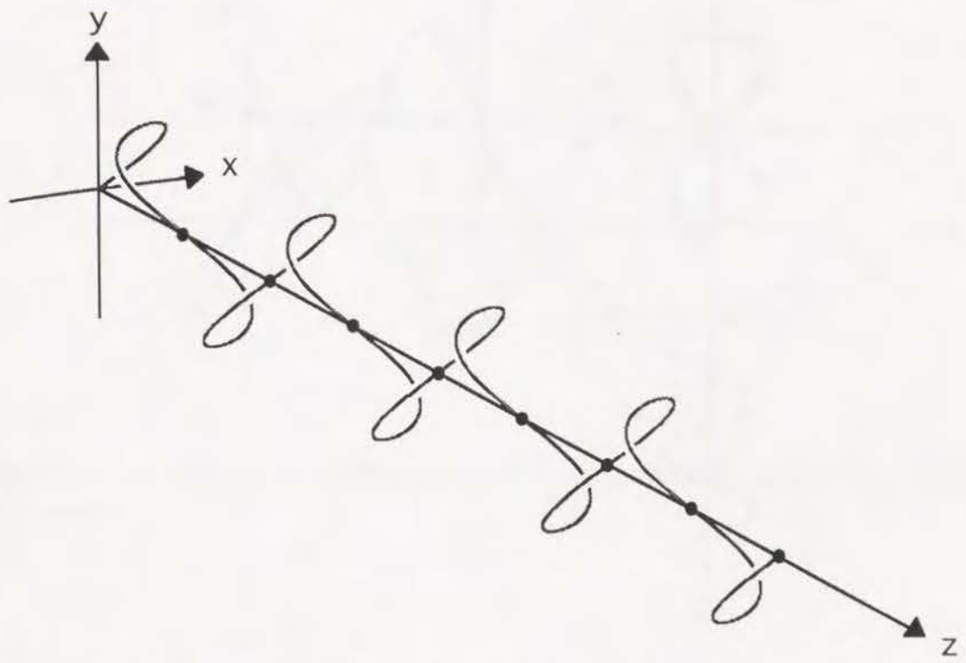

Figure 3.5. Approximated trajectory of the figure-8 undulator.

long as that of the horizontal. Again, we consider the period length of the total device as that of the horizontal undulator.

3.3 Spectrum

Let us calculate the spectrum to be obtained from the figure-8 undulator. In order to investigate the performances of the figure-8 undulator, it is sufficient to calculate only the practical case (Fig. 3.5), however, it may be quite interesting to calculate the ideal case (Fig. 3.2) also, and compare to the practical case.

3.3.1 Ideal case

First, the ideal case is considered. The magnetic fields shown in Fig. 3.4 are given by the equations

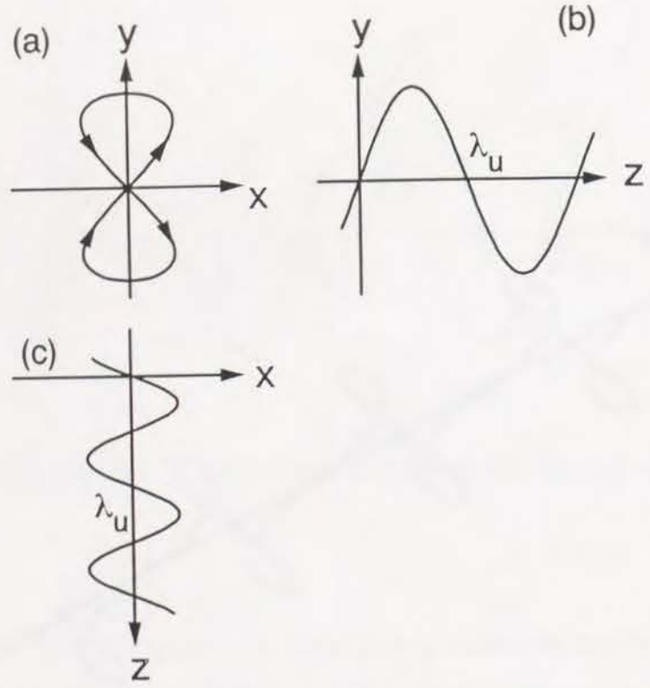

Figure 3.6. Approximated orbits in the figure-8 undulator projected on (a)x-y (b)y-z and (c)z-x planes.

$$B_x = \begin{cases} B_0 \cos k_u z; & 2n\lambda_u \le z < (2n+1)\lambda_u, \\ -B_0 \cos k_u z; & (2n+1)\lambda_u \le z < 2(n+1)\lambda_u, \end{cases} \tag{3.5}$$

$$B_y = B_0 \sin k_u z, \tag{3.6}$$

where n is an integer and

$$k_u = \frac{2\pi}{\lambda_u}. \tag{3.7}$$

In the same manner taken in chapter 2, the relative velocity and position of the electron moving in the fields given by equation (3.5) are calculated as

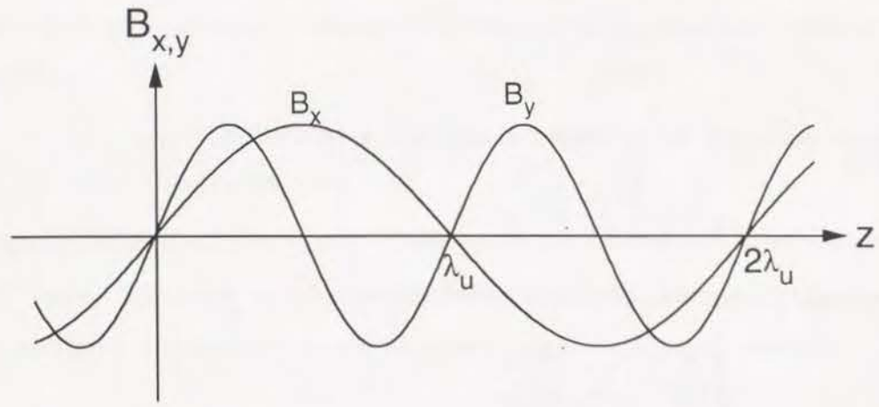

Figure 3.7. Horizontal and vertical magnetic fields in the figure-8 undulator (practical case).

$$\beta_x = \frac{K}{\gamma}\cos\omega_0 t,$$

$$\beta_y = \begin{cases} \frac{K}{\gamma}\sin\omega_0 t; & 2n\lambda_u \le z < (2n+1)\lambda_u, \\ -\frac{K}{\gamma}\sin\omega_0 t; & (2n+1)\lambda_u \le z < 2(n+1)\lambda_u, \end{cases} \tag{3.8}$$

$$\beta_z = \beta\left(1 - \frac{K^2}{2\gamma^2}\right),$$

$$x = \frac{cK}{\gamma\omega_0}\sin\omega_0 t,$$

$$y = \begin{cases} \frac{cK}{\gamma\omega_0}(1-\cos\omega_0 t); & 2n\lambda_u \le z < (2n+1)\lambda_u, \\ \frac{cK}{\gamma\omega_0}(\cos\omega_0 t - 1); & (2n+1)\lambda_u \le z < 2(n+1)\lambda_u, \end{cases} \tag{3.9}$$

$$z = c\beta\left(1 - \frac{K^2}{2\gamma^2}\right)t,$$

with

$$\omega_0 = \frac{2\pi c}{\lambda_u}\left(1 - \frac{K^2}{2\gamma^2}\right), \tag{3.10}$$

$$K = \frac{eB_0\lambda_u}{2\pi mc}. \tag{3.11}$$

The frequency of the fundamental radiation is calculated as

$$\omega_1 = \frac{4\pi c\gamma^2/\lambda_u}{1 + K^2 + \gamma^2\theta^2}. \tag{3.12}$$

The total photon flux density is calculated as

$$\frac{d^2P}{d\Omega d\omega} = \sum_{n=1/2} \frac{d^2P_n}{d\Omega d\omega}, \tag{3.13}$$

where $n = \frac{1}{2}, 1, \frac{3}{2}, 2, \ldots, \frac{k}{2}$ and

$$\frac{d^2P_k}{d\Omega d\omega} = \frac{e^2\gamma^2(N/2)^2}{4\pi\epsilon_0 c}(|f_x|^2 + |f_y|^2), \tag{3.14}$$

with

$$f_x = P_N \begin{cases} -\dfrac{K}{2}(S^+_{-1} + S^+_1) + \gamma\theta\cos\phi S^+_0; & k = \text{even}, \\ -iK(R^-_{-2} + R^-_2) + 2i\gamma\theta\cos\phi R^-_0; & k = \text{odd}, \end{cases} \tag{3.15}$$

$$f_y = P_N \begin{cases} \dfrac{iK}{2}(S^-_{-1} - S^-_1) + \gamma\theta\sin\phi S^+_0; & k = \text{even}, \\ K(R^+_{-2} - R^+_2) + 2i\gamma\theta\sin\phi R^-_0; & k = \text{odd}, \end{cases} \tag{3.16}$$

$$P_N = \frac{\sin\pi N\omega/\omega_1}{\pi N(\omega/\omega_1 - n)}. \tag{3.17}$$

(See appendix A.3.1 for details and the definition of the symbols.) When observed on axis, f_x and f_y are calculated as

$$f_x = \begin{cases} 0; & n \neq 1, \\ -\dfrac{2K}{1+K^2}P_N; & n = 1, \end{cases} \tag{3.18}$$

$$f_y = \begin{cases} \dfrac{2K}{1+K^2}\dfrac{2n}{\pi(n^2-1)}P_N; & n = \text{half-odd integer}, \\ 0; & n = \text{integer}. \end{cases} \tag{3.19}$$

It is found from above equations that the fundamental radiation is horizontally polarized, while half-odd-integer harmonics are vertically polarized. The ratio of

the intensity of half-odd-integer harmonics to that of the fundamental radiation is calculated as

$$\frac{\text{half-odd-integer (=n) harmonics}}{\text{fundamental}} = \frac{4n^2}{\pi^2(n^2-1)^2}, \tag{3.20}$$

which rapidly reduces with increasing of the harmonic number and is independent of the K value. Therefore, reasonable utilization of the fundamental radiation is possible without being annoyed by the heat load caused by higher harmonics.

3.3.2 Practical case

Next, the practical case is considered. The magnetic fields shown in Fig. 3.7 are given by the equations

$$B_x = B_{x0}\sin\left(\frac{k_u}{2}z\right), \tag{3.21}$$

$$B_y = B_{y0}\sin k_u z, \tag{3.22}$$

with

$$k_u = \frac{2\pi}{\lambda_u}. \tag{3.23}$$

Solving the equations of motion, we have

$$\begin{aligned} \boldsymbol{r}(t) = c\beta\Bigg(&\frac{K_y}{\omega_0\gamma}\sin\omega_0 t, \quad \frac{2K_x}{\omega_0\gamma}\sin\frac{\omega_0 t}{2}, \\ &\left(1 - \frac{K_x^2 + K_y^2}{4\gamma^2}\right)t - \frac{K_x^2}{4\omega_0\gamma^2}\sin\omega_0 t - \frac{K_y^2}{8\omega_0\gamma^2}\sin 2\omega_0 t\Bigg), \end{aligned} \tag{3.24}$$

$$\begin{aligned} \boldsymbol{\beta}(t) \;=\; \beta\Bigg(&\frac{K_y}{\gamma}\cos\omega_0 t, \quad \frac{K_x}{\gamma}\cos\frac{\omega_0 t}{2}, \\ &1 - \frac{K_x^2 + K_y^2}{4\gamma^2} - \frac{K_x^2}{4\gamma^2}\cos\omega_0 t - \frac{K_y^2}{4\gamma^2}\cos 2\omega_0 t\Bigg), \end{aligned} \tag{3.25}$$

with

$$\omega_0 = \frac{2\pi\beta c}{\lambda_u}\left(1 - \frac{K_x^2 + K_y^2}{4\gamma^2}\right), \tag{3.26}$$

$$K_x = \frac{eB_{x0}(2\lambda_u)}{2\pi mc}, \tag{3.27}$$

$$K_y = \frac{eB_{y0}\lambda_u}{2\pi mc}. \tag{3.28}$$

The frequency of the fundamental radiation is calculated as

$$\omega_1 = \frac{4\pi c\gamma^2/\lambda_u}{1 + K_x^2/2 + K_y^2/2 + \gamma^2\theta^2}. \tag{3.29}$$

The total photon flux density is calculated as

$$\frac{d^2P_n}{d\Omega d\omega} = \sum_{n=1/2} \frac{d^2P_n}{d\Omega d\omega}, \tag{3.30}$$

$$\frac{d^2P_n}{d\Omega d\omega} = \frac{e^2\gamma^2N^2}{4\pi\epsilon_0 c}(f_x^2 + f_y^2), \tag{3.31}$$

with

$$f_x = \xi[2S_0\gamma\theta\cos\phi - K_y(S_2 + S_{-2})]P_N, \tag{3.32}$$

$$f_y = \xi[2S_0\gamma\theta\sin\phi - K_x(S_1 + S_{-1})]P_N. \tag{3.33}$$

(See appendix A.3.2 for details and the definition of the symbols.) As well as the ideal case, half-odd-integer harmonics appear in the spectrum.

When observed on axis, f_x and f_y are calculated as

$$f_x = \begin{cases} -\xi K_y P_N \sum_{p=-\infty}^{\infty} [J_{-2p-k-1}(Y) + J_{-2p-k+1}(Y)]J_p(Z) \\ \quad ;\ n = \text{integer}, \\ 0\ ;\ n = \text{half-odd integer}, \end{cases} \tag{3.34}$$

$$f_y = \begin{cases} 0\ ;\ n = \text{integer}, \\ -\xi K_x P_N \sum_{p=-\infty}^{\infty} [J_{-2p-\frac{2k+1}{2}}(Y) + J_{-2p-\frac{2k-1}{2}}(Y)]J_p(Z) \\ \quad ;\ n = \text{half odd integer}. \end{cases} \tag{3.35}$$

It is found from above equations that integer harmonics are horizontally polarized, while half-odd-integer harmonics are vertically polarized.

3.4 Examples of spectra

Now, let us show some examples of spectra to be obtained from the figure-8 undulator and compare to the planar undulator. For example, the electron energy is assumed to be 8 GeV, the beam current 100 mA, the period length 10 cm, the total length of an ID 4.4 m.

3.4.1 High-field case

First, a high-field case is considered. The K value is assumed to be 4.72 (=K, planar) and 3.34 (=K_x=K_y, figure-8). In this case, the energy of the fundamental radiation is found to be 500 eV. Figures 3.8 (a)$\sim$(c) show the spectra to be obtained from the planar, ideal-figure-8 and practical-figure-8 undulators, respectively. As already described in chapter 2, so many higher harmonics appear in the spectrum in the case of the planar undulator because the K value is much larger than unity. On the other hand, much less higher harmonics appear in the spectrum in the case of the figure-8 undulator. The photon flux density at 500 eV is also shown in the figure. It is found that the difference of the intensity between the planar and figure-8 undulators is small.

In order to compare the practical case with the ideal one, the spectra in the energy range between 0 and 4 keV are shown in Figs. 3.9 (a) and (b). As described before, half-odd-integer harmonics appear in the spectrum. As for integer harmonics, only the fundamental appears in the ideal case, while all integer harmonics appear in the practical case unlike the planar undulator which only contains the odd-number harmonics. The intensity in the practical case is found to be about three quarters of that in the ideal case.

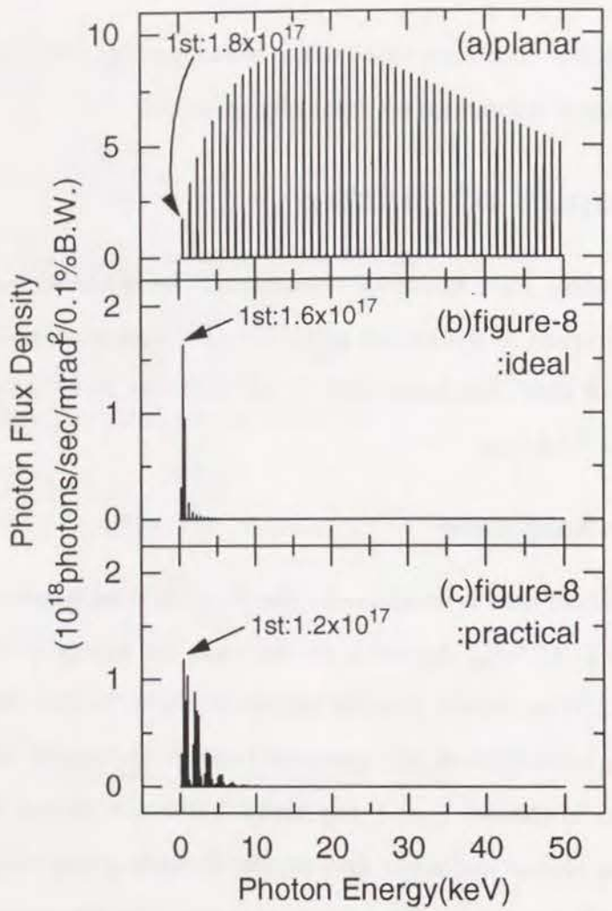

Figure 3.8. Examples of spectra to be obtained from the (a)planar, (b)ideal-figure-8 and (c)practical-figure-8 undulators.

3.4.2 Low-field case

Next, a low-field case is considered. The K value is assumed to be 0.66 (=K, planar) and 0.46 (=K_x=K_y, figure-8). In this case, the energy of the fundamental radiation is found to be 5000 eV. Figures 3.10 (a)$\sim$(c) show the spectra to be obtained from the planar, ideal-figure-8 and practical-figure-8 undulators, respectively. The contribution of higher harmonics to the spectrum is small not only in the case of the figure-8 undulator but the planar undulator. This is because the K value is small. Therefore, the effect due to the figure-8 trajectory is not so drastic as the

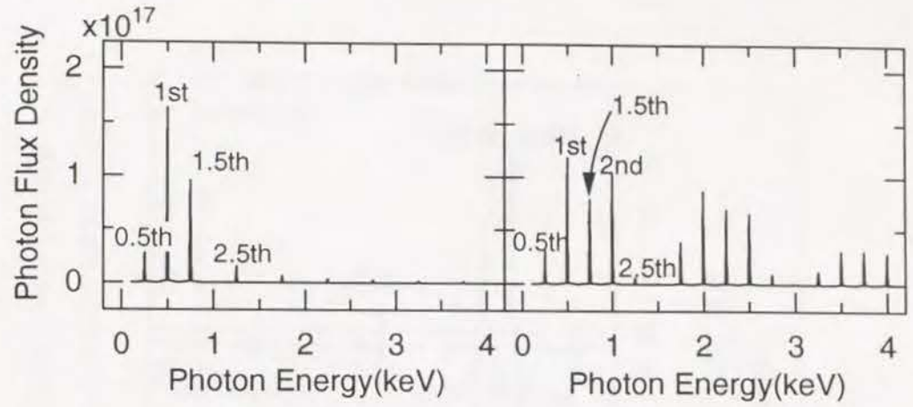

Figure 3.9. Spectra obtained from the figure-8 undulator between 0 and 4 keV in the (a)ideal and (b)practical cases.

high-field case. In addition, the degradation of the intensity at the energy of the fundamental is large compared to the high-field case. Moreover, the 1.5th harmonic in the ideal case is remarkable. This is due to the fact that the ratio expressed by equation (3.20) is independent of the K value.

In this way, the figure-8 undulator is not so effective in the low-field region. However, as described later, it has the advantage that some specific higher harmonic, for example, the third harmonic, can be eliminated completely by adjusting the ratio, K_x/K_y. In general, the radiation contains integer harmonics even after the monochromatization by a monochromator. Because even-number harmonics can be eliminated by using an ordinary crystal monochromator, for example, Si(111), the main higher harmonic may be the third. Therefore, only the fundamental can be obtained by adjusting K_x/K_y so as to eliminate the third harmonic. Of course, for the user who uses the double crystal monochromator, such discussions may be meaningless, because one can eliminate the third harmonic by detuning the second crystal of the monochromator [25].

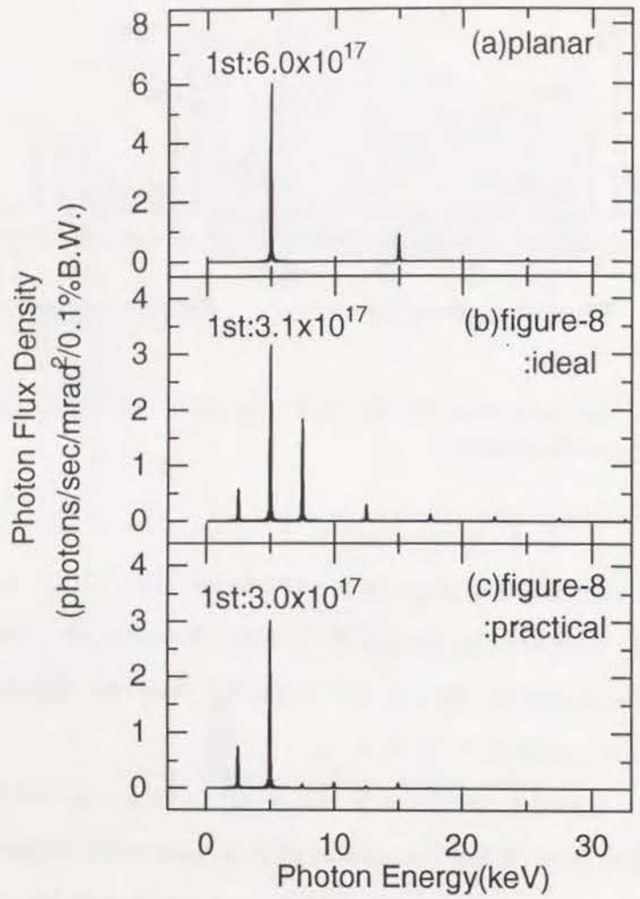

Figure 3.10. Examples of spectra to be obtained from (a)planar, (b)ideal-figure-8 and (c)practical-figure-8 undulators.

3.4.3 Effects due to the angular divergence

In the previous section, the angular divergence of the beam was not included in the calculation. In practice, the beam has a finite angular divergence. Therefore, comparison should be made by the calculation including the angular divergence of the beam. In this section, the effects due to the angular divergence on the radiation from the planar and figure-8 undulators are investigated. The undulator parameters used in the calculation are correspondent to those in Fig 3.8. Figures 3.11 (a) and (b) show the spectrum and the degree of linear polarization, P_L, obtained from the

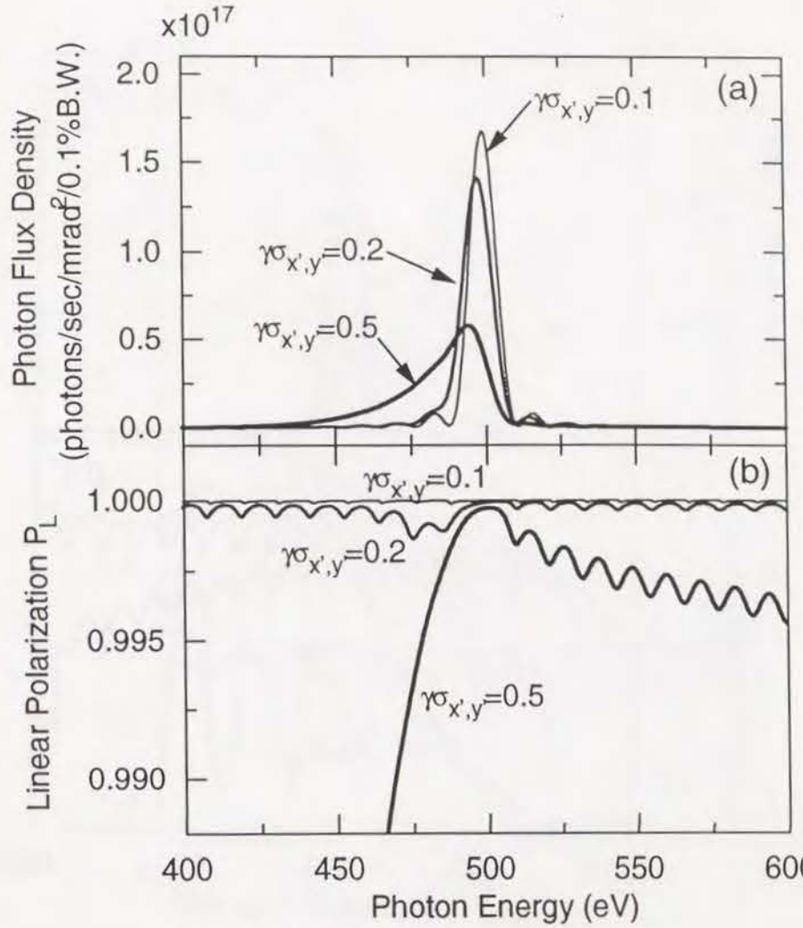

Figure 3.11. Spectrum and degree of linear polarization obtained from the planar undulator including the effect of the angular divergence.

planar undulator, respectively. The degradation of the photon flux density and P_L become more remarkable as the increase of the angular divergence. However, P_L at the peak energy remains sufficiently high when $\gamma\sigma_{x',y'} = 0.5$.

Figures 3.12 (a) and (b) correspond to Fig. 3.11, in the case of the figure-8 undulator. Unlike the planar undulator, the degradation of P_L is not negligible when $\gamma\sigma_{x',y'}$ are large. Therefore, the angular divergence of the beam should be low in the case that the extremely high degree of linear polarization is desired, which means that the emittance of the beam should be low and the betatron value should

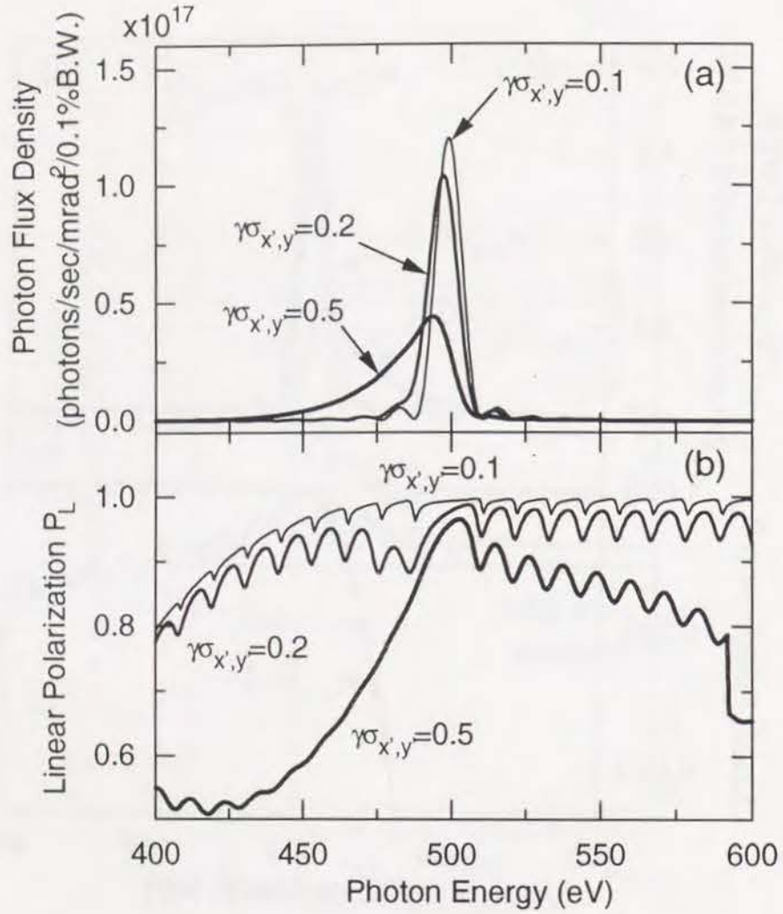

Figure 3.12. Spectrum and degree of linear polarization obtained from the practical-figure-8 undulator including the effect of the angular divergence.

be high.

For a reference, the spectrum and P_L to be obtained from the "tandem" type, which means that two helical undulators with different helicities are placed tandem, are shown in Figs. 3.13 (a) and (b). The angular divergence of the beam is included in the calculation. The degree of polarization at the energy of 500 eV in each case of $\gamma\sigma_{x',y'} = 0.1, 0.2$ and 0.5 are found to be 0.95, 0.71 and 0.29, respectively. The value of 0.29 may be almost meaningless for experiments which utilize the polarization of radiation. Therefore, the angular divergence of the beam should be extremely low

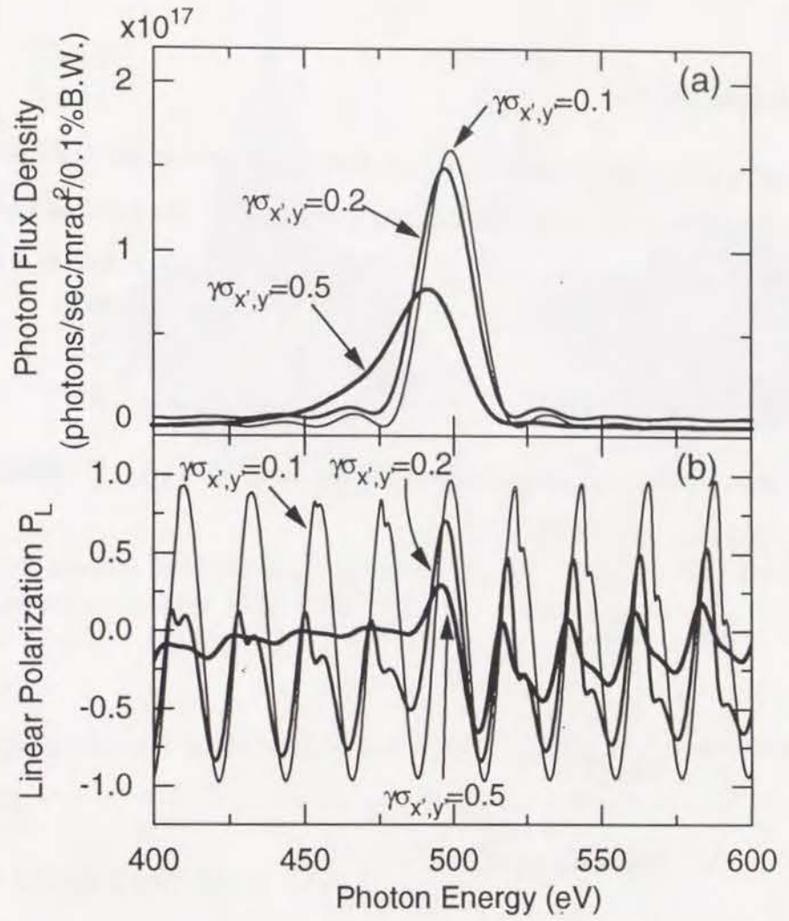

Figure 3.13. Spectrum and degree of linear polarization obtained from the "tandem" type including the effect of the angular divergence.

in order to use such IDs, as already described in section 3.2.1.

3.5 Power density

Calculating the power density at a fixed point in space may be quite important for the analysis of the heat load on optical elements and front-end components. In this section, the power density radiated from the figure-8 undulator is investigated.

3.5.1 Ideal case

First, the ideal case is considered. It is easy to understand that the power density obtained from the ideal-figure-8 trajectory is quite the same as that of the helical undulator, because the equation (2.47) does not contain $\boldsymbol{r}$, or the position of the electron.

3.5.2 Practical case

Next, the practical case is considered. Substituting $\beta_x = (K_y/\gamma)\cos(\omega_0 t/2)$ and $\beta_y = (K_x/\gamma)\cos\omega_0 t$ into (2.47), we have

$$\frac{dP}{d\Omega} = \frac{e^2}{8\pi^2\epsilon_0 c}\gamma^4\omega_0\, N \times \int_{-\pi}^{\pi} d\xi \left(\frac{E_1}{D^3} - \frac{E_2}{D^5}\right), \tag{3.36}$$

with

$$D = 1 + X^2 + Y^2, \tag{3.37}$$

$$X = \gamma\theta_x - K_y \cos 2\xi, \tag{3.38}$$

$$Y = \gamma\theta_y - K_x \cos\xi, \tag{3.39}$$

$$E_1 = K_x^2 \sin^2\xi + 4K_y^2 \sin^2 2\xi, \tag{3.40}$$

$$E_2 = 4(K_x Y \sin\xi + 2K_y X \sin 2\xi)^2. \tag{3.41}$$

The expression for the power density given by equation (3.36) is similar to that of the elliptical undulator. This is natural because the magnetic fields in the figure-8 undulator are similar to those in the elliptical undulator.

3.6 Spatial distribution of the power density

Now, let us calculate the spatial distribution of the power density obtained from the figure-8 undulator and compare to that from the planar undulator. The

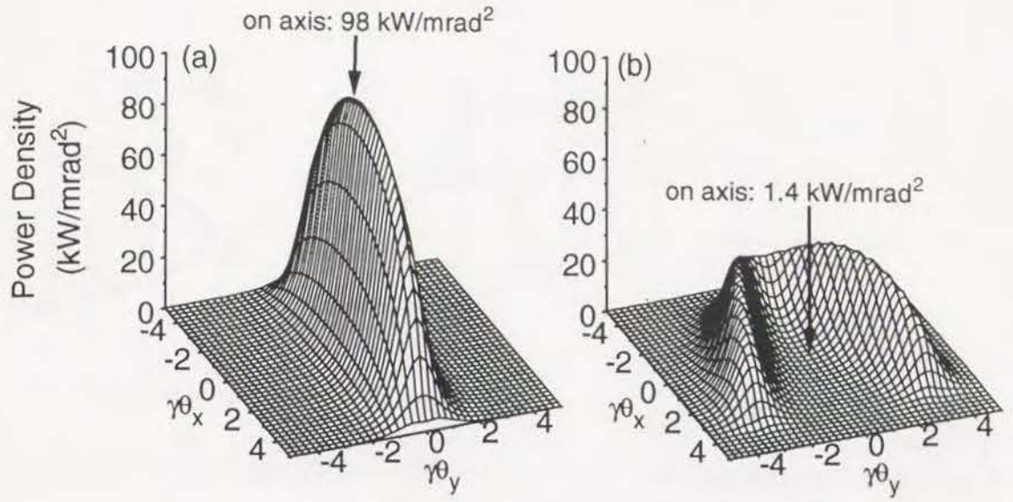

Figure 3.14. Spatial distribution of the power density obtained from the (a)planar and (b)figure-8 undulators (high-field case).

parameters to be used in the calculation are assumed to be the same as those in section 3.4.

3.6.1 High-field case

First, a high-field case is considered. The K value is assumed to be 4.72 (=K, planar) and 3.34 (=K_x=K_y, figure-8).

Figures 3.14 (a) and (b) show the spatial distribution of the power density obtained from the planar and figure-8 undulators, respectively. It is found from the figure that most of the power radiated from the planar undulator exists on axis. The on-axis power density is found to be 98 kW/mrad^2. On the other hand, most of the power radiated from the figure-8 undulator exists off axis. Therefore, the on-axis power density is much lower than that of the planar undulator and found to be 1.4 kW/mrad^2.

The spatial distribution of the power density obtained from the figure-8 undulator is asymmetric with respect to θ_x and forms a V figure. This is explained as follows.

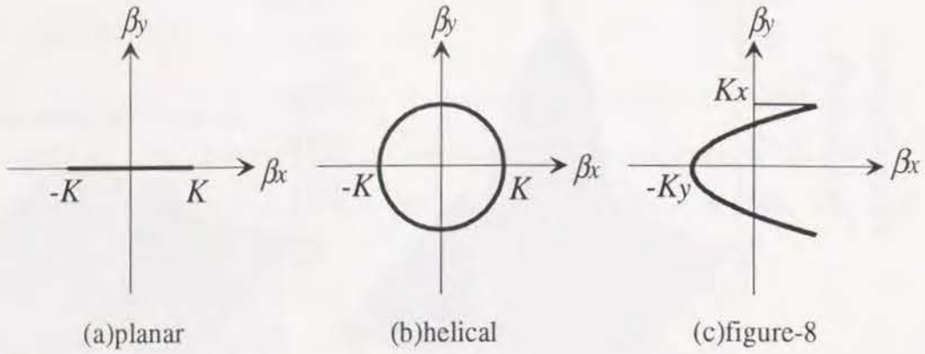

Figure 3.15. Relation between the horizontal and vertical velocities in the case of the (a)planar, (b)helical and (c)figure-8 undulators.

Figures 3.15 (a)$\sim$(c) show the relations between β_x and β_y for three types of undulator. In the case of the planar and helical undulators, the shapes are similar to their own orbits projected on the transverse plane. In the case of the figure-8 undulator, however, it does not look a figure 8 but a V figure. Since the power radiated from a relativistic electron is condensed to a narrow forward cone, the power radiated from the electron with the velocity $\boldsymbol{\beta} = (\beta_x, \beta_y)$ has its peak at the observation angle $(\theta_x, \theta_y) = (\beta_x, \beta_y)$, which means that the distribution of the power density reflects the relation between the horizontal and vertical velocities, β_x and β_y. Therefore, the spatial distribution of the power density obtained from the figure-8 undulator forms a V figure.

3.6.2 Low-field case

Next, low-field case is considered. The K value is assumed to be 0.66 (=K, planar) and 0.46 (=K_x=K_y, figure-8).

Figures 3.16 (a) and (b) show the spatial distribution of the power density obtained from the planar and figure-8 undulators, respectively. In this case, the V figure cannot be seen any more and most of the radiated power exists on axis as well as the planar undulator. The V figure is contracted to the axis and collapses.

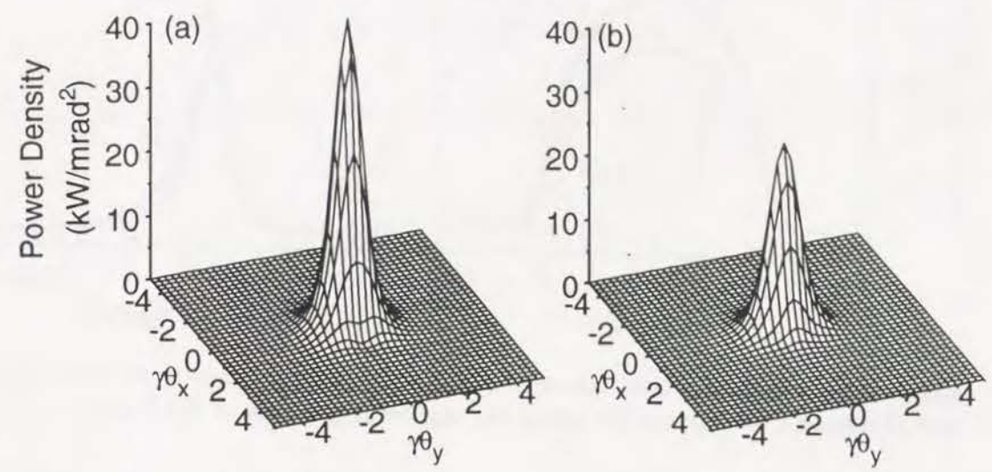

Figure 3.16. Spatial distribution of the power density obtained from the (a)planar and (b)figure-8 undulators (low-field case).

In this way, the figure-8 undulator cannot be used to suppress the on-axis heat load when the K value is small.

3.6.3 Effects due to the angular divergence

As well as the spectrum and the degree of polarization, the distribution of the power density is affected by the angular divergence of the beam.

Figures 3.17 (a) and (b) show the horizontal angular distribution of the power density including the effect of the angular divergence in the case of the planar and figure-8 undulators, respectively. The K values are correspondent to those in Figs 3.8 (a) and (b).

In the case of the planar undulator, the on-axis power density, which is the maximum value, is reduced as the increase of the angular divergence. On the other hand, the on-axis power density of the figure-8 undulator increases. This is due to the fact that the peak power density of the figure-8 undulator exists off axis and that it is broadened by the angular divergence of the beam. The designer of optical elements should be careful of the fact described above, since the situation is reverse

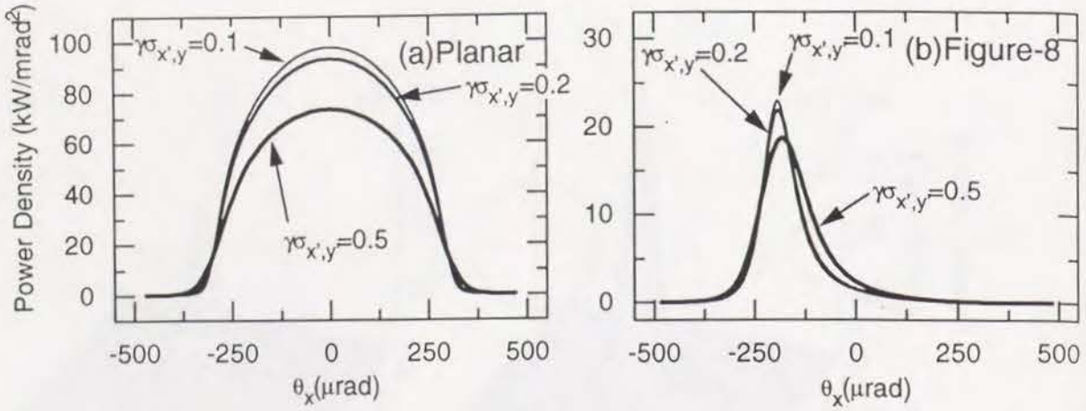

Figure 3.17. Horizontal distribution of the power density radiated from the (a)planar and (b)figure-8 undulators including the angular divergence of the beam.

to that of the planar undulator.

3.7 Other types of figure-8 undulator

So far, the period length of the vertical undulator has been set to the value twice as long as that of the horizontal undulator. One may think of other types of ID that the period length of the vertical undulator is M times as long as that of the horizontal, where M is an integer. If M can be large, the construction of the device may be easier because the number of magnet pieces can be reduced.

In this case, the magnetic fields can be written as

$$\boldsymbol{B} = \left(B_{x0} \sin\left(\frac{k_u z}{M}\right), \quad B_{y0} \sin k_u z, \quad 0 \right). \tag{3.42}$$

The photon flux density and the power density can be calculated in the same manner taken so far. The photon flux density is given as

$$\frac{d^2P}{d\Omega d\omega} = \sum_{k=1/M}^{\infty} \frac{d^2P_k}{d\Omega d\omega}, \tag{3.43}$$

where $k = \frac{1}{M}, \frac{2}{M}, \ldots, \frac{M-1}{M}, 1, \frac{M+1}{M}, \ldots \frac{n}{M}, \ldots$, and

$$\frac{d^2P_k}{d\Omega d\omega} = \frac{e^2\gamma^2 N^2}{4\pi\epsilon_0 c}(f_x^2 + f_y^2), \tag{3.44}$$

$$f_x(\gamma\theta,\phi) = \xi[2S_0\gamma\theta\cos\phi - K_y(S_M + S_{-M})]P_N, \tag{3.45}$$

$$f_y(\gamma\theta,\phi) = \xi[2S_0\gamma\theta\sin\phi - K_x(S_1 + S_{-1})]P_N, \tag{3.46}$$

$$\xi = \frac{k}{1 + (K_x^2 + K_y^2)/2 + \gamma^2\theta^2}, \tag{3.47}$$

$$K_x = \frac{eB_{x0}M\lambda_u}{2\pi mc}, \tag{3.48}$$

$$K_y = \frac{eB_{y0}\lambda_u}{2\pi mc}, \tag{3.49}$$

$$\omega_1 = \frac{4\pi c\gamma^2/\lambda_u}{1 + (K_x^2 + K_y^2)/2 + \gamma^2\theta^2}, \tag{3.50}$$

$$S_j = \sum_{p=-\infty}^{\infty}\sum_{q=-\infty}^{\infty}\sum_{r=-\infty}^{\infty} J_{Mk+2q+2Mp-Mr+j}(X)J_q(Y)J_p(Z)J_r(W), \tag{3.51}$$

$$X = 2\xi M K_x\gamma\theta\sin\phi, \tag{3.52}$$

$$Y = \frac{\xi M K_x^2}{4}, \tag{3.53}$$

$$W = 2\xi K_y\gamma\theta\cos\phi. \tag{3.54}$$

The power density is given as

$$\frac{dP}{d\Omega} = \frac{e^2\gamma^4}{4\pi^2\epsilon_0 c}\frac{\omega_0}{M}\frac{2N}{M}\int_{-\pi}^{\pi}\left(\frac{E_1}{D^3} - \frac{E_2}{D^5}\right)d\eta, \tag{3.55}$$

$$E_1 = K_x^2\sin^2\eta + M^2K_y^2\sin^2 M\eta, \tag{3.56}$$

$$E_2 = 4(MXK_y\sin M\eta + YK_x\sin\eta)^2, \tag{3.57}$$

$$X = \gamma\theta_x - K_y\cos\eta, \tag{3.58}$$

$$Y = \gamma\theta_y - K_x\cos\frac{\eta}{M}, \tag{3.59}$$

$$D = 1 + X^2 + Y^2. \tag{3.60}$$

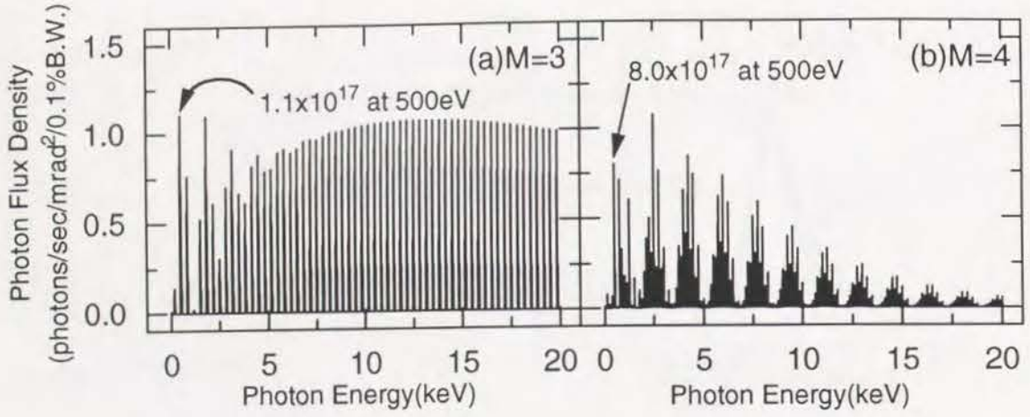

Figure 3.18. Examples of spectra in the case that (a)$M = 3$ and (b)$M = 4$.

Figures 3.18 (a) and (b) show the examples of spectra in the case that $M = 3$ and $M = 4$, respectively. The parameters used in the calculation are correspondent to those in Fig 3.8 (c). When $M = 3$, the contribution of higher harmonics to the spectrum is much larger than that of the ordinary figure-8 undulator and the spectrum is similar to the planar undulator. When $M = 4$, the contribution of higher harmonics is less than the $M = 3$ case, however, it is still large. In addition, the photon flux density at 500 eV in each case is less than that of the figure-8 undulator.

Figures 3.19 (a) and (b) show the spatial distribution of the power density in the case that $M = 3$ and $M = 4$, respectively. In each figure, the relation between β_x and β_y is also shown. The distribution of the power density reflects the relation between β_x and β_y, as already described in section 3.6. It is easy to understand the reason why the on-axis power density is high in the $M = 3$ case and low in the $M = 4$ case. Anyway, the on-axis power density in each case is higher than the that of the ordinary figure-8 undulator.

From the facts described above, we can say that the $M = 2$ case, or the ordinary figure-8 undulator, is the best configuration.

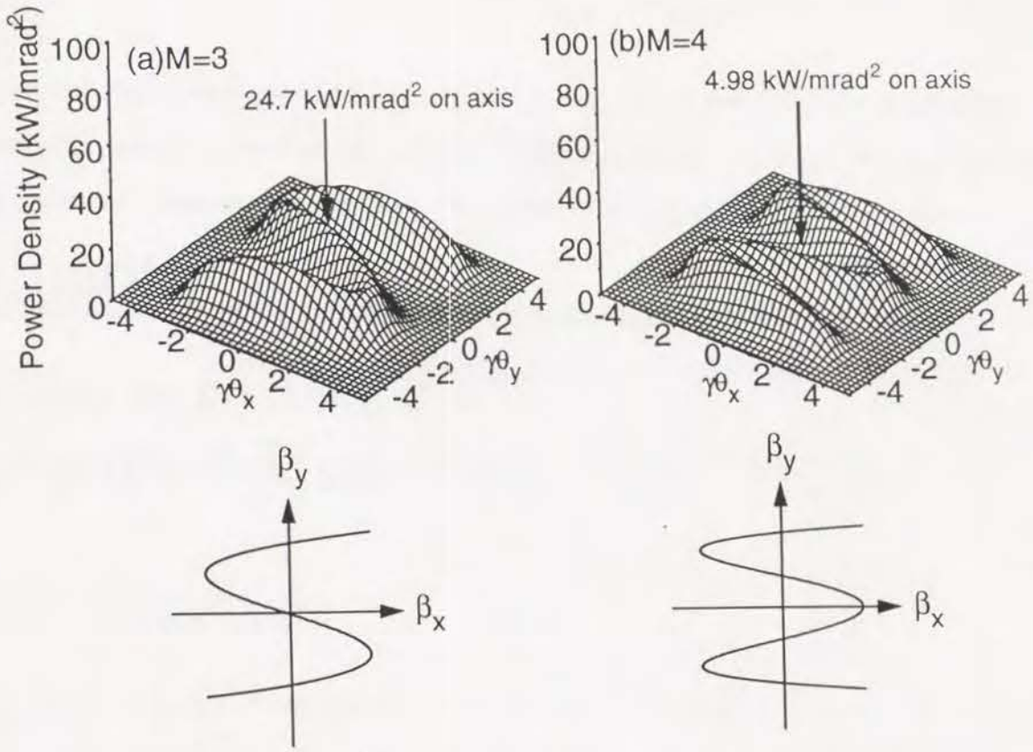

Figure 3.19. Spatial distribution of the power density (above) and relation between β_x and β_y (below) in the case that (a) $M = 3$ and (b) $M = 4$.

3.8 Conclusions

Three types of ID containing two helical trajectories with different helicities were proposed to obtain linearly-polarized radiation with a low on-axis power density. It was found that the degree of polarization obtained from the tandem type would be quite low and that the magnetic field of the parallel type, or the ideal-figure-8 undulator, should be discontinuous. Therefore, these two IDs were impractical for use. The figure-8 type, or the practical-figure-8 undulator, was found to be realized easily by a slight modification of the helical undulator.

Calculation showed that the photon flux density obtained from the figure-8 undulator was almost equivalent to that of the planar undulator, while the on-axis power

density was much lower. This was due to the fact that the power radiated from the figure-8 undulator existed mainly off axis like the helical undulator. The low on-axis power density is a great benefit for the VUV and SX beamline components, in particular, optical elements.

From now on, we call the practical-figure-8 undulator simply the figure-8 undulator since the ideal-figure-8 undulator is impossible to construct.

Chapter 4

Characteristics of Figure-8-Undulator Radiation

4.1 Introduction

The tunability of the undulator is achieved by changing the magnetic field, i. e., the magnet gap. The K value and the K ratio, which means the ratio of the horizontal K value (K_x) to the vertical K value (K_y), are considered to be often changed when changing the magnet gap in order to shift the energy of the fundamental radiation. Therefore, it is necessary to investigate the K-value and K-ratio dependences of radiation for the effective utilization of undulator radiation. In addition, these characteristics are important in determining the design of the figure-8 undulator such as the magnet configuration and the size of each magnet block.

As well as an ID, the design and the construction of a beamline to transport the photon beam is an important factor which determines the quality of the SR facility. Many components are contained in one beamline, e. g., x-ray beam position monitor (XBPM), X-Y slit, monochromator, and so on. The XBPM is used to monitor the position of the photon beam and to make a feedback on the storage-ring operation parameters. The X-Y slit is used to eliminate the power brought by the photons in unnecessary spectral part. The monochromator is used to obtain a monochromatized photon beam with the typical bandwidth of 10^{-4}. In designing these components,

it is important to know the spatial distribution of radiation, such as the power, polarization and harmonics.

Because the trajectory in the figure-8 undulator is a novel one and different from any other IDs which have been proposed or developed so far, it is important to investigate the above characteristics of radiation obtained from the figure-8 undulator and to clarify the difference between the figure-8 and ordinary undulators.

4.2 Polarization

If the user is not concerned with the polarization, the best way to obtain SR with the high brilliance is to use the helical undulator. If the user wants to use the linear polarization, the degree of polarization is one of important items to be careful when constructing a beamline.

4.2.1 Spatial dependence

From equations (A.59)$\sim$(A.62), we obtain the two polarization components of the electric field of radiation emitted from the figure-8 undulator

$$E_{n\parallel} = \frac{ie\omega_1\gamma}{2\epsilon_0}\frac{\mathrm{e}^{-i\omega_1 nR/cc}}{R} f_x(\gamma\theta,\phi), \tag{4.1}$$

$$E_{n\perp} = \frac{ie\omega_1\gamma}{2\epsilon_0}\frac{\mathrm{e}^{-i\omega_1 nR/cc}}{R} f_y(\gamma\theta,\phi), \tag{4.2}$$

where $f_{x,y}$ are functions given by equations (3.32) and (3.33). As is already described, the polarization is linear because both components have the same phase.

The amplitude E_{0n} and the direction of polarization α for each harmonic are given by

$$E_{0n} = \sqrt{|E_{n\parallel}|^2 + |E_{n\perp}|^2}, \tag{4.3}$$

$$\alpha_n = \tan^{-1}\left(\frac{E_{n\perp}}{E_{n\parallel}}\right). \tag{4.4}$$

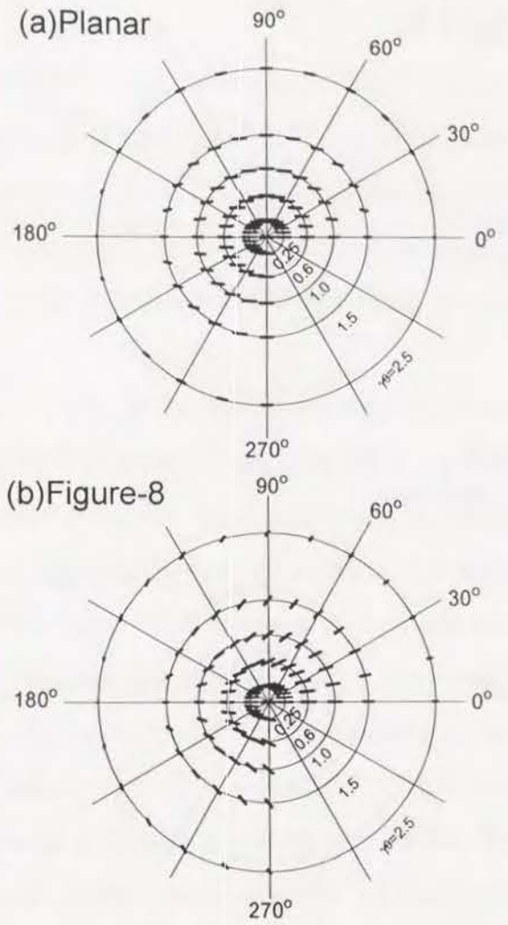

Figure 4.1. Spatial dependence of the amplitude and the direction of polarization for the fundamental radiation in the case of the (a) planar and (b) figure-8 undulators.

Figures 4.1 (a) and (b) show the spatial dependence of the direction and the amplitude for the fundamental radiation obtained from the planar and figure-8 undulators, respectively [26]. The K values are assumed to be 4.72 (=K, planar) and 3.34 (=K_x=K_y, figure-8). The length and the slope of each bar show the amplitude and the direction of polarization, respectively.

In the case of the planar undulator, the radiation is polarized nearly in the horizontal plane for values of $\gamma\theta$ smaller than 1.0, while for larger values of $\gamma\theta$, the direction of polarization rotates along the contour. In the case of the figure-8

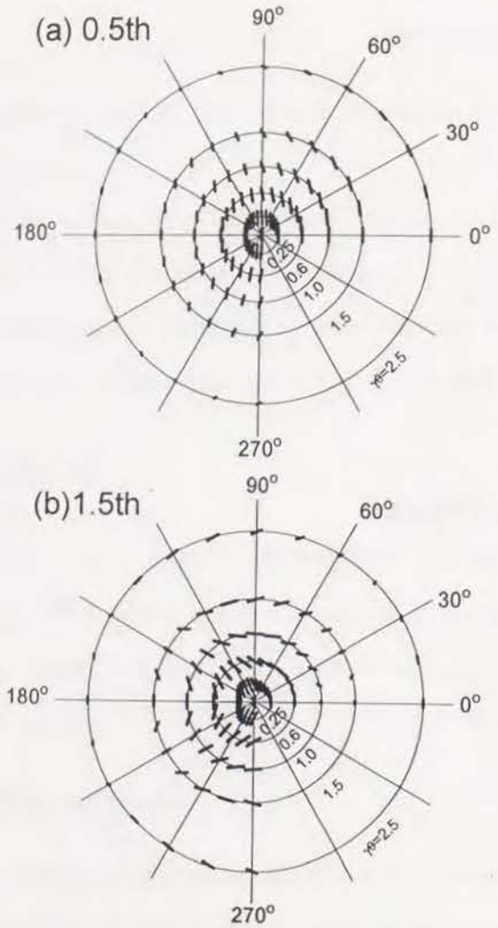

Figure 4.2. Spatial dependence of the amplitude and the direction of polarization for the (a)0.5th and (b)1.5th harmonics obtained from the figure-8 undulator.

undulator, the rotation of the direction of polarization along the contour is more remarkable than that of the planar undulator, which means that the degradation of the degree of polarization due to the angular divergence of the beam and the size of the aperture for extracting the SR beam, will be more remarkable.

The direction and the amplitude of polarization of the figure-8 undulator are symmetric and antisymmetric with respect to θ_y, while they are asymmetric with respect to θ_x. These characteristics can be explained by the asymmetry of the relation between β_x and β_y.

The slope of the direction of polarization is equal to zero both along θ_x and θ_y in the case of the planar undulator. On the other hand, that of the figure-8 undulator is increasing along the θ_y axis, which means that the degree of polarization degrades. Therefore, the coupling constant of the storage ring and the vertical size of the aperture should be as small as possible in order to obtain the high degree of polarization.

Figures 4.2 (a) and (b) show the spatial dependence of the direction and the amplitude for the 0.5th and 1.5th harmonics obtained from the figure-8 undulator. As well as the fundamental radiation, the direction and the amplitude are asymmetric with respect to θ_x for both harmonics. As for the 0.5th harmonic, the radiation is polarized in the vertical plane when observed on axis and the rotation of the direction of polarization for larger values of $\gamma\theta$ is not so remarkable as the fundamental, which will result in the higher degree of polarization. As for the 1.5th harmonic, the polarization on axis is vertical as well as the 0.5th harmonic, however, the rotation of the direction of polarization is more remarkable. Therefore, the degree of polarization will degrade more rapidly than that of the 0.5th harmonic.

4.2.2 Effects due to the angular divergence

Figures 4.3 (a) and (b) show the degradation of the degree of polarization due to the angular divergence of the beam for the planar and figure-8 undulators, respectively. In the case of the planar undulator, increase of both $\sigma_{x'}$ and $\sigma_{y'}$ causes the degradation, however, increase of either $\sigma_{x'}$ or $\sigma_{y'}$ does not degrade the degree of polarization. This is due to the fact that the slope of the direction of polarization is equal to zero both along θ_x and θ_y. In the case of the figure-8 undulator, degradation with respect to $\sigma_{y'}$ is remarkable. This is also equivalent to the discussion in the previous section. In order to achieve the high degree of polarization, $\sigma_{y'}$ should be small, which means that the coupling constant of the storage ring should be as small as possible.

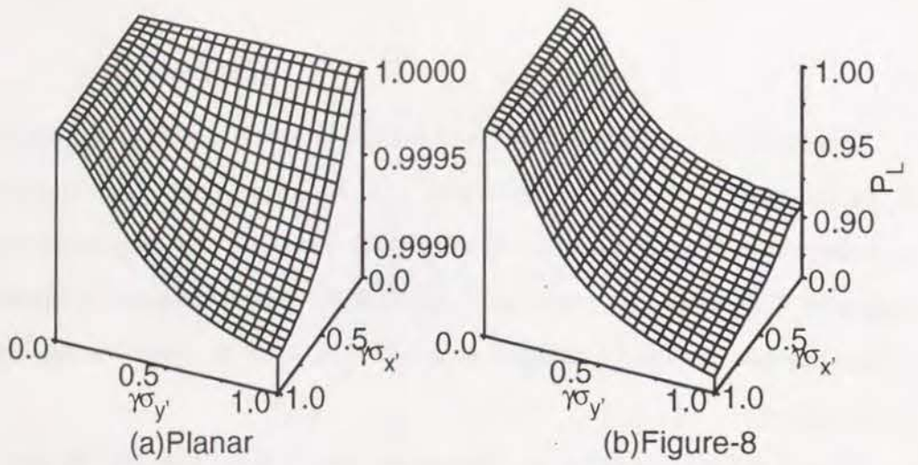

Figure 4.3. Degradation of the degree of polarization according to the angular divergence for the fundamental radiation obtained from the (a)planar and (b)figure-8 undulators.

Figures 4.4 (a) and (b) show the degradation of the degree of polarization due to the angular divergence of the beam for 0.5th and 1.5th harmonics of the figure-8 undulator, respectively. For both harmonics, the degradation due to $\sigma_{y'}$ is remarkable as well as the fundamental radiation. As for the 0.5th harmonic, however, the degradation is small. On the other hand, the degradation of polarization for 1.5th harmonic is very large. For example, P_L for the 1.5th harmonic is 0.63 when $\gamma\sigma_{x',y'} = 0.5$. On the other hand, that for the 0.5th harmonic is 0.98. From the facts described above, the 0.5th harmonic is more preferable than the 1.5th for obtaining the vertically polarized radiation.

4.3 Electric field of radiation

Substituting equation (3.25) into equation (2.13) directly, we obtain the electric field of radiation observed at the point far from the device. Because the spectrum is obtained by the Fourier transformation of the electric field, it is interesting to investigate the features of the electric field.

4.3.1 Time dependence

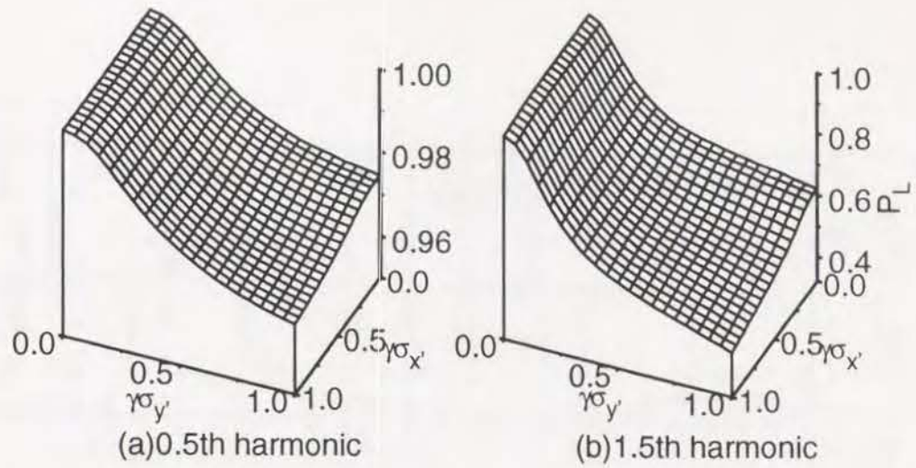

Figure 4.4. Degradation of the degree of polarization according to the angular divergence for the (a)0.5th and (b)1.5th harmonics obtained from the figure-8 undulator.

Figures 4.5 (a) and (b) show the on-axis electric field of radiation from the planar and figure-8 undulators, respectively. R means the distance between the observer and the source and T the period of the electric field. In the same figures, the deflection angles are also shown. The observer time means the time in the laboratory frame, not in the rest frame of the electron.

In the case of the planar undulator, the electric field forms a pulse at the time when the deflection angle is equal to zero. This is due to the fact that the time interval through which the deflection angle is smaller than γ^{-1} is very narrow, which is found from the figure showing the time dependence of the deflection angle. When the electric field shown in Fig. 4.5 (a) is expanded into a Fourier series, so many higher harmonics appear in the spectrum, which cause the unreasonable heat load. This has been already described in chapter 2.

In the case of the figure-8 undulator, the electric field does not form a pulse because the deflection angle is never equal to zero. Therefore, much less higher harmonics appear in the spectrum than the planar undulator.

Figures 4.6 (a) and (b) show the off-axis electric field of radiation obtained from the figure-8 undulator. The horizontal observation angle θ_x is assumed to be $-K_y/\gamma$ and K_y/γ, respectively. The horizontal angle is assumed to be zero in each case. It is

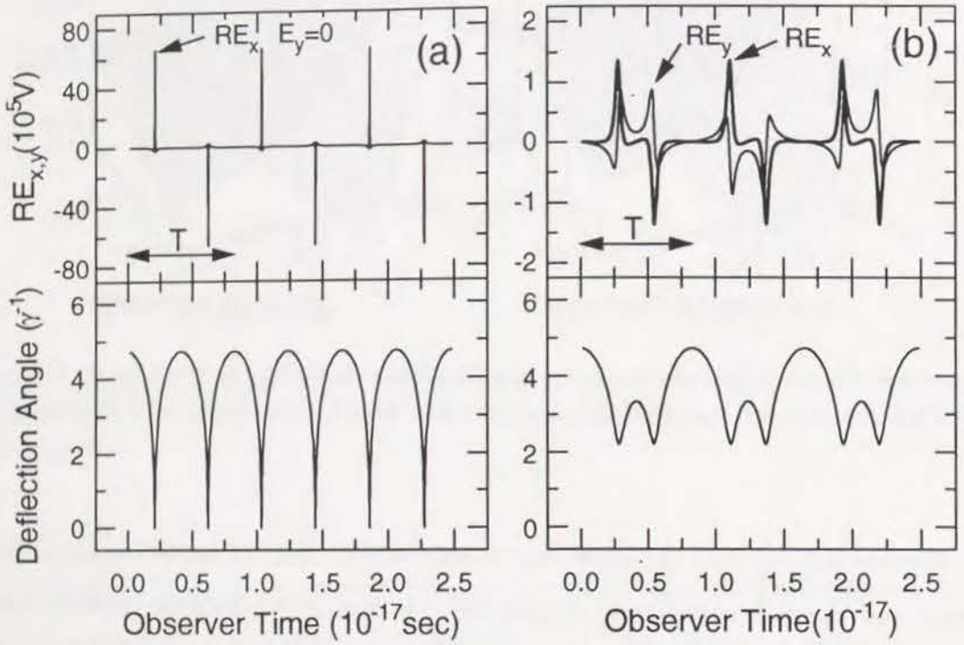

Figure 4.5. Above: On-axis electric field of radiation from the (a)planar and (b)figure-8 undulators. Below: Deflection angle of the trajectory for both undulators.

found from the figures that the electric field forms a pulse at the angle $\theta_x = -K_y/\gamma$, while it does not form a pulse at the angle $\theta_x = K_y/\gamma$. This is due to whether the effective deflection angle δ_{eff}, defined as

$$\delta_{eff} = \sqrt{(\theta_x - \beta_x)^2 + (\theta_y - \beta_y)^2}, \tag{4.5}$$

becomes equal to zero or not. The meaning of the effective deflection angle is the angle between the direction of observation and the direction of the electron motion. If the effective deflection angle becomes equal to zero at some part of the trajectory, the contribution of radiation will be the largest at that point. Therefore, the electric field forms a pulse.

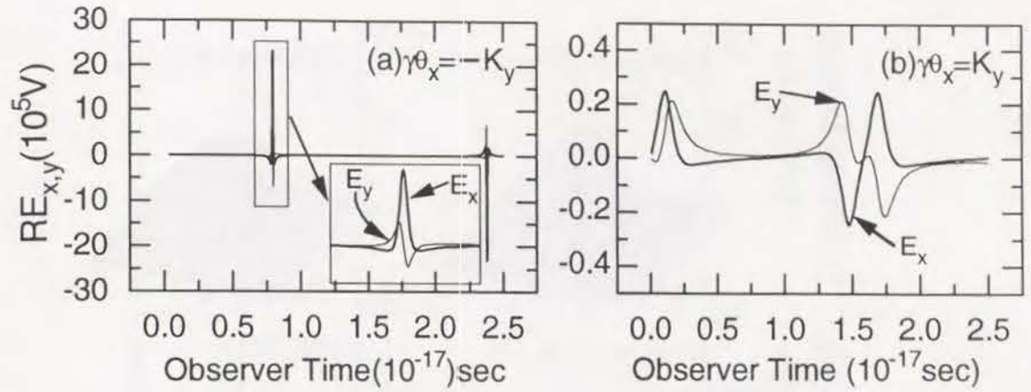

Figure 4.6. Electric field of radiation from the figure-8 undulator observed off axis.

4.3.2 Harmonics and polarization

In chapter 2, the radiation from the planar undulator was found to contain only the odd-number harmonics when observed on axis. This is due to the fact that the horizontal component of the electric field satisfies the periodic condition

$$E_x(t + T/2) = -E_x(t). \tag{4.6}$$

When E_x is expanded into a Fourier series, the even-number harmonics disappear due to the periodic condition (4.6). In the case of the figure-8 undulator, however, E_x does not satisfy the periodic condition (4.6), which is found from Fig. 4.5 (b). Therefore, even-number harmonic in addition to odd-number harmonics appear in the spectrum. As for E_y, integer harmonics disappear in turn, because of the periodic condition

$$E_y(t + T) = -E_y(t). \tag{4.7}$$

Therefore, only the half-odd-integer harmonics appear in the spectrum.

Summarizing the facts described above, integer harmonics are found to be horizontally polarized, while half-odd-integer harmonics vertically polarized. This is equivalent to the discussion in section 4.2.

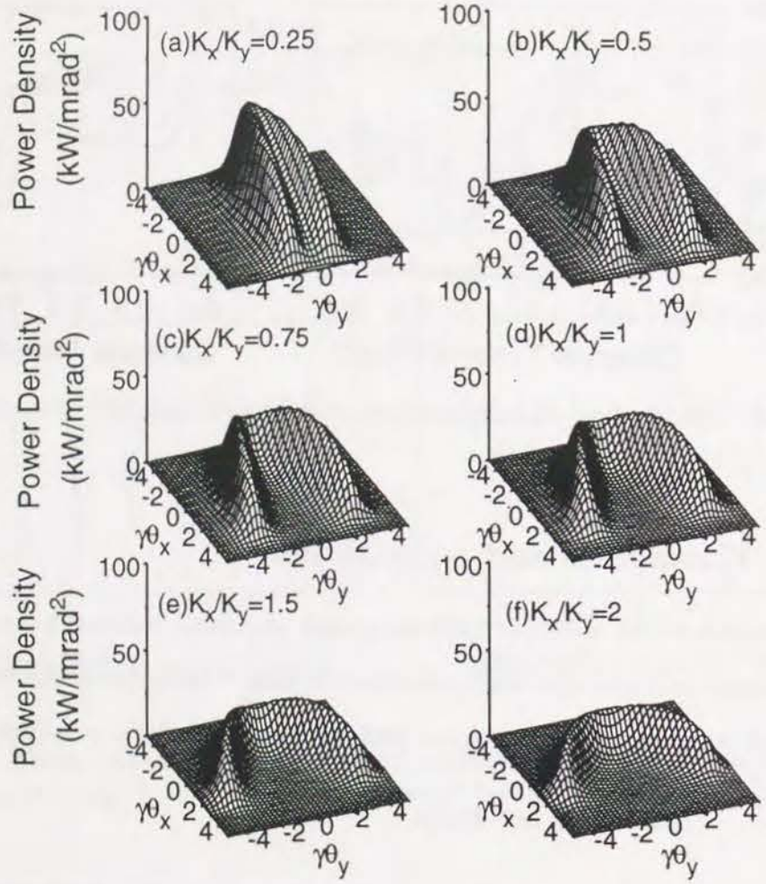

Figure 4.7. Spatial distribution of the power density for various values of the K ratio.

4.4 K-ratio dependence of radiation

So far, the ratio of the horizontal K value to the vertical, K_x/K_y, has been assumed to be constant and unity. In this section, the dependence of radiation on the K ratio is investigated.

4.4.1 Power density

First, the K-ratio dependence of the power density is discussed. Figures 4.7 (a)$\sim$(f) show the spatial distribution of the power density for various values of

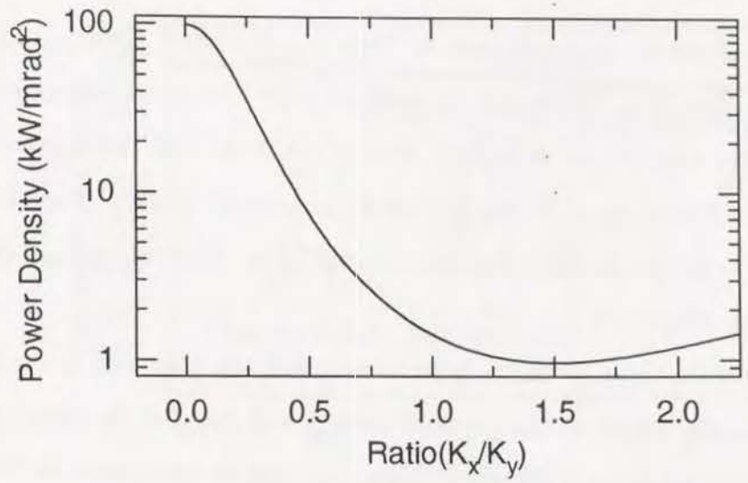

Figure 4.8. K-ratio dependence of the on-axis power density.

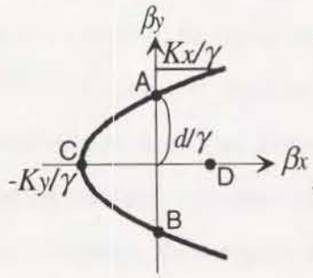

Figure 4.9. Relation between horizontal and vertical velocities.

K_x/K_y. In calculating the dependence, the value, $K = \sqrt{K_x^2 + K_y^2}$, is set to be constant (=4.72). Therefore, the energy of the first harmonic is fixed at 500 eV. It is found from the figures that the vertical angle of the V figure of distribution is increasing as the increase of the radio, K_x/K_y. In addition, the top of the V figure gets closer to the axis.

Figure 4.8 shows the K-ratio dependence of the on-axis power density. When $K_x/K_y = 0$, the device is simply a planar undulator and the power density is 98 kW/mrad^2. The on-axis power density takes its minimum at $K_x/K_y = 1.5$. When K_x/K_y is smaller than 1.5, the on-axis power density is reduced as the increase

of K_x/K_y. However, it is sufficient to keep K_x/K_y larger than 0.5 in order to suppress the heat load. When K_x/K_y is larger than 1.5, the on-axis power density is increasing as the increase of K_x/K_y. This is due to the fact that the top of the V figure of distribution closes to the axis as the increase of K_x/K_y. Therefore, the K ratio should be set to the value between 0.5 and 1.5 in order to suppress the on-axis power density effectively.

The minimum value of the K ratio to suppress the heat load is considered to depend on the K value. In the previous case, it was found to be about 0.5, which corresponds to the value of $K_x = 2.1$. This value can be interpreted as follows.

As described before, the relation between β_x and β_y reflects the distribution of the power density. In Fig. 4.9, the distance between the top of the V figure and the axis is K_y/γ. Let K_y be much larger than unity. If d is smaller than unity, then the on-axis power density may be high because the angle between the direction of the electron motion and the observer on axis is smaller than γ^{-1} and the radiated power from the electron having the velocity represented by the point A and B reaches to the axis. In turn, if d is larger than unity, the on-axis power density may be low. Therefore, the minimum value for d to keep the on-axis power density low, is considered to be unity. Because d/γ is the absolute value of β_y when $\beta_x = 0$, or $\omega_0 t = \frac{2n+1}{2}\pi$, where n is an integer, d is calculated as follows

$$d = \left| K_x \cos\left(\frac{2n+1}{2}\pi\right)\right| = \frac{K_x}{\sqrt{2}}. \tag{4.8}$$

Therefore, the minimum value for K_x to keep the on-axis power density low is considered to be 1.4. In practice, K_x slightly higher than 1.4 is necessary for suppressing effectively the heat load on axis. Thus the minimum value for K_x is considered as about 2, which is equivalent to the value estimated from Fig. 4.8.

The minimum K_x value of 2 to keep the on-axis power density low, is independent of K_x except the condition that K_y is larger than unity. This fact is important for designing the figure-8 undulator, to be discussed in chapter 5.

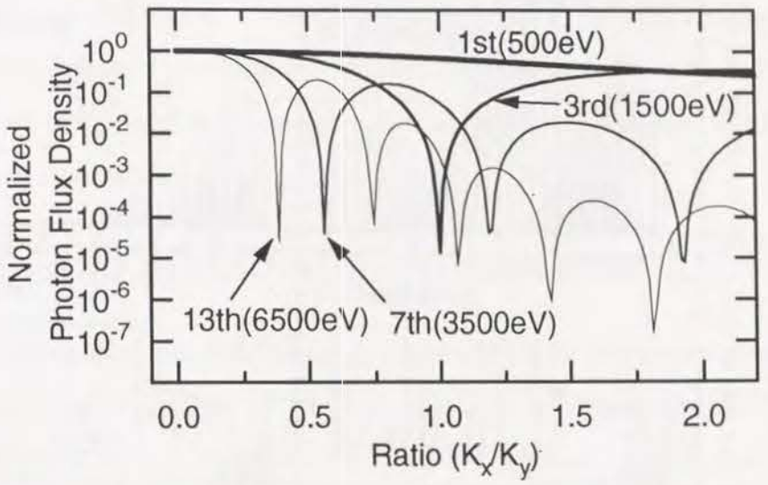

Figure 4.10. K-ratio dependence of the photon flux density.

4.4.2 Photon flux density

Next, the K-ratio dependence of the photon flux density is discussed. Figure 4.10 shows the K-ratio dependence of the on-axis photon flux density for various harmonics. Each value is normalized by the value at $K_x/K_y = 0$. It is found from the figure that the unnecessary higher harmonics is reduced rapidly as the increase of K_x/K_y, while the degradation of the fundamental is not so remarkable.

What is more interesting is that some specific harmonic can be eliminated completely by adjusting K_x/K_y. For exarnple, the third harmonic is eliminated completely when $K_x/K_y = 1.0$. As described before, the even number harmonics can be eliminated by using an ordinary crystal monochromator, therefore only the fifth harmonic or higher may remain after monochromatization by a monochromator. However, the reflectivity of the fifth harmonic or higher is considered to be much smaller than that of the fundamental, therefore the intensity of higher harmonics will be quite low.

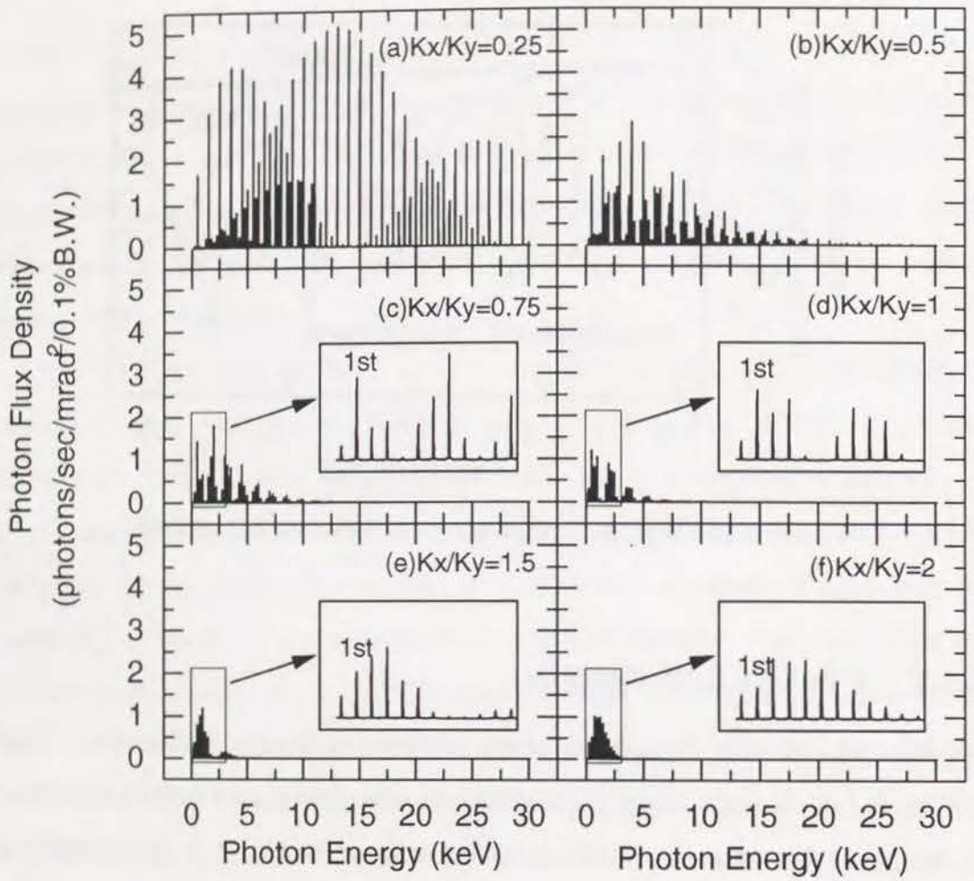

Figure 4.11. Spectra of the figure-8 undulator for various values of the K ratio.

4.4.3 Spectrum

Figures 4.11 (a)∼(f) show the spectra for various values of the K ratio. As the increase of the K ratio, the contribution of higher harmonics to the spectrum becomes smaller. Although considerable higher harmonics remain in the spectrum when $K_x/K_y = 0.25$, they are suppressed considerably when K_x/K_y is larger than 0.5. This is equivalent to the discussion in section 4.4.

In Figs. 4.11 (c)∼(f), the spectra in the energy range up to 3 keV are also shown. From these figures, it is found that the intensity for the fundamental is getting lower as the increase of the K ratio, while those of the half-odd-integer

harmonics are getting higher. This is easily understood by considering the fact that those half-odd-integer harmonics are derived from the vertical undulator with the period length of $2\lambda_u$ and that the larger K ratio means the stronger magnetic field of the vertical undulator.

4.5 Spatial distribution of radiation

Investigating the spatial distribution of radiation is important for designing the components of the beamline, in particular the mirror for focusing the SR beam and the X-Y slit for extracting the SR beam and eliminating the photons in the unnecessary spectral part.

4.5.1 Partial power density

Integrating equation (3.31) over ω, we obtain the power contained in the n-th harmonic. We call it a partial power density for the n-th harmonic. If the partial power density for the fundamental is high and that for higher harmonics is low, the radiation is reasonable for the utilization of the fundamental radiation.

Figures 4.12 (a)∼(d) show the spatial distribution of the partial power density for various harmonics obtained from the planar undulator. Distributions along θ_x and θ_y axes are shown with the on-axis value. For each harmonic, the on-axis value is the maximum. As the increase of the number of harmonic, the on-axis power density increases, which means that the ratio of the partial power density for the fundamental to the total power density will be low. In fact, the ratio is calculated as $0.31/98 = 3.2 \times 10^{-3}$. Therefore, only 0.3% of the power radiated to the axis is available.

Figures 4.13 (a)∼(d) show the spatial distribution of the partial power density for various harmonics obtained from the figure-8 undulator. Although the distribution is symmetric with respect to the θ_y axis, it is asymmetric with respect to the θ_x axis. This is due to the asymmetry of β_x with respect to β_y, which is already discussed

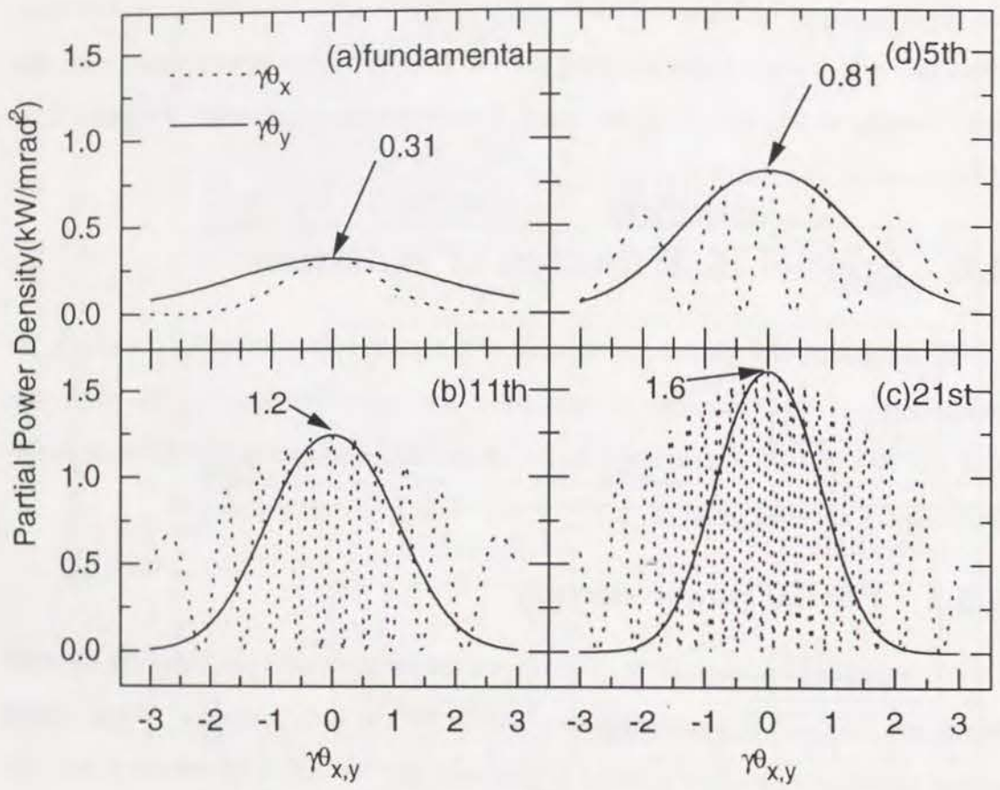

Figure 4.12. Angular distribution of the partial power density for various harmonics obtained from the planar undulator.

in section 3.6. As for the fundamental, the on-axis value is not the maximum. The maximum of the power density is located at the angle slightly shifted to $+\theta_x$. It is found from the figures that the on-axis power density is reduced as the increase of the harmonic number. Although the on-axis power density for the fifth harmonic is comparable to that of the fundamental, that of the other higher harmonics is much lower than that of the fundamental. The reason is that the power for higher harmonics distributes mainly off axis, which is similar to the total power density. In this case, the ratio of the partial power density for the fundamental to the total power density is calculated as $0.22/1.4 = 0.16$. Although this value is lower than that of the helical undulator (partial/total=1.0, because no higher harmonics are

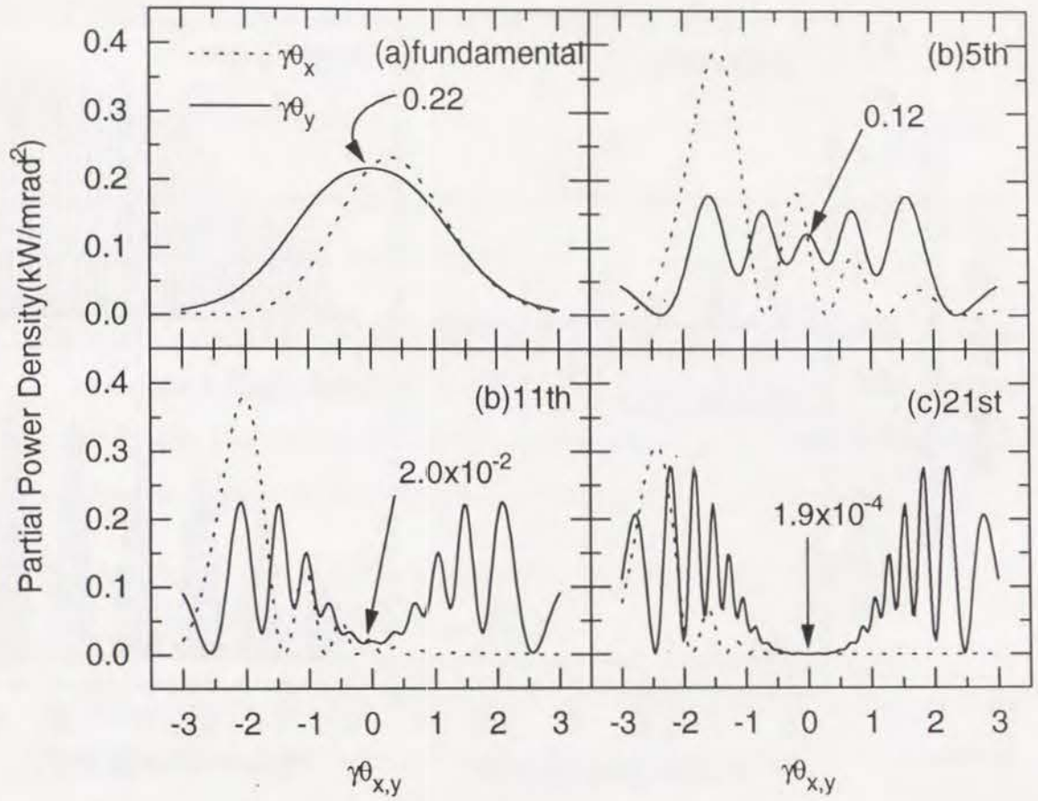

Figure 4.13. Angular distribution of the partial power density for various harmonics obtained from the figure-8 undulator.

observed on axis!), it is much higher than that of the planar undulator.

Because the partial power density for higher harmonics distributes mainly off axis, larger size of the aperture results in larger contribution of higher harmonics to the spectrum. From Fig. 4.13 (a), it is found that in order to extract most of the power contained in the fundamental radiation, the aperture should be as large as $2/\gamma$. However, this may result in the unreasonable heat load caused by higher harmonics. In order to avoid such a situation, the size of the aperture should be as small as $1/\gamma$.

4.5.2 Spectrum

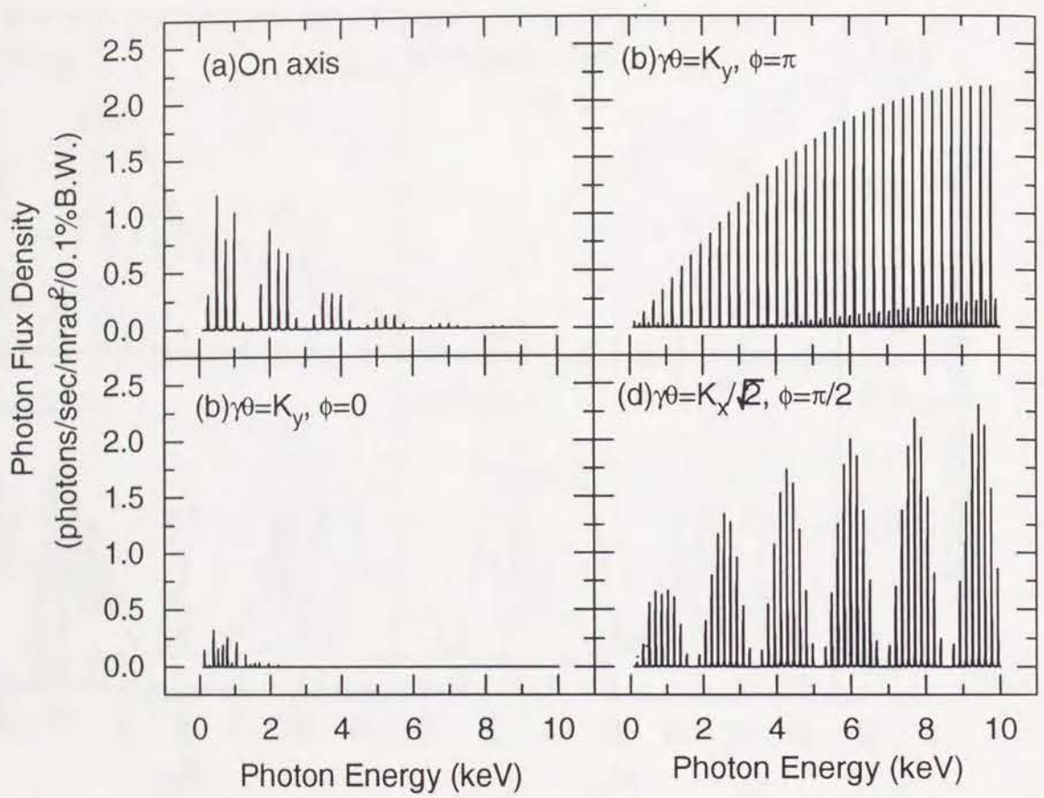

Figure 4.14. Spectra of the figure-8 undulator for various angles of observation.

Figures 4.14 (a)$\sim$(d) show the spectra obtained from the figure-8 undulator for various angles of observation. The observation angles shown in Figs. 4.14 (b)$\sim$(d) correspond to the points C, D and A indicated in Fig. 4.9, respectively. Although the values of $\gamma\theta$ in Fig. 4.14 (b) and (c) are the same, the spectra are quite different. When $\phi = 0$, the contribution of higher harmonics is quite small. On the other hand, so many higher harmonics appear in the spectrum when $\phi = \pi$. This is due to the fact that the electric field of radiation forms a pulse when observed at $\gamma\theta = K_y$ and $\phi = 0$, as shown in Fig. 4.6 (a) because the effective deflection angle becomes equal to zero at some part of the trajectory. Similarly, so many higher harmonics appear in the spectrum when observed at $\gamma\theta = K_x/\sqrt{2}$ and $\phi = \pi/2$. This is also explained

by the discussion on the effective deflection angle.

4.6 Conclusions

In this chapter, various characteristics of figure-8-undulator radiation were investigated. The results are summarized below.

1. Unlike the planar undulator, the slope of the direction of polarization increases along the θ_y axis. Therefore, the horizontal angular divergence of the electron beam and the vertical size of the aperture should be as small as possible in order to achieve the high degree of polarization.

2. The photon flux density of some specific harmonic can be eliminated completely by adjusting the K ratio, K_x/K_y.

3. The on-axis electric field of radiation from the figure-8 undulator does not form a pulse because the deflection angle never becomes equal to zero. Therefore, higher harmonics are suppressed effectively.

4. Ideal utilization of the fundamental radiation is possible because most of the power of the higher harmonics exists off axis.

The facts described in items 3 and 4 are equivalent to the case of the helical undulator. This is natural because the figure-8 undulator is based on the combination of two helical undulators.

Chapter 5

Design of the Figure-8 Undulator

5.1 Introduction

Recently, it has been decided that the figure-8 undulator should be installed in the Super Photon ring-8GeV, or the SPring-8, for supplying linearly polarized SR in the VUV and SX regions. The SPring-8, now under construction, is the SR facility using the 8-GeV electron (positron) beam for supplying SR with a high brilliance and a wide spectral range of energies. Because the energy of the electron beam is extremely high, it is natural to use the figure-8 undulator instead of the planar undulator for supplying VUV and SX with a linear polarization.

In designing an ID, the requested performances, i. e., the characteristics of radiation desired by the users, should be concerned. In the figure-8-undulator case, not only the high brilliance but also the high degree of polarization and low on-axis power density are desired. In addition, the available energy range of the fundamental radiation should be as wide as possible.

If there are no limitations on the dimensions of the ID, it is easy to design any type of ID. In particular, it may be easier to construct an ID having not only the vertical but also horizontal magnetic fields such as the helical and figure-8 undulators. In fact, there are some limitations. Among them, the most troublesome is

that the horizontal gap of the ID should be quite large, typically larger than 90 mm. Therefore, it is impractical to adopt the three-dimensional configuration, i. e., the configuration with magnet arrays not only in the vertical plane but also in the horizontal plane.

In this chapter, some magnet configurations for the figure-8 undulator are discussed and the most fitted one is determined. After that, the size of each magnet block is determined considering the requested performances. In addition, discussions on the magnet configuration to generate the ideal trajectory of the figure-8 undulator are given. Finally, effects of the magnetic fields on the electron beam in the storage ring are investigated in the case of the determined magnet configuration.

5.2 Requested performances

What performances are requested for the ID is quite important for designing the device. In the figure-8-undulator case, the requested performances and ID parameters at the SPring-8 are shown in Table 5.1.

Table 5.1. Requested performances and ID parameters for the figure-8 undulator at the SPring-8.

Available Energy	100 eV∼5000 eV
On-axis power density	as low as possible
Brilliance	as high as possible
Polarization	linear
Minimum Gap	20 mm
Remanent Field of Permanent Magnet	1.3 T
Total Width of an ID	106 mm
Total Length of an ID	4.5 m

5.3 Planar structure for helical undulators

As described before, the magnetic fields in the figure-8 undulator can be realized by a slight modification of the helical undulator. To be concrete, by changing the period length of the horizontal magnetic field from λ_u to $2\lambda_u$, where λ_u is the period length of the helical undulator. Therefore, we should consider the design of the helical undulator before considering the design of the figure-8 undulator.

After the study on the ID with a helical magnetic field, or the helical undulator, by Kincaid [15], many efforts have been devoted to construct such devices. This is due to the ability of the helical undulator to arrow the ideal utilization of the fundamental radiation and the interesting demand for circularly-polarized radiation in the study of magnetic materials, biological molecules and other systems that exhibit circular dichroism.

If there is no limitation on the size of the aperture of the beamline, the simplest way to make such devices is to superpose two planar undulators, as shown in Fig. 2.11. In order to install the devices in the storage ring, however, the horizontal aperture should be large for the beam injection and the beam life time. Therefore, a planar structure should be adopted.

So far, four types of configuration of the magnets are considered in order to realize the helical undulator having the planar structure. It is important to compare the performances between them to determine which configuration should be adopted.

5.3.1 Configuration of magnets

Figures 5.1 (a)$\sim$(d) show various configurations of magnets to realize helical magnetic fields which have been proposed and developed so far. Each configuration has magnet arrays more than two, which are all standard Halbach types except Fig. 5.1 (b).

Figure 5.1 (a) is the so-called Helios, proposed by Elleaume [13]. The upper magnet array generates the vertical field and the lower array generates the horizontal

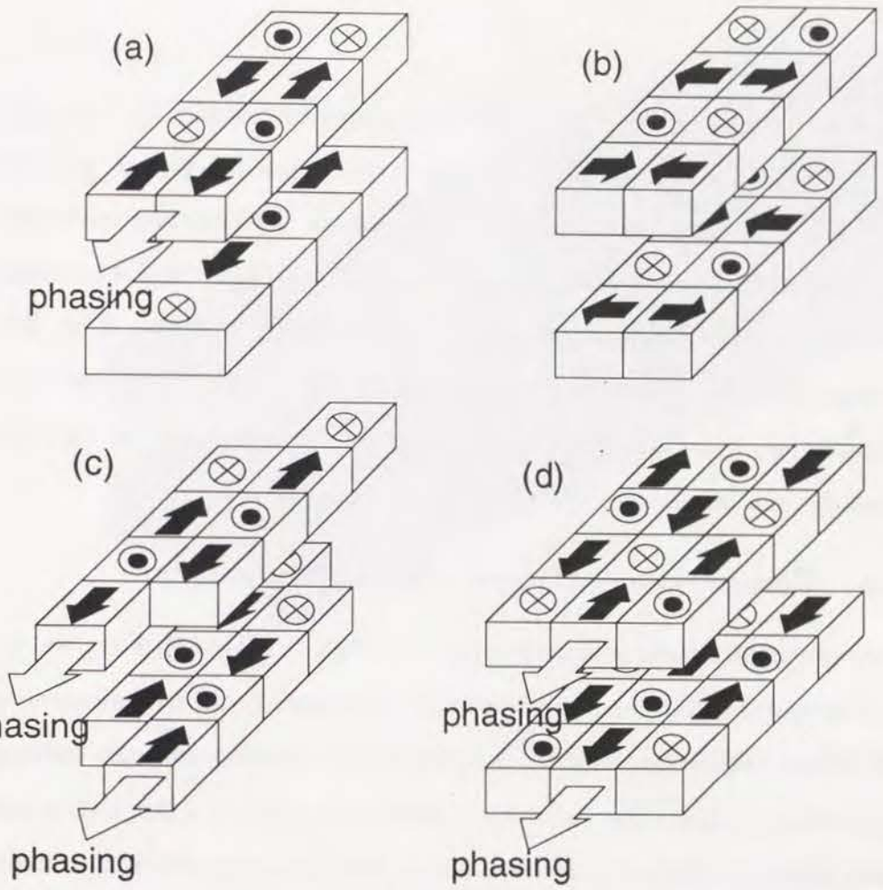

Figure 5.1. Various configurations of magnets to realize helical magnetic field.

field. The phasing, which means the changing of the helicity, can be done by sliding the upper array and changing the relative distance between the arrays upper and lower. In order to generate a circular helix, the half gaps between the axis and the arrays must be changed independently.

Figure 5.1 (b) is the configuration proposed by Walker and Diviacco [28]. Each magnet array is similar to the Halbach configuration but the magnet blocks magnetized in the z direction are replaced by those in the x direction. The magnet blocks magnetized in the y direction generates the horizontal field and those in the x direction do the vertical. It is clear from the figure that the phasing cannot be

done.

Figure 5.1 (c) is the so-called APPLE, proposed by Sasaki [29]. Four standard Halbach arrays are contained. Each magnet block has the role to generate the vertical and horizontal magnetic fields. Two arrays, for example, upper left and lower right, are movable in order to obtain linear, elliptical and circular polarizations.

Figure 5.1 (d) is a configuration recently proposed by Kitamura et al. [30],[31]. Six standard Halbach arrays are contained. Four outer arrays generate the horizontal field, while two inner arrays below and above the axis generate the vertical field. The helicity can be changed by sliding the two inner arrays.

5.3.2 Comparison between each configuration

Let us compare each configuration shown in Figs. 5.1 (a)$\sim$(d). First, we consider the performance with respect to the field measurement. In the field measurement in an ID, a Hall probe is usually used. A Hall probe is a device to measure the magnetic field by using the Hall effect, whereby a voltage is created in a thin slab of material (usually a semiconductor) in which a current flows perpendicular to the direction of the magnetic field. By measuring the voltage, the magnetic field can be determined. In such a measurement using the Hall probe, what is the most troublesome is the so-called planar Hall effect. This is a phenomenon that an additional voltage is created by a magnetic field not perpendicular but parallel to the plane on which the Hall probe lies [32]-[34]. Therefore, an accurate measurement of the vertical and horizontal fields is difficult at the place where both horizontal and vertical fields exist. In this point of view, the configurations shown in Figs. 5.1 (a) and (d) are preferable.

Next, the performance is considered with respect to the strength of the magnetic field. It is easily understood that the configuration whose achievable magnetic field is the lowest is that shown in Fig. 5.1 (a). This is due to the fact that both horizontal and vertical fields are generated by magnet array(s) placed only at one side, below

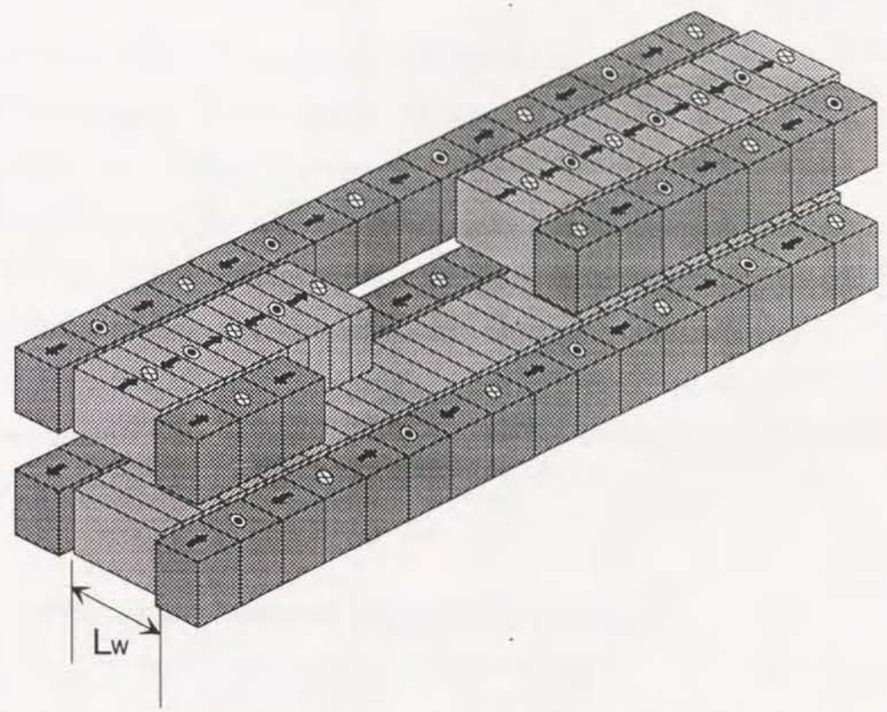

Figure 5.2. An example of the magnet configuration for the figure-8 undulator.

and above the axis. On the other hand, other three types are considered to be equivalent, except slight differences.

5.4 Configuration for the figure-8 undulator

In considering the magnet configuration for the figure-8 undulator, we should concern with the fact that the period length of the horizontal magnetic field is twice as long as that of the vertical. In this point of view, the configuration which can generate the horizontal and vertical magnetic fields independently is preferable. Therefore, the configurations shown in Figs. 5.1 (a) and (d) are considered to be fitted for the figure-8 undulator. Considering the strength of the magnetic field, the best configuration is that shown in Figs. 5.1 (d). An example of the configuration for the figure-8 undulator is shown in Fig. 5.2.

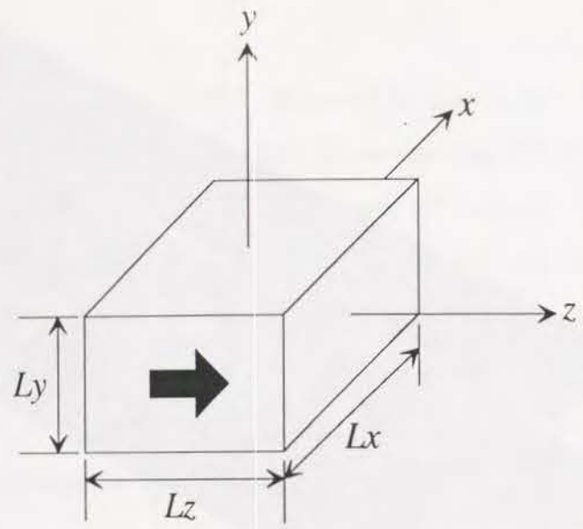

Figure 5.3. Parallelepiped permanent magnet block.

The four outer arrays generate the horizontal field, while the inner two arrays generate the vertical field. We call the former the vertical undulator and the latter the horizontal undulator, according to the orbital plane of the electron moving in each field.

5.5 Size of magnet blocks

In the previous section, the configuration of magnets for the figure-8 undulator has been decided. Next, the size of each magnet block is discussed.

5.5.1 Calculation of the magnetic field generated by a permanent magnet block

In general, the analysis of the magnetic field in a system containing the coil with current, soft iron for the yoke and other materials with high permeability, is difficult and cannot be solved analytically. However, in the ID using only the permanent magnet materials such as the rare-earth-cobalt and rare-earth-iron-boron,

the analysis is more simple. The magnetic field can be considered as the sum of the magnetic field generated by each magnet block because the permeability of such material is almost equal to unity. Therefore, the magnetic field generated by magnet block(s) with an arbitrary shape and magnetization can be obtained by dividing the block into small pieces and summing up the magnetic fields generated by individual piece. In order to do this, the expression for the magnetic field generated by a parallelepiped permanent magnet block should be derived. According to references [35]$\sim$[37], the magnetic fields generated by the magnet block with a magnetization M in the z direction, as shown in Fig. 5.3, are given by

$$B_x = -\frac{\mu_0 M}{4\pi} \sum_{\epsilon_x\epsilon_y\epsilon_z} \epsilon_x\epsilon_y\epsilon_z \times \operatorname{argsh}\left[\frac{y-\epsilon_y L_y/2}{\sqrt{(x-\epsilon_x L_x/2)^2+(z-\epsilon_z L_z/2)^2}}\right], \tag{5.1}$$

$$B_y = -\frac{\mu_0 M}{4\pi} \sum_{\epsilon_x\epsilon_y\epsilon_z} \epsilon_x\epsilon_y\epsilon_z \times \operatorname{argsh}\left[\frac{x-\epsilon_x L_x/2}{\sqrt{(y-\epsilon_y L_y/2)^2+(z-\epsilon_z L_z/2)^2}}\right], \tag{5.2}$$

$$B_z = \frac{\mu_0 M}{4\pi} \sum_{\epsilon_x\epsilon_y\epsilon_z} \epsilon_x\epsilon_y\epsilon_z \tan^{-1}\left[\frac{(x-\epsilon_x L_x/2)(y-\epsilon_y L_y/2)}{(z-\epsilon_z L_z/2)} \times \frac{1}{\sqrt{(x-\epsilon_x L_x/2)^2+(y-\epsilon_y L_y/2)^2+(z-\epsilon_z L_z/2)^2}}\right], \tag{5.3}$$

with

$$\operatorname{argsh}(x) = \ln(x+\sqrt{x^2+1}), \tag{5.4}$$

$$\epsilon_{x,y,z} = +1 \text{ or } -1. \tag{5.5}$$

Using equations (5.1)$\sim$(5.3), the calculation of the magnetic field generated by arbitrary magnet configurations is possible.

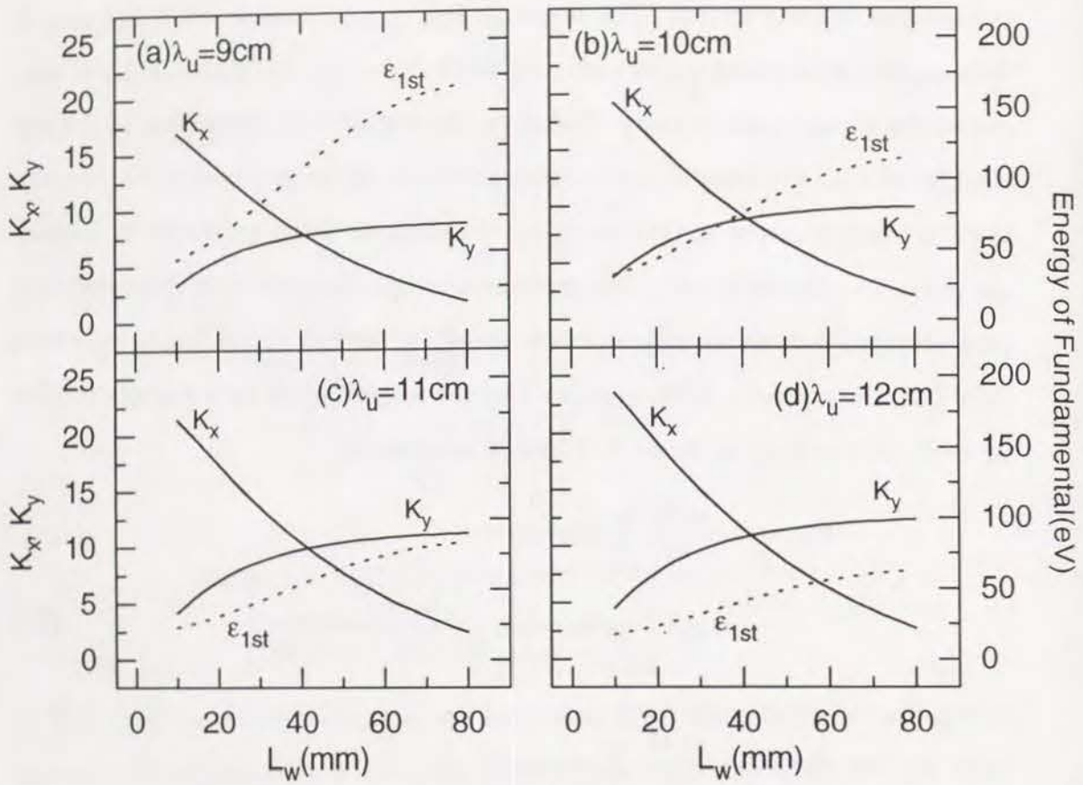

Figure 5.4. Solid line: K values as a function of the width of the horizontal undulator at the gap of 20 mm for the period length of (a)9 cm, (b)10 cm, (c)11 cm and (d)12 cm. Dotted line: Energy of the fundamental radiation calculated using the K values shown by the solid lines.

5.5.2 Achievable K value

First, the achievable K value is considered. The variable parameters to be determined are the period length, the widths and heights of both (horizontal and vertical) undulators. Among these, we determine the height of the horizontal and vertical undulators as 35 mm and 40 mm because of the mechanical limitation of the support. Therefore, the period and the width can be varied.

Figures 5.4 (a)$\sim$(d) show the K values as a function of the width of the horizontal undulator at the minimum gap (20 mm) for various values of the period length. In the same figures, the corresponding energy of the fundamental radiation is also

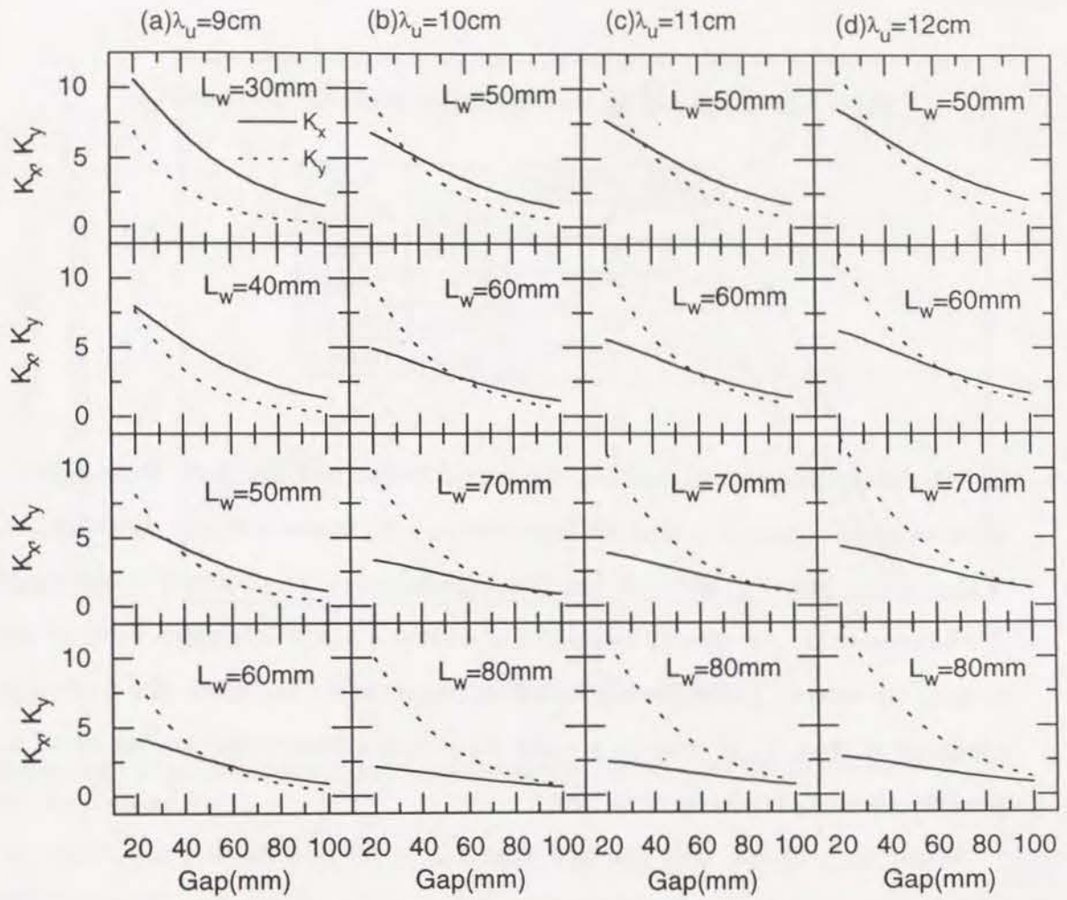

Figure 5.5. Gap dependence of the magnetic field for various values of the width of the horizontal undulator and the period length.

shown. It is found from the figures that in order to obtain the fundamental radiation of 100 eV, L_W should be smaller than 37 mm and 60 mm when λ_u is equal to 9 cm and 10 cm, respectively. In the other two cases, there is no limitation with respect to the minimum energy of 100 eV of the fundamental.

5.5.3 Gap dependence

Next, the gap dependence of the magnetic field is considered. Figures 5.5 (a)$\sim$(d) show the gap dependence of the magnetic field for various values of L_W

Table 5.2. Designs of figure-8 undulator fitted for the condition.

Name of design	λ_u	L_W
A	10 cm	60 mm
B	11 cm	60 mm
C	11 cm	70 mm
D	12 cm	60 mm
E	12 cm	70 mm

and the period length. In deciding the period length and L_W from these figures, what we should consider is that the higher value of K_x causes not only the reduction of the on-axis power density but also the degradation of the photon flux density of the fundamental. As already described in section 4.4, the minimum value of K_x to keep the on-axis power density low, is estimated as 2. Therefore, the preferable condition is that K_x is close to 2 when K_y is larger than unity, and as small as possible when K_y is smaller than unity.

When $\lambda_u = 9$ cm, only the case that $L_W = 60$ mm fits the condition. In other cases, K_x is too high and the degradation of the photon flux density of the fundamental will be remarkable. When $\lambda_u = 10$ cm, 11 cm and 12 cm, two cases that $L_W = 60$ mm and 70 mm fit the condition. In the case that $L_W = 50$ mm, K_x is too high. On the other hand, K_x is too low in the case that $L_W = 80$ mm. Among these cases, $(\lambda_u, L_W) = (9$ cm, 60 mm) and $(\lambda_u, L_W) = (10$ cm, 70 mm) do not satisfy the condition that the obtainable energy of the fundamental radiation should be as low as 100 eV.

Summarizing the discussions above, there are five designs which are considered to be fitted for the condition. They are shown in Table 5.2.

5.5.4 Brilliance and power density

In order to determine which design is the best among the cases discussed in the previous section, we should calculate the peak brilliance and the on-axis power density to be obtained practically. Figure 5.6 shows the peak brilliance of the fundamental radiation from the figure-8 undulator for the designs A∼E. The ring parameters used in the calculation are shown in Table 5.3

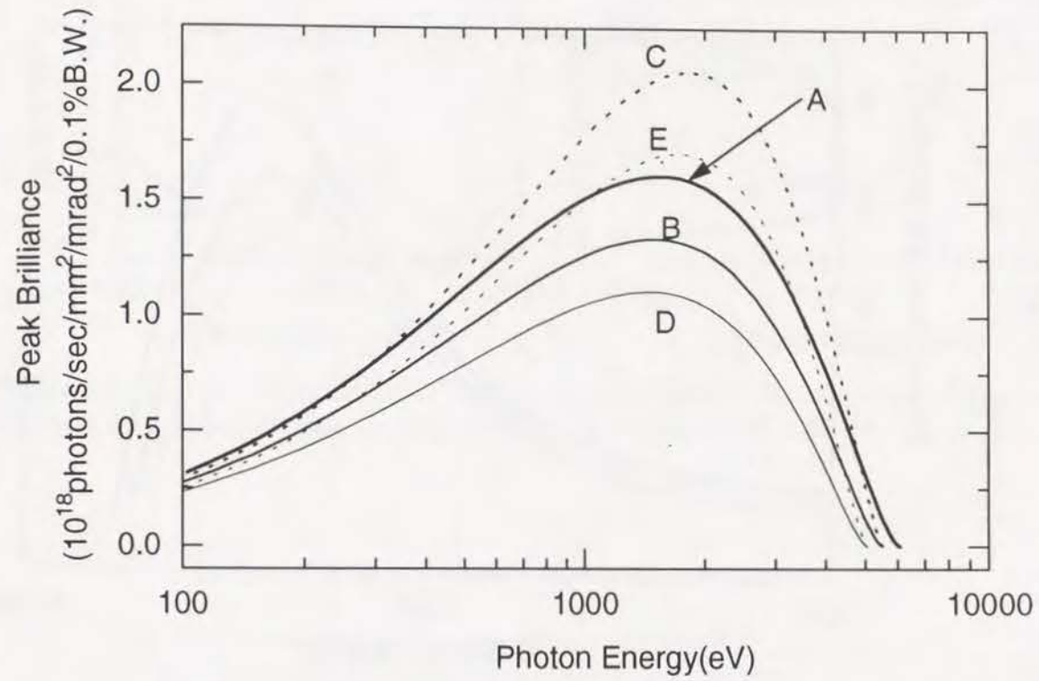

Figure 5.6. Peak brilliance of the fundamental radiation from the figure-8 undulator for the designs A∼E.

It is found from the figure that the highest brilliance can be obtained by adopting the design C in most of the required energy range. In the design D, the brilliance is about half of that in the design C. In general, the brilliance in the designs for L_W of 60 mm is lower than those for L_W of 70 mm. This is because K_y increases with the increase of L_W.

Figure 5.7 shows the on-axis power density from the figure-8 undulator for the designs A∼E. The maximum on-axis power density is obtained at 2500 eV in the design C. In general, the on-axis power density in the designs for L_W of 60 mm is lower than those for L_W of 70 mm.

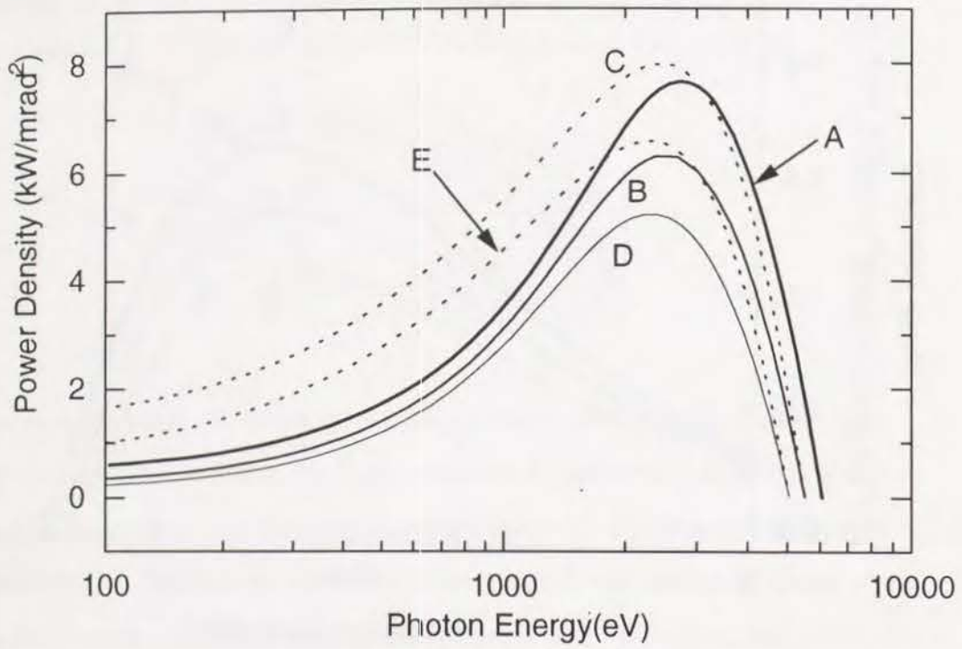

Figure 5.7. On-axis power density from the figure-8 undulator for the designs A∼E.

From Figs. 5.6 and 5.7, it is found that the best design cannot be decided, because the reduction of the on-axis power density causes the degradation of the brilliance of the fundamental. In other words, the designs A∼E are considered to be all acceptable.

For comparison, the peak brilliance and the on-axis power density obtained from the designs for λ_u of 10 cm and L_W of 50 mm and 80 mm are shown in Figs 5.8 (a) and (b). As for the brilliance, that from the design for L_W of 50 mm is a little too low, while as for the on-axis power density, that from the design for L_W of 80 mm is a little too high. Therefore, the two designs are not preferable.

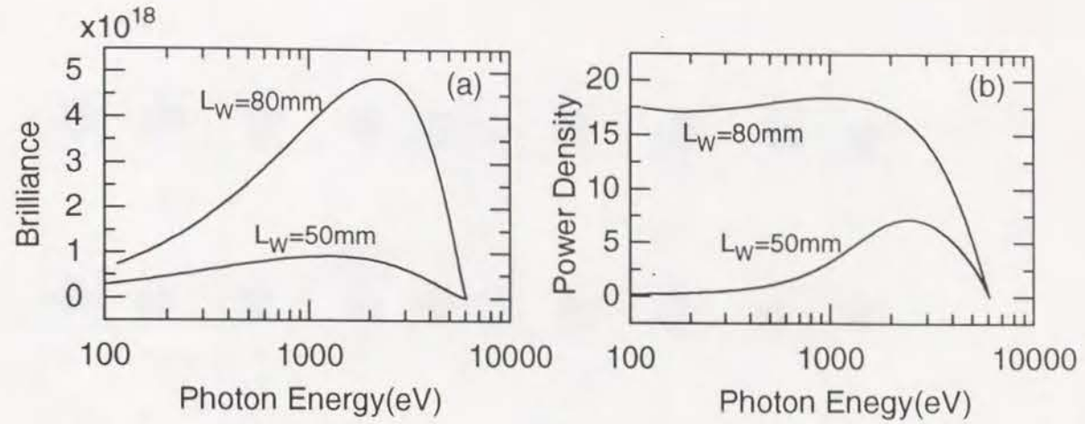

Figure 5.8. (a)Peak brilliance and (b)On-axis power density for two cases of L_W values of 50 mm and 80 mm. λ_u is assumed to be 10 cm in each case.

Table 5.3. Ring parameters used in the calculation.

Electron Energy	8 GeV
Average Current	100 mA
Natural Emittance	7.0×10^{-9} m·rad
Coupling Constant	0.02
Horizontal Betatron Value	24 m
Vertical Betatron Value	9 m

5.6 Consideration on the ideal trajectory

In section 3.2.2, the ideal trajectory of the figure-8 undulator was found to be impractical because the magnetic field should be discontinuous. It is, however, important to investigate the magnetic configuration to make the ideal trajectory.

In order to make a trajectory similar to the ideal one, a magnet configuration as shown in Fig. 5.9 is considered. The trapezoidal magnet plays a role to suppress the leakage of the magnetic flux. If there is no leakage of the flux, the magnetic field generated by such a magnetic configuration may be the ideal one. In fact, however, the practical magnetic field is far from the ideal one, as shown in Fig. 5.10. In the calculation, the values of H_c, λ_u and g_2 are fixed to be 15 mm, 100 mm and 40 mm, respectively.

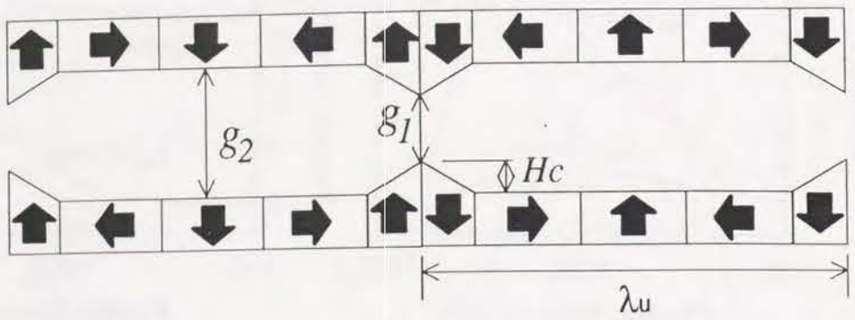

Figure 5.9. Example of a magnetic configuration to make a trajectory similar to the ideal one.

Figures 5.11 (a) and (b) show the spectra obtained from the ordinary figure-8 undulator and the magnetic configuration shown in Fig. 5.9, respectively. In the calculation, the respective parameters of the number of periods, the electron energy and the average current are used as 10, 8 GeV and 100 mA. It is clear from the figures that the ordinary figure-8 undulator is preferable with respect to the photon flux density of the fundamental and the contribution of the higher harmonics. In addition, the magnetic configuration shown in Fig. 5.9 has a disadvantage that the practical value of the gap is regarded not as g_2 but as g_1, which means that the achievable magnetic field may be much lower.

If H_c is smaller, the leakage of the flux may be larger, which results in much more difference between the practical and ideal fields. In turn, if H_c is larger, the practical field may be more close to the ideal one but the achievable magnetic field may be much lower. Therefore, we can say that the magnetic configuration of the ordinary figure-8 undulator is the best one.

5.7 Effects on the electron beam in the storage ring

In installing the ID in the storage ring, the most desirable situation is that the

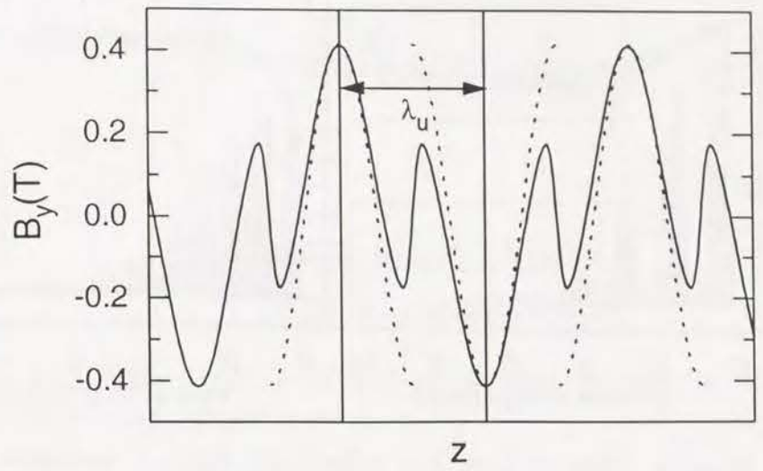

Figure 5.10. Magnetic field obtained from the magnetic configuration shown in Fig. 5.9. The dotted line shows the ideal magnetic field.

fields of the ID do not have any effect on the electron beam. In other words, the ID field should be regarded as the so-called drift space. In practice, however, there are some effects due to field errors of magnets and the nonuniformity of the field.

5.7.1 Field integral

When the electron beam crosses an ID, it experiences the deflection (θ) and the displacement (δ) between the entrance and the exit of the ID due to the field error of the magnets, as shown in Figs. 5.12 (a) and (b). They are calculated as

$$\theta_{x,y} = \frac{e}{\gamma mc} \int_{-\infty}^{\infty} B_{y,x}(z) dz, \tag{5.6}$$

$$\delta_{x,y} = \frac{e}{\gamma mc} \int_{-\infty}^{\infty} \int_{-\infty}^{z} B_{y,x}(z') dz' dz, \tag{5.7}$$

where the subscripts x and y mean the values of x and y components, respectively. The terms of integral are often called the first and second field integrals of the ID. It is possible to eliminate the both field integrals by a careful adjustment of magnets and steering coils placed before and after the ID.

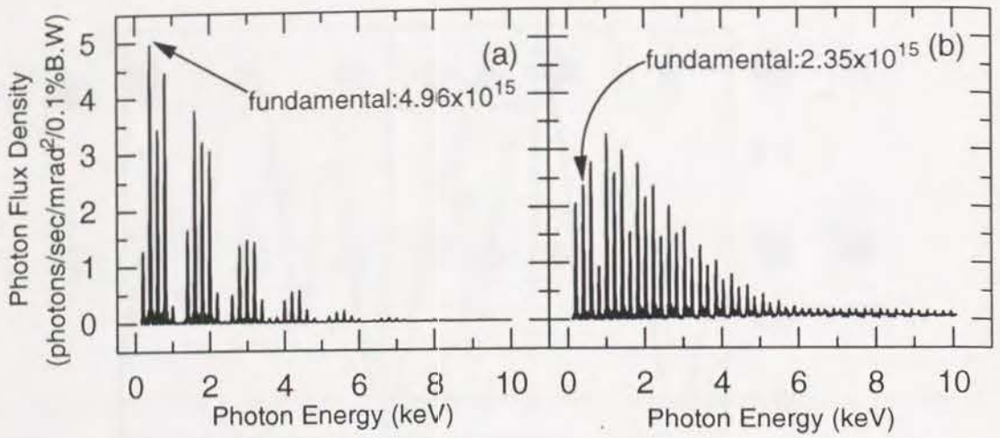

Figure 5.11. Spectra obtained from the (a)ordinary figure-8 undulator and (b)magnetic configuration shown in Fig. 5.9.

5.7.2 Focusing

If the first and the second field integrals are corrected and can be ignored, another effect, or the focusing of the beam, becomes remarkable. The focusing effect is characteristic of the ordinary ID and is utilized for focusing of the beam in some FEL experiments [38]-[40], but in the case of the ID to be installed in the storage ring, such effect causes some unwanted variations of storage-ring parameters. Therefore, it is important to investigate such focusing effects of IDs.

Focusing in the ID is characterized by the focal length given by [13],[41]

$$\frac{1}{F_x} = \frac{\partial^2 \phi}{\partial x^2}, \tag{5.8}$$

$$\frac{1}{F_y} = \frac{\partial^2 \phi}{\partial y^2}, \tag{5.9}$$

$$\frac{1}{F_c} = \frac{\partial^2 \phi}{\partial x \partial y}, \tag{5.10}$$

$$\phi = -\frac{1}{2}\left(\frac{e}{\gamma mc}\right)^2$$

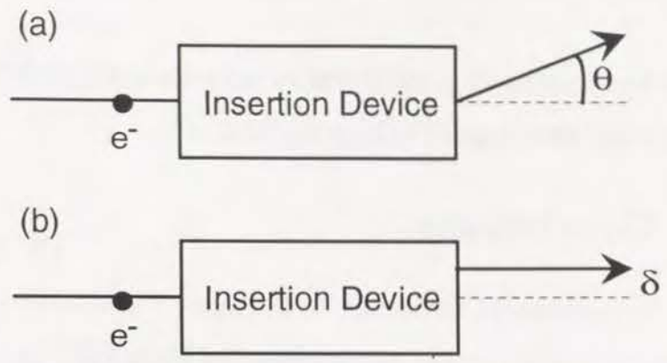

Figure 5.12. Effects of the ID field on the electron beam in the storage ring: (a)deflection and (b)displacement.

$$\times \int_{-\infty}^{\infty} \left[\left(\int_{-\infty}^{z} B_x(z')dz' \right)^2 + \left(\int_{-\infty}^{z} B_y(z')dz' \right)^2 \right] dz, \tag{5.11}$$

where the subscript c means the cross (skew) focusing. The focusing induces a variation of the betatron function and degrades the stability region in the tune diagram, or causes the tune shift [42]. In addition, the skew focusing causes a variation of the emittance, which results in the modification of the coupling constant.

For example, we consider the design A. By numerical computation, F_x, F_y and F_c are found to be 3.02×10^3, 5.00×10^2 and ∞. Therefore, the skew focusing does not exist. The horizontal and vertical focusings cause the tune shift and the variation of the betatron function given by [42]

$$\delta\nu_{x,y} = \frac{1}{4\pi}\frac{\beta_{x,y}}{F_{x,y}}, \tag{5.12}$$

$$\frac{\delta\beta_{x,y}}{\beta_{x,y}} = \frac{2\pi\delta\nu_{x,y}}{\sin 2\pi\nu_{x,y}}. \tag{5.13}$$

Substituting $\beta_x = 24$ m and $\beta_y = 9$ m, $\delta\nu_x$ and $\delta\nu_y$ are found to be 6.32×10^{-4} and 1.43×10^{-3}, respectively. These values are quite low and the degradation of the stability region in the tune diagram is almost negligible. $\delta\beta_x/\beta_x$ and $\delta\beta_y/\beta_y$ are found to be 7.94×10^{-3} and 1.80×10^{-2}, respectively. These variations in the

betatron functions result in the change of the angular divergence and the beam size. However, they are too small to be concerned.

5.8 Conclusions

We have discussed the design of the figure-8 undulator such as the magnet configuration and the size of the magnets, for obtaining VUV and SX with linear polarization at the SPring-8. It was found that the configuration containing four magnet arrays for the horizontal field and two for vertical, was fitted for the figure-8 undulator. The width of the horizontal undulator (L_W) and the period length (λ_u) were also determined considering the performances such as the brilliance and the on-axis power density. It was found that λ_u between 10 cm and 12 cm and L_W between 60 mm and 70 mm were preferable. In addition, the effects on the electron beam were also investigated, and it was found that the effects were small and negligible.

Chapter 6

Rhombus Undulator

6.1 Introduction

In chapter 2, it was found that the contribution of higher harmonics to the spectrum was small in the case of the elliptical undulator. In particular, no higher harmonics were observed in the special case that $K_x = K_y$ (helical undulator). Accordingly, the helical undulator has a great advantage that the ideal utilization of the fundamental radiation is possible without being annoyed by the heat load caused by the unwanted higher harmonics.

In an SR facility using medium-energy electrons, it is difficult to obtain VUV and SX by the fundamental radiation of the conventional undulators. In the case of the planar undulator, VUV and SX can be covered by using higher harmonics. On the other hand, higher harmonics cannot be obtained by helical undulators, therefore circularly-polarized VUV and SX is never available only by using helical undulators.

Other than the helical undulator, the elliptical and crossed undulators can be used to obtain higher harmonics with a circular polarization. In the case of the crossed undulator, the degree of polarization is quite sensitive to the angular divergence of the electron beam and it is almost impossible to use higher harmonics as circularly polarized radiation. In the case of the elliptical undulator, higher harmonics are considerably suppressed when one obtains the high degree of circular polarization and vice versa. Therefore, the ID which can generate higher harmonics

with the high degree of circular polarization is desired.

The reason why only the fundamental radiation is contained in the on-axis spectrum obtained from the helical undulator is that the deflection angle is constant, as already discussed. In the figure-8-undulator case, the deflection angle never becomes equal to zero. Therefore, the electric field never forms a pulse and higher harmonics are effectively suppressed. On the contrary, considerable higher harmonics are expected from a trajectory having a part in which the deflection angle is equal to zero. This is the basic idea of a novel ID to be proposed in this chapter. It is called a rhombus undulator, because the orbit projected on the transverse plane looks like a rhombus.

6.2 IDs for high-energy photons with a circular polarization

So far, various devices have been proposed to obtain high-energy photons with a circular polarization. In this section, the outlines of these devices are described.

6.2.1 Crossed undulator

The crossed undulator, which was already described in section 3.2.1, contains two planar undulators. Circularly-polarized radiation is obtained as a result of the coherent sum of SR from each undulator. In the case of such devices, the degree of polarization is sensitive to the finite angular divergence. Therefore, the achievable degree of polarization will be low.

6.2.2 Elliptical undulator

In the case of the elliptical undulator, the deflection angle never becomes equal to zero, however, it is not constant. Therefore, the apparent motion of the electron moving in the elliptical undulator is not a harmonic oscillation, which means that higher harmonics in addition to the fundamental appear in the spectrum. However,

it is easily understood that the degree of polarization will be lower with decreasing of the ratio, K_x/K_y, and the intensity of higher harmonics will be lower if K_x/K_y is close to unity.

6.2.3 Asymmetric and elliptical wigglers

It is well known that the polarization of radiation from a bending magnet is linear when observed on the orbital plane, while it is right-/left-handed circular when observed slightly above/below that plane, if the rotation of the electron is right handed. There are two kinds of ID applying this principle.

One is an asymmetric wiggler [44]. In the case of the ordinary wiggler, radiation from each pole is circularly polarized when observed off axis but the component of the circular polarization is cancelled out because the direction of the rotation of the electron passing through a certain pole is contrary to that of the electron passing through the neighboring pole. In the asymmetric wiggler, the field integrals of the neighboring poles are the same but the peak-field strengths are different from each other. Therefore, cancellation of polarization is avoided and the circular polarization is obtained when observed off axis.

The other is an elliptical wiggler [45]~[47]. Although the structure of this device is equivalent to that of the elliptical undulator, the vertical K value is much larger than unity. In an ordinary case, K_x and K_y are set to be ~10 and ~1, respectively. Then, the radiation from the device can be regarded as the superposition of the off-plane radiation from the bending magnets. Each half of the sinusoidal orbit is tilted up or down slightly by the horizontal magnetic field. When observed on axis, the cancellation of polarization is avoided and the circular polarization is obtained.

6.2.4 Comparison between each device

Let us consider an SR facility using an electron beam with a medium energy, for example, 1 GeV. In this case, the energy range which can be covered by the fundamental radiation from a conventional undulator will be up to 300 eV. If the

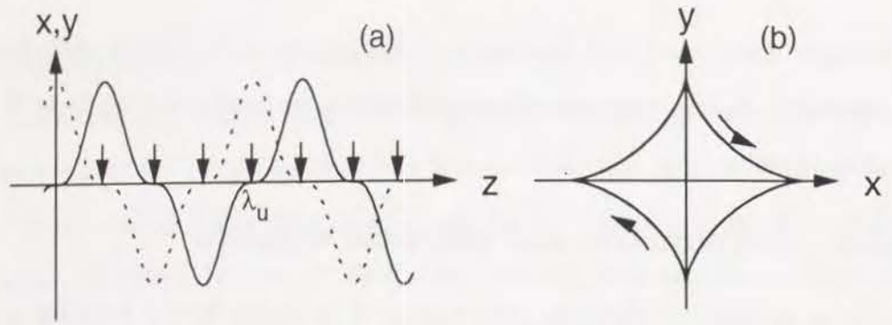

Figure 6.1. Trajectory in the proposed ID.

user wants circularly-polarized photons in the x-ray region (above 2 keV), no device exists except the wiggler type such as the elliptical wiggler. On the other hand, an undulator-type device, such as the elliptical undulator, can be used if the user wants circularly-polarized VUV and SX (below 1 keV). However, the intensity of higher harmonics obtained from the elliptical undulator is not so high as described in chapter 2. In the case of the crossed undulator, the intensity of higher harmonics is equivalent to that of the planar undulator, however, the achievable degree of polarization is sensitive to the angular divergence of the electron beam.

6.3 Principle of a rhombus undulator

As described in the previous section, circularly-polarized photons with energies slightly higher than the upper limit of the fundamental radiation can be obtained by using the elliptical undulator or the crossed undulator. However, the intensity and/or the degree of polarization may not be sufficiently high. A device to be proposed from now on is an ID improving these disadvantages.

6.3.1 Trajectory

Let us consider a trajectory shown in Figs. 6.1 (a) and (b). In this case, the deflection angle becomes equal to zero at the points indicated by the arrows in the figure, where the contribution to the radiation becomes the largest. Therefore,

the electric field of radiation is distorted and higher harmonics are observed in the spectrum. In addition, the relative phase between the horizontal and vertical motions is $\pi/2$, therefore the polarization becomes circular. As shown in Fig. 6.1 (b), the orbit projected on the transverse plane looks like a rhombus. Therefore, we call this device a "rhombus" undulator.

The orbits shown in Fig. 6.1 are expressed as

$$\begin{aligned} x &= \sin z - \frac{\sin 3z}{3}, \\ y &= \cos z + \frac{\cos 3z}{3}. \end{aligned} \tag{6.1}$$

In order to make an electron move along the trajectory given by equation (6.1), the magnetic fields should be

$$\boldsymbol{B} = \boldsymbol{B}_0 + \boldsymbol{B}_1, \tag{6.2}$$

$$\boldsymbol{B}_0 = B_0 \left[\cos\left(\frac{2\pi}{\lambda_u} z\right), \ -\sin\left(\frac{2\pi}{\lambda_u} z\right), \ 0 \right], \tag{6.3}$$

$$\boldsymbol{B}_1 = B_1 \left[\cos\left(\frac{6\pi}{\lambda_u} z\right), \ \sin\left(\frac{6\pi}{\lambda_u} z\right), \ 0 \right], \tag{6.4}$$

$$B_1 = 3B_0. \tag{6.5}$$

From above equations, it is found that $\boldsymbol{B}_0$ represents the magnetic field of a helical undulator having the period length of λ_u, while $\boldsymbol{B}_1$ represents that having the period length of $\lambda_u/3$. Therefore, the magnetic field $\boldsymbol{B}$ is realized by superposing two helical undulators, one of which has the period length three times as long as that of the other. In addition, the direction of rotation should be different. For example, $\boldsymbol{B}_0$ is right handed, while $\boldsymbol{B}_1$ is left handed.

6.3.2 Configuration of magnets

Two methods are considered in order to superpose undulators having different period lengths. One is the superposition of magnetization of each magnet. This means that the direction of magnetization should have some angles with respect to

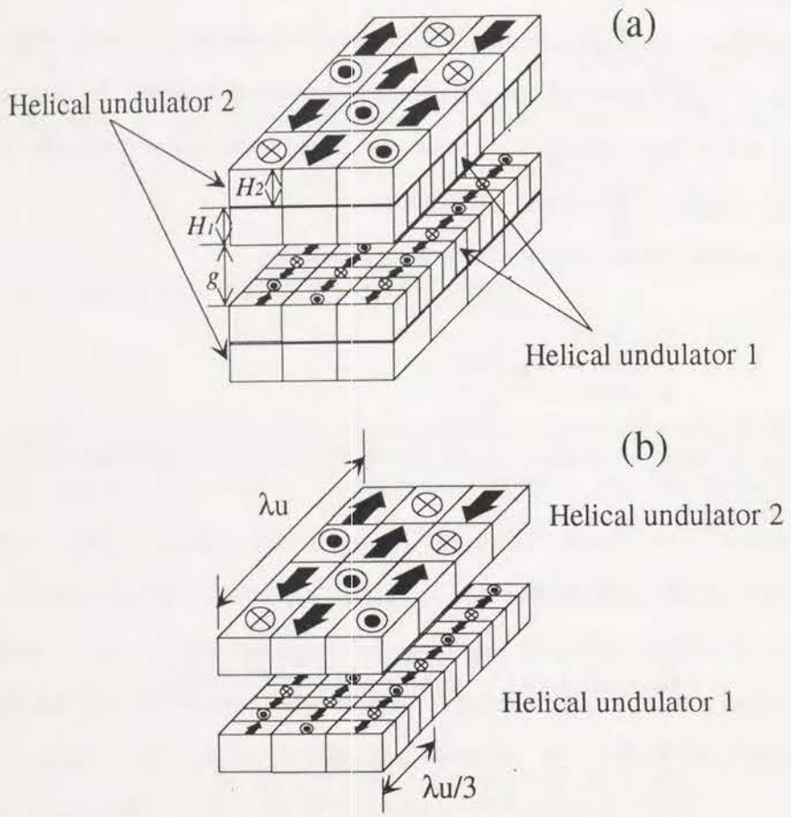

Figure 6.2. Superposition of two helical undulators having different period lengths.

the x, y or z axis. Therefore, the construction of the device will be difficult. The other is the superposition of the magnet blocks of each device, as shown in Figs. 6.2 (a) and (b). In the case of configuration (a), the peak magnetic fields are considered to have the dependence on the gap as follows

$$B_0 \simeq C_0 \, \mathrm{e}^{-\pi(g+2H_1)/\lambda_u}, \tag{6.6}$$

$$B_1 \simeq C_1 \, \mathrm{e}^{-\pi g/(\lambda_u/3)}, \tag{6.7}$$

where C_0 and C_1 are the geometrical factors determined by the size of the magnet block. It is found from the above equations that the relation (6.5) does not hold for all the values of the gap. In the case of configuration (b), the relation (6.5) can be made hold for all the values of the gap by moving the helical undulators 1 and 2 independently. In addition, this device can be used as a simple helical undulator having the period length of λ_u or $\lambda_u/3$. The disadvantage of configuration (b) is that the peak magnetic field may be lower. However, (b) is preferable to (a) on the point described above and that the mechanical support may be easier.

6.4 Spectrum

Very generally, the magnetic fields generated by the configuration of magnets shown in Fig. 6.2 are given by

$$\begin{aligned} B_x(z) &= B_{x1}\cos 3k_u z + B_{x2}\cos k_u z, \\ B_y(z) &= B_{y1}\sin 3k_u z - B_{y2}\sin k_u z, \end{aligned} \tag{6.8}$$

where $k_u = 2\pi/\lambda_u$. Solving the equations of motion, we have

$$\begin{aligned} \boldsymbol{\beta}(t) = \Bigg[& (-K_{y1}\cos 3\omega_0 t + K_{y2}\cos\omega_0 t), \ -(K_{x1}\sin 3\omega_0 t + K_{x2}\sin\omega_0 t), \\ & \left(1 - \frac{K_{x1}^2 + K_{x2}^2 + K_{y1}^2 + K_{y2}^2}{4\gamma^2}\right)\gamma \\ & + \frac{A}{4\gamma}\cos 6\omega_0 t + \frac{B}{2\gamma}\cos 4\omega_0 t + \frac{C}{4\gamma}\cos 2\omega_0 t\Bigg]\frac{\beta}{\gamma}, \end{aligned} \tag{6.9}$$

$$\begin{aligned} \boldsymbol{r}(t) = \Bigg[& \left(-\frac{K_{y1}}{3}\sin 3\omega_0 t + K_{y2}\sin\omega_0 t\right), \ -\left(\frac{K_{x1}}{3}\cos 3\omega_0 t + K_{x2}\cos\omega_0 t\right), \\ & \left(1 - \frac{K_{x1}^2 + K_{x2}^2 + K_{y1}^2 + K_{y2}^2}{4\gamma^2}\right)\gamma\omega_0 t \\ & + \frac{A}{24\gamma}\sin 6\omega_0 t + \frac{B}{8\gamma}\sin 4\omega_0 t + \frac{C}{8\gamma}\sin 2\omega_0 t\Bigg]\frac{c\beta}{\omega_0\gamma}, \end{aligned} \tag{6.10}$$

with

$$K_{x1,y1} = \frac{eB_{x1,y1}\lambda_u/3}{2\pi mc}, \tag{6.11}$$

$$K_{x2,y2} = \frac{eB_{x2,y2}\lambda_u}{2\pi mc}, \tag{6.12}$$

$$\omega_0 = \frac{2\pi c}{\lambda_u}\left(1 - \frac{K_{x1}^2 + K_{x2}^2 + K_{y1}^2 + K_{y2}^2}{4\gamma^2}\right), \tag{6.13}$$

$$A = K_{x1}^2 - K_{y1}^2, \tag{6.14}$$

$$B = K_{x1}K_{x2} + K_{y1}K_{y2}, \tag{6.15}$$

$$C = 2K_{x1}K_{x2} - 2K_{y1}K_{y2} - K_{x2}^2 + K_{y2}^2. \tag{6.16}$$

The photon flux density for the k-th harmonic is calculated directly as

$$\frac{d^2P}{d\Omega d\omega} = \frac{e^2\gamma^2N^2}{\pi\epsilon_0 c}(|f_x|^2 + |f_y|^2), \tag{6.17}$$

with

$$f_x = (S_z\gamma\theta\cos\phi - S_x)P_N, \tag{6.18}$$

$$f_y = (S_z\gamma\theta\sin\phi - S_y)P_N, \tag{6.19}$$

$$S_x = \frac{1}{2\pi}\int_0^{2\pi}(-k_{y1}\cos 3\eta + K_{y2}\cos\eta)\,\mathrm{e}^{-i\psi(\eta)}d\eta, \tag{6.20}$$

$$S_y = -\frac{1}{2\pi}\int_0^{2\pi}(k_{x1}\sin 3\eta + K_{x2}\sin\eta)\,\mathrm{e}^{-i\psi(\eta)}d\eta, \tag{6.21}$$

$$S_z = \frac{1}{2\pi}\int_0^{2\pi}\mathrm{e}^{-i\psi(\eta)}d\eta, \tag{6.22}$$

$$\begin{aligned}\psi(\eta) &= k\eta - \frac{A\xi}{12}\sin 6\eta - \frac{B\xi}{4}\sin 4\eta - \frac{C\xi}{4}\sin 2\eta \\ &- 2\xi\gamma\theta\left[\sin\phi\left(\frac{K_{x1}}{3}\cos 3\eta + K_{x2}\cos\eta\right)\right. \\ &- \left.\cos\phi\left(\frac{K_{y1}}{3}\sin 3\eta - K_{y2}\sin\eta\right)\right].\end{aligned} \tag{6.23}$$

The degree of circular polarization is given by

$$P_C = \frac{2\mathrm{Im}(f_x^* f_y)}{|f_x|^2 + |f_y|^2}. \tag{6.24}$$

If the relation (6.5) holds, the K values are the same. Replacing those by K, equations (6.20) and (6.21), for photons observed on axis, are rewritten as

$$S_x = \begin{cases} 0; & k = \text{even}, \\ Q; & k = 1 + 4n, \\ -Q; & k = 3 + 4n, \end{cases} \tag{6.25}$$

$$S_y = \begin{cases} 0; & k = \text{even}, \\ -iQ; & k = \text{odd}, \end{cases} \tag{6.26}$$

with

$$Q = \frac{2K}{\pi}\int_0^{\pi/2}(\sin 3\eta + \sin\eta)\sin\left(k\eta - \frac{\xi K^2}{2}\sin 4\eta\right)d\eta, \tag{6.27}$$

where n is an integer. From above equations, it is found that P_C is equal to -1 for $(4n+1)$-th harmonics and 1 for $(4n+3)$-th. In other words, the radiation has a right-handed circular polarization for $(4n+1)$-th harmonics and has a left-handed for $(4n+3)$-th, which means that this device cannot be used as a wiggler because the obtainable degree of polarization will be low in the energy region of higher harmonics, or the envelope part of the spectrum. The reason why radiation with different helicities are contained is that the magnetic field, or the trajectory in the device, contains two helicities.

6.5 Power density

Substituting (6.9) into (2.47), we obtain the power density from the rhombus undulator

$$\frac{dP}{d\Omega} = \frac{\gamma^4\omega_0 e^2 N}{2\pi^2\epsilon_0 c}\int_{-\pi}^{\pi}\left(\frac{E_1}{D^3} - \frac{E_2}{D^5}\right)d\eta, \tag{6.28}$$

with

$$E_1 = U^2 + V^2, \tag{6.29}$$

$$E_2 = 4(XU + YV)^2, \tag{6.30}$$

$$D = 1 + X^2 + Y^2, \tag{6.31}$$

$$X = \gamma\theta_x - (K_{y1}\cos 3\eta - K_{y2}\cos\eta), \tag{6.32}$$

$$Y = \gamma\theta_y - (K_{x1}\sin 3\eta + K_{x2}\sin\eta), \tag{6.33}$$

$$U = -3K_{y1}\sin 3\eta + K_{y2}\sin\eta, \tag{6.34}$$

$$V = 3K_{x1}\cos 3\eta + K_{x2}\cos\eta. \tag{6.35}$$

6.6 Examples of performances

Now, let us show some performances of the rhombus undulator. In order to obtain sufficient tunability of the undulator, at least 1.0 is required as the maximum K value. In the case of the magnetic configuration shown in Fig. 6.2(b), λ_u larger than 18 cm is necessary for this requirement when the minimum gap is assumed to be 20 mm. In this case, the helical undulator 1 has the period length of 6 cm. Therefore, this device can be operated in three modes: (a)helical undulator 1 (period=6 cm), (b)helical undulator 2 (period=18 cm), and (c)rhombus undulator. For example, the electron energy is assumed to be 1 GeV, the average current 100 mA, coupling constant 0.1, horizontal and vertical betatron values 10 m and the total length of an ID 4.5 m.

6.6.1 Spectrum

Figures 6.3(a)~(d) show examples of spectra obtained from the helical, elliptical, crossed and rhombus undulators, respectively. The K values for each device are set to the values indicated in the figure so that the energy of the 7th (helical, elliptical and crossed undulators) and the 27th (rhombus undulator) harmonic becomes equal to 500 eV. The natural emittance is assumed to be 10 nm·rad, which is a typical value in most SR facilities now planned or under construction.

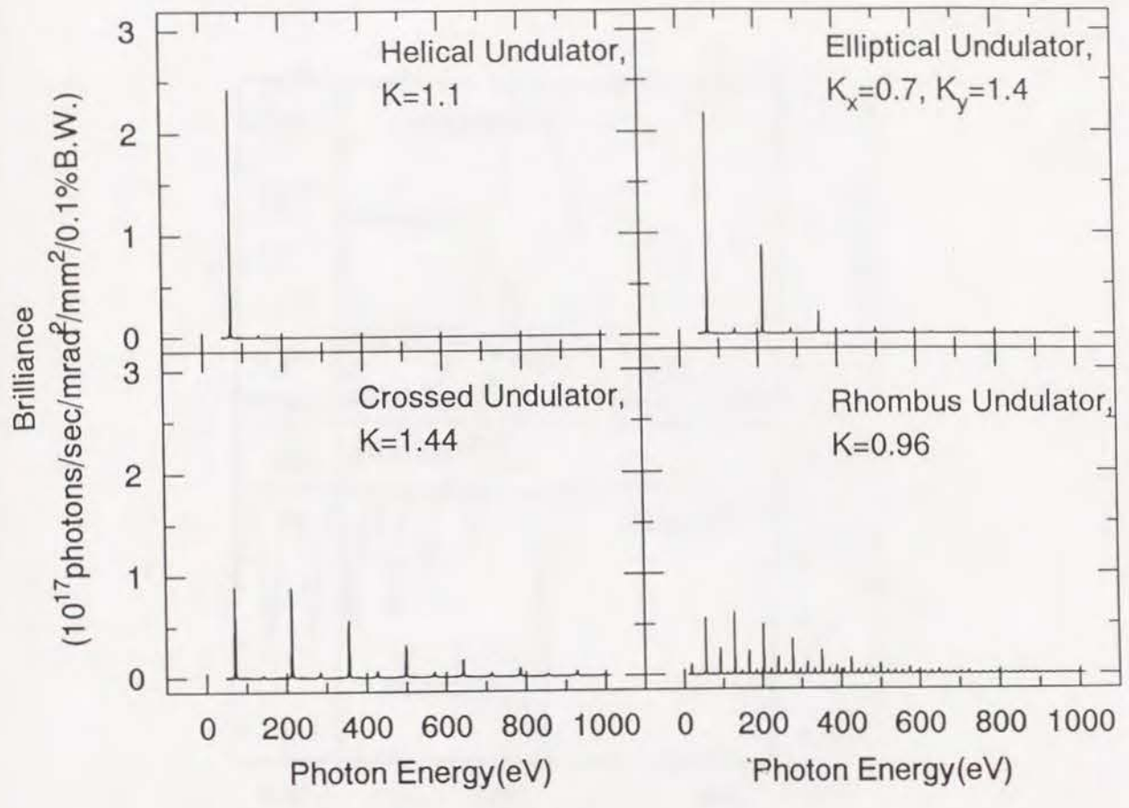

Figure 6.3. Examples of spectra obtained from the (a)helical, (b)elliptical, (c)crossed and (d)rhombus undulators.

It is found from the figure that the helical undulator is the best choice for users who want to use low-energy photons, because only the fundamental radiation appears in the spectrum. On the other hand, for those who want to use high-energy photons, for example, above 200 eV, other IDs should be used.

Figures 6.4(a) and (b) show the spectra and the degree of circular polarization in the energy range between 495 eV and 505 eV obtained from the elliptical, crossed and rhombus undulators, respectively. If users are not concerned with the degree of polarization, the best choice will be the crossed undulator because the brilliance is the highest. On the other hand, the best choice will be the rhombus undulator if users need the high degree of polarization.

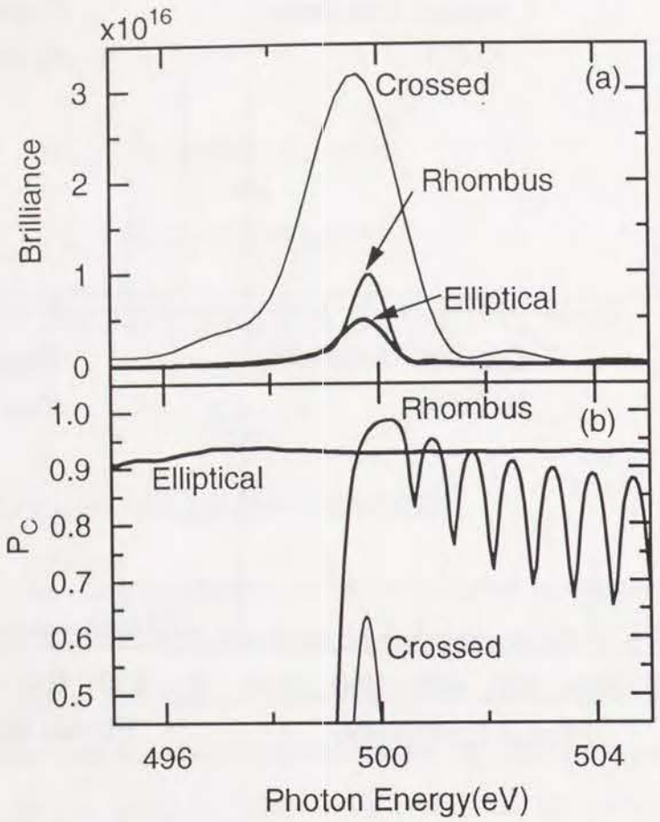

Figure 6.4. Examples of (a)spectra and (b)degree of circular polarization obtained from the crossed, elliptical and rhombus undulators.

6.6.2 Emittance dependence

Figures 6.5(a) and (b) show the spectra and the degree of circular polarization obtained from the rhombus undulator for various values of natural emittance. The peak brilliance degrades with increasing of the emittance. However, P_C remains meaningful ($P_C \sim 0.7$) even when $\varepsilon = 1000$ nm·rad.

In Figs. 6.6 (a) and (b), the spectra and the degree of polarization for various ε are shown in the case of the crossed undulator. It is found from the figure that the degradation of P_C due to the finite emittance is more remarkable. For example, P_C=0.36 and 0.28 when $\varepsilon = 100$ and 1000 nm·rad. These values are considered to

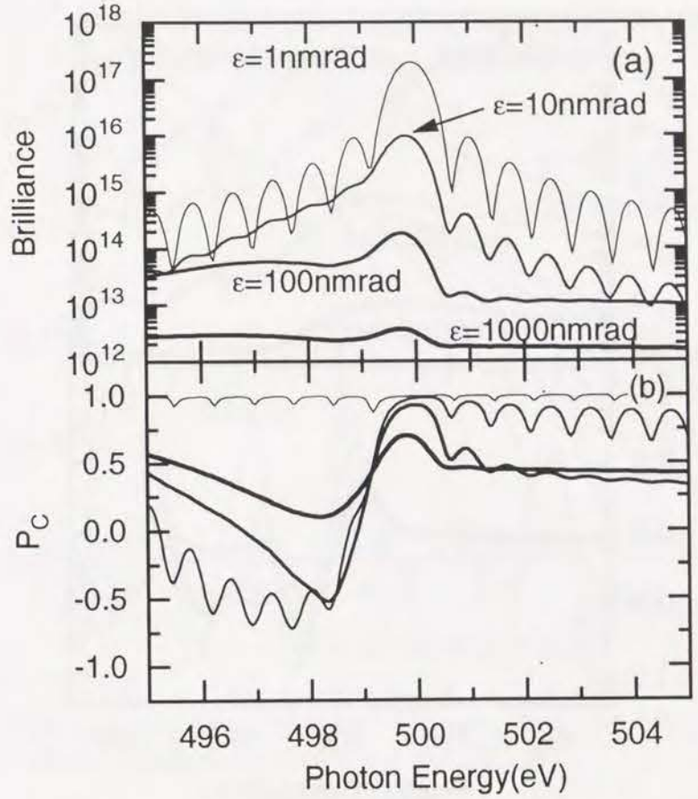

Figure 6.5. Emittance dependence of the (a)brilliance and (b)degree of polarization obtained from the rhombus undulator.

be meaningless for users of the circular polarization.

6.6.3 Available energy range

Figure 6.7 shows the peak brilliance for four IDs. The natural emittance is assumed to be 10 nm·rad. The solid lines labeled "Helical 1" and "Helical 2" show the peak brilliance in the case that either the helical undulator 1 or 2 are used. In this case, this device works as a simple helical undulator. Other solid lines show the peak brilliances of $(4n + 3)$-th higher harmonics obtained from the rhombus undulator. The dashed line shows an example of the spectrum obtained from the elliptical multipole wiggler (EMPW). The period length is assumed to be 12 cm, K_x

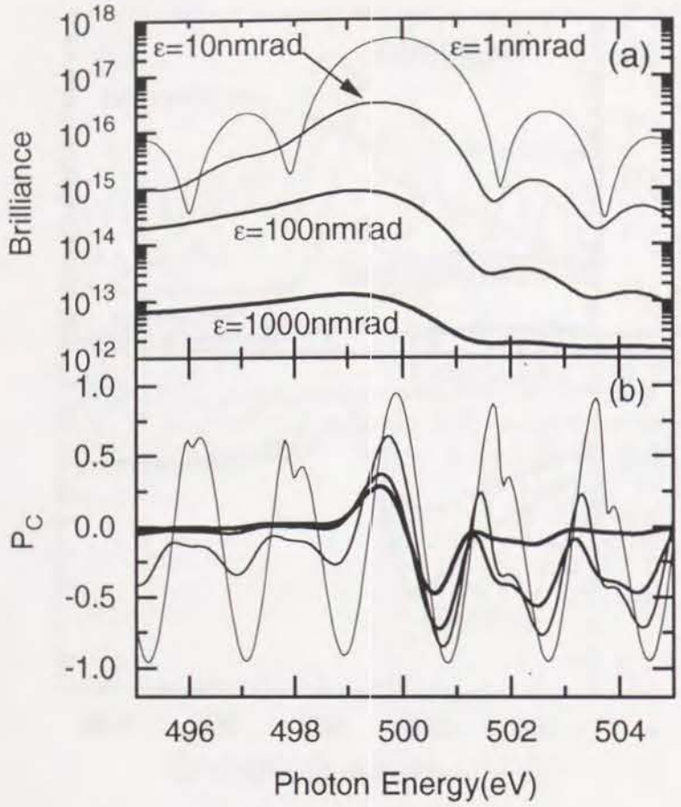

Figure 6.6. Emittance dependence of the (a)brilliance and (b)degree of polarization obtained from the crossed undulator.

1.0 and K_y 11.2. The brilliance obtained from the rhombus undulator is found to be higher than that of the EMPW in the energy range shown in the figure. We can say from the figure that quite broad energy range is covered by using the proposed device, as shown in Table 6.1.

6.6.4 Power density

Figures 6.8 (a) and (b) show the spatial distributions of the power density obtained from the rhombus and elliptical undulators, respectively. The parameters are correspondent to those in Figs. 6.3 and 6.4. It is found from the figures that the on-axis power density from the rhombus undulator is higher than that of the

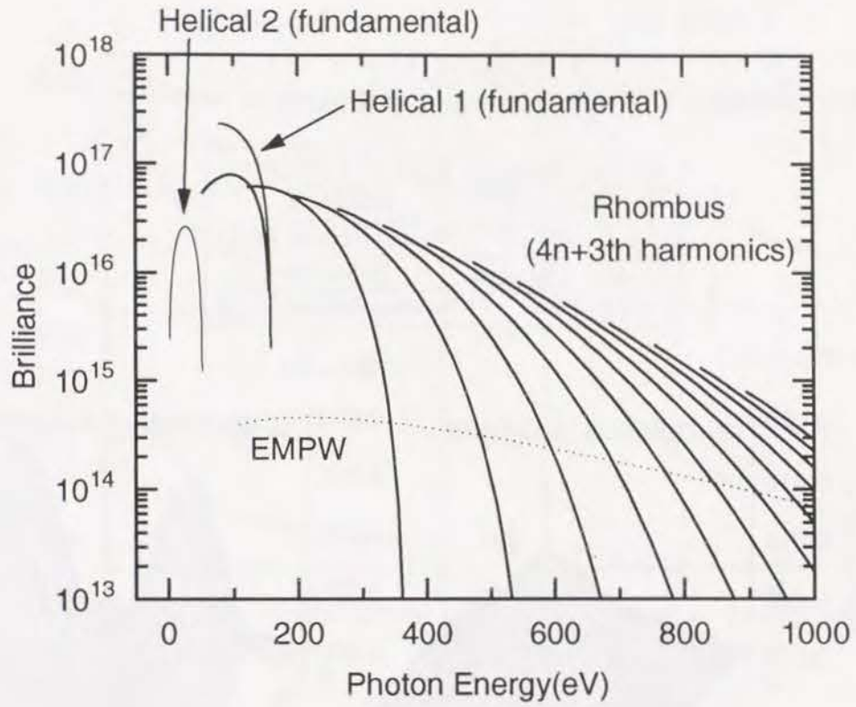

Figure 6.7. Examples of peak brilliances obtained from the helical undulator 1, helical undulator 2, rhombus undulator and the EMPW.

elliptical undulator. This is natural because the contribution of higher harmonics to the spectrum is larger than that of the elliptical undulator. As for the peak width, that of the rhombus undulator is larger than that of the elliptical undulator, which is due to the larger deflection angle of the trajectory. Anyway, the on-axis power density is too low to damage the optical elements.

6.7 Consideration on the design of the rhombus undulator

Because the magnet configuration shown in Fig. 6.2 (b) is simply the superposition of two helical undulators having period lengths of λ_u and $\lambda_u/3$, the aim in designing a rhombus undulator is the same as that of the helical undulator. What is required of the helical undulator is that the horizontal and vertical K values are

Table 6.1. Available energy and the type of undulator.

Energy Range	Type of Undulator
2 eV∼50 eV	Helical 2
50 eV∼80 eV	Novel (Helical 1+2)
80 eV∼150 eV	Helical 1
150 eV∼	Novel (Helical 1+2)

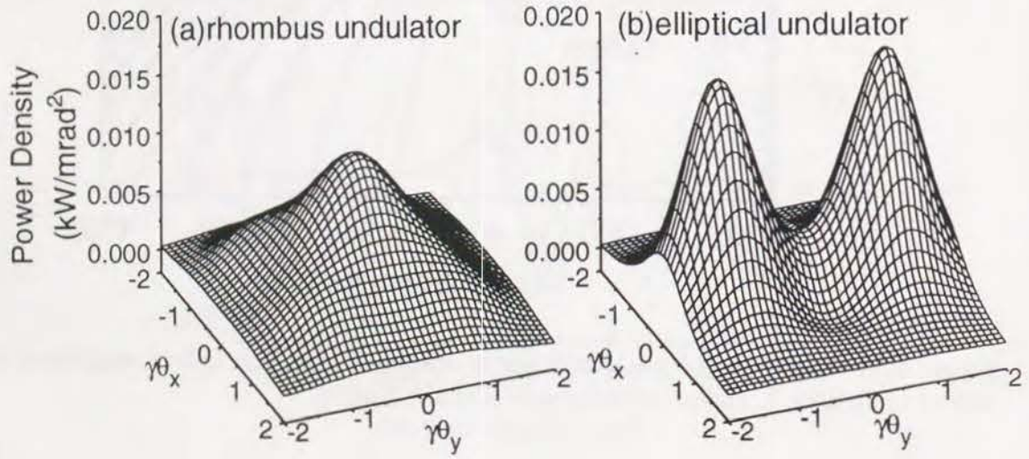

Figure 6.8. Spatial distribution of the power density obtained from the (a) rhombus and (b) elliptical undulators.

the same at all the values of the gap. It is not so difficult to realize this requirement. For example, let the total width of an ID be 120 mm, the height 40 mm and λ_u 18 cm. Figures 6.9 (a) and (b) show the peak magnetic fields for various values of L_W in the case of the helical undulators 1 and 2, respectively. It is found from the figures that L_W = 18 mm and 30 mm are preferable for the helical undulators 1 and 2, respectively.

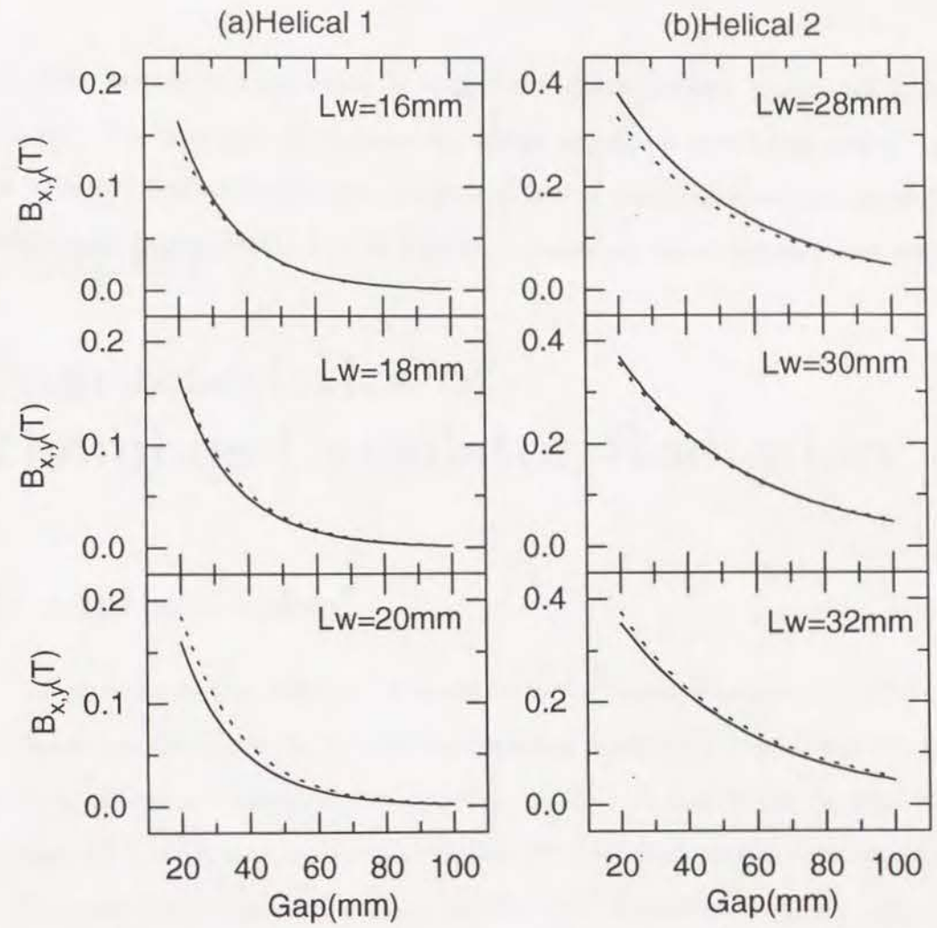

Figure 6.9. Peak magnetic fields as a function of the value of the gap for various values of L_W: (a) helical undulator 1 and (b) helical undulator 2.

6.8 Conclusions

In this chapter, the "rhombus" undulator was proposed as an ID for obtaining higher harmonics with a circular polarization. In addition, comparisons with the elliptical and crossed undulators were made with respect to the photon flux density and the degree of polarization. It was found that the photon flux density obtained from the rhombus undulator was about twice larger than that of the elliptical undulator and that the degree of polarization was almost equal to unity, when the angular divergence was as small as is achievable in most SR facilities. Even if the

angular divergence was not small, the degree of polarization remained sufficiently large. It was also found that by using the proposed device not only as the rhombus undulator but also as a simple helical undulator, circularly-polarized radiation with a quite broad energy range, for example, from 2 eV to 1000 eV, would be available.

Chapter 7

Characteristics of Rhombus-Undulator Radiation

7.1 Introduction

When utilizing the radiation obtained from the rhombus undulator, two factors are important for the users. One is the degree of polarization and the other is the intensity of higher harmonics. Because the rhombus undulator will be used in the medium SR facility, it is unnecessary to take the heat load problem into account.

There are four types of K value in the rhombus undulator, i. e., K_{x1}, K_{y1}, K_{x2} and K_{y2}. The subscripts 1 and 2 represent the magnetic fields generated by helical undulators 1 and 2, respectively. The subscripts x and y represent the horizontal and vertical fields, respectively. With respect to obtaining the high degree of polarization, it is preferable that the ratio, K_x/K_y, is set to unity. As already described, it is not so difficult to hold K_x/K_y to be unity at all values of the magnet gap. Another K ratio, K_1/K_2, can be changed easily by moving the magnet arrays of helical undulators 1 and 2 independently. Therefore, it is meaningful to investigate the dependence of radiation on the ratio of K_1/K_2.

Because many higher harmonics are contained in the rhombus-undulator radiation, it is important to determine which harmonic should be used for the experiments. In order to do so, it is necessary to investigate the relation between harmonics and polarization including the effects of the emittance of the electron beam.

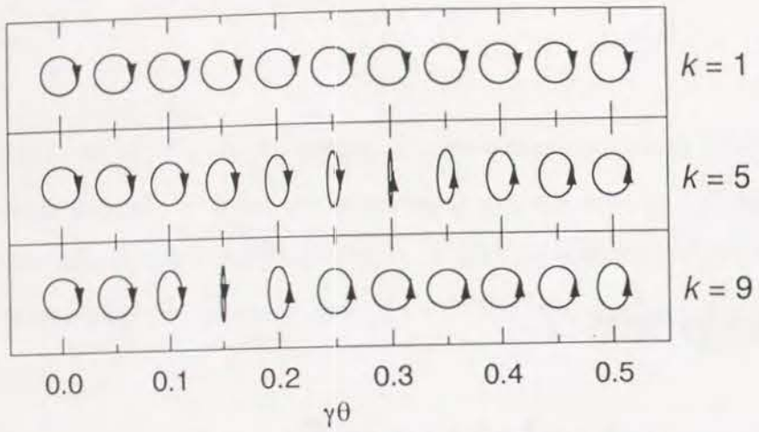

(a) $k = (4n+1)$th harmonics

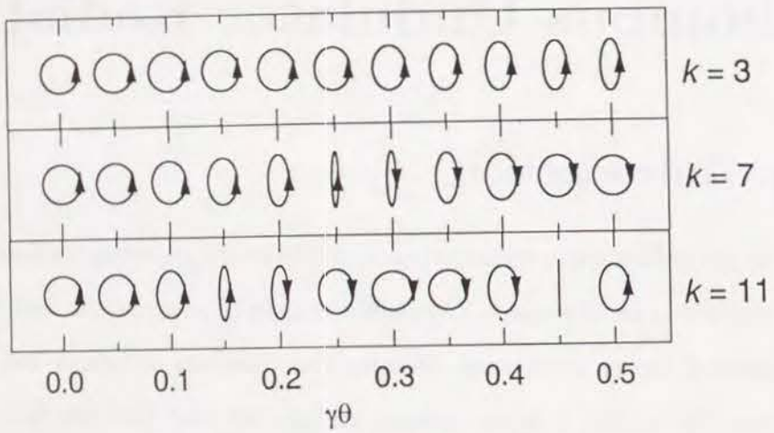

(b) $k = (4n+3)$th harmonics

Figure 7.1. Shapes of polarization for various harmonics obtained from the rhombus undulator.

In this chapter, some characteristics of rhombus-undulator radiation mentioned above, are investigated. In addition, an explanation with respect to the relation between the helicity and harmonics is given by analyzing the electric field of radiation.

7.2 Polarization

Since the polarization of radiation obtained from the rhombus undulator has the strange characteristics that both left- and right-handed circular polarizations are contained, it is interesting to investigate the polarization in detail.

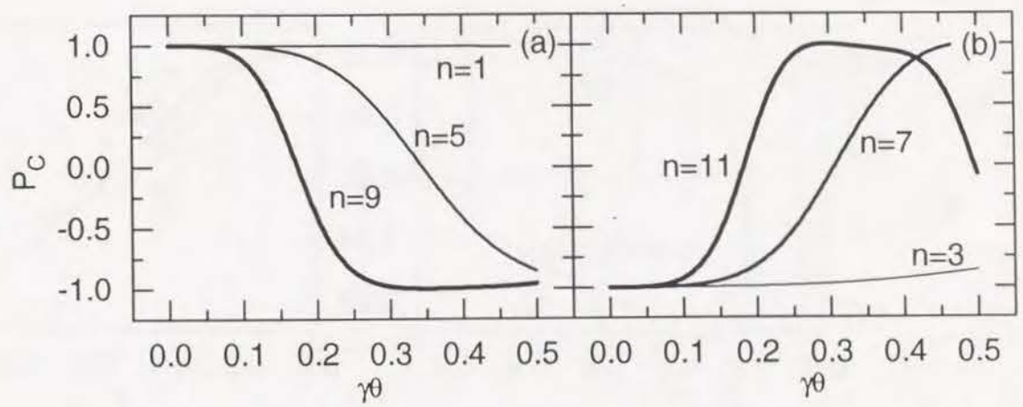

Figure 7.2. Angular distribution of the degree of polarization.

7.2.1 Angular distribution

Figures 7.1 (a) and (b) show the angular dependence of polarization for various harmonics. Each polarization is shown as an ellipse with an arrow representing the direction of rotation. As described before, the on-axis polarization for $(4n + 1)$-th harmonics is right handed, while that for $(4n + 3)$-th harmonics is left handed. For the fundamental, the shape of polarization is almost a circle at all angles shown in the figure. On the other hand, the shape of polarization for higher harmonics collapses rapidly as the increase of $\gamma\theta$. After collapsing, the shape begins to return to a circle, however, the direction of rotation is reversed.

Figures 7.2 (a) and (b) show the angular distribution of the degree of polarization, P_C, for harmonics corresponding to those in Figs. 7.1 (a) and (b), respectively. It is found from the figure that the degradation of P_C according to the increase of $\gamma\theta$ is more remarkable for higher harmonics. Therefore, P_C for higher harmonics are affected easily by the finite beam emittance and the size of the aperture.

7.2.2 Effects due to the angular divergence

Figure 7.3 shows the dependence of the degree of polarization on the angular

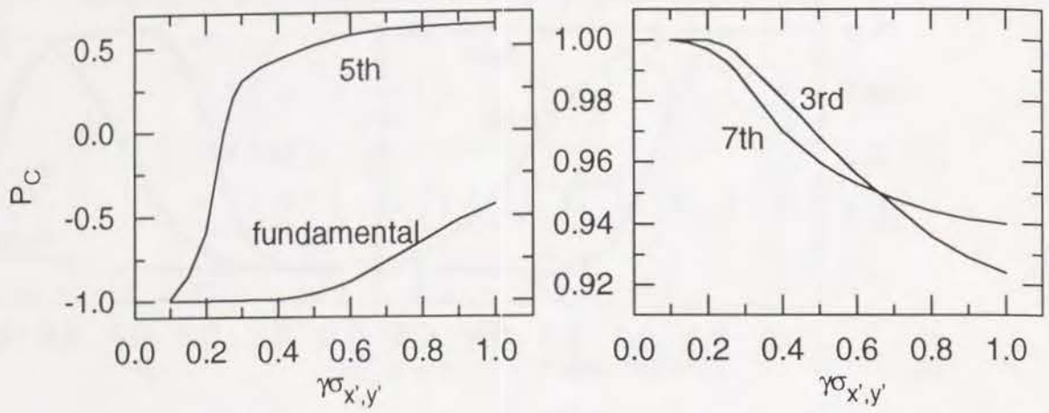

Figure 7.3. Dependence of P_C on the angular divergence.

divergence of the beam for various harmonics obtained from the rhombus undulator. The degradation of the degree of polarization is remarkable for $(4n+1)$-th harmonics. In particular, that of the 5th harmonic is reversed when $\gamma\sigma_{x',y'}$ are larger than 0.3. This is due to the contribution of the 7th harmonic which has a left-handed circular polarization. On the other hand, the degradation is small for $(4n+3)$-th harmonics. We can say from the figures that the $(4n+3)$-th harmonics are preferable for experiments which need the high degree of polarization.

7.3 Electric field of radiation

7.3.1 Time dependence

Figure 7.4 shows the on-axis electric fields and the deflection angle as a function of the observer time. Although the K values are not so high (0.96), the electric field forms a pulse at the point where the deflection angle is equal to zero. This is due to the fact that the maximum deflection angle is not equal to K/γ but equal to $2K/\gamma$, which results in the effective K value of 1.92. Because the electric field forms a pulse, so many higher harmonics will appear in the spectrum.

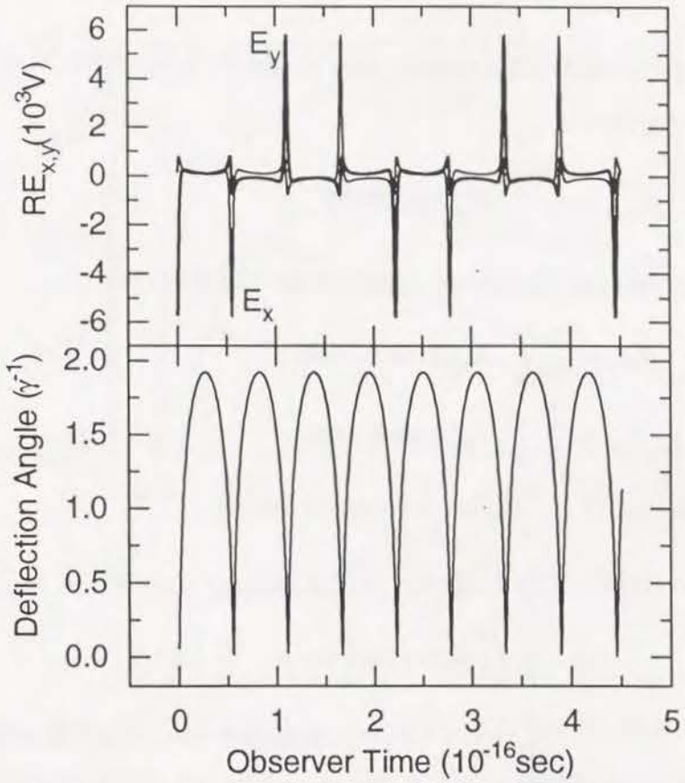

Figure 7.4. Electric field obtained from the rhombus undulator and the deflection angle.

7.3.2 Harmonics and polarization

As described before, the radiation from the rhombus undulator contains both left- and right-handed circular polarizations. This is natural because the trajectory contains both right- and left-handed helicities. However, this cannot explain the fact that the polarization is right handed for $(4\ddot{n}+1)$-th harmonics and left handed for $(4n+3)$-th harmonics. In order to understand the relation between harmonics and polarization, the analysis of the electric field is necessary.

It is clear from Fig. 7.4 that E_x and E_y associate with each other by the relation

$$E_y(t) = E_x(t + T/4), \tag{7.1}$$

where T is the period. The electric field of the k-th harmonic is obtained by the Fourier transformation

$$E_{kx,y} = \frac{1}{T}\int_0^T E_{x,y}(t)\, \mathrm{e}^{ik\omega_1 t} dt. \tag{7.2}$$

Due to the symmetry, the above equations are rewritten as

$$\begin{aligned} E_{kx} &= \frac{1}{T}\int_0^T E_x(t) \cos k\omega_1 t dt, \\ E_{ky} &= \frac{i}{T}\int_0^T E_y(t) \sin k\omega_1 t dt. \end{aligned} \tag{7.3}$$

From the relation (7.1), E_{ky} is rewritten as follows

$$\begin{aligned} E_{ky} &= \frac{i}{T}\int_0^T E_x\left(t+\frac{T}{4}\right) \sin k\omega_1 t dt \\ &= \frac{i}{T}\int_0^T E_x(\tau) \sin\left(k\omega_1\tau - \frac{k\pi}{2}\right) d\tau \\ &= \begin{cases} -\dfrac{i}{T}\displaystyle\int_0^T E_x(\tau)\cos k\omega_1\tau d\tau = -iE_{kx}; & k = 4n+1, \\ \dfrac{i}{T}\displaystyle\int_0^T E_x(\tau)\cos k\omega_1\tau d\tau = iE_{kx}; & k = 4n+3. \end{cases} \end{aligned} \tag{7.4}$$

Therefore, the polarization for $(4n+1)$-th harmonics is right handed and that for $(4n+3)$-th harmonics are left handed.

Because the discussion above is limited only by the conditions $E_x(t) = E_y(t + T/4)$ and $E_x(t) = E_x(t+T)$, it is quite general. We can say that the radiation whose amplitude of both horizontal and vertical electric fields are the same and the phase difference is $\pi/2$ necessarily contains both right- and left-handed circular polarizations.

7.4 K-ratio dependence

If the magnet configuration shown in Fig. 6.2 (b) is adopted, the K-ratio, which means the ratio of the K value of the helical undulator 1 to that of the helical undulator 2, can be varied arbitrarily. Therefore, it is important to investigate the K-ratio dependence of radiation to determine the values of the half gap of both

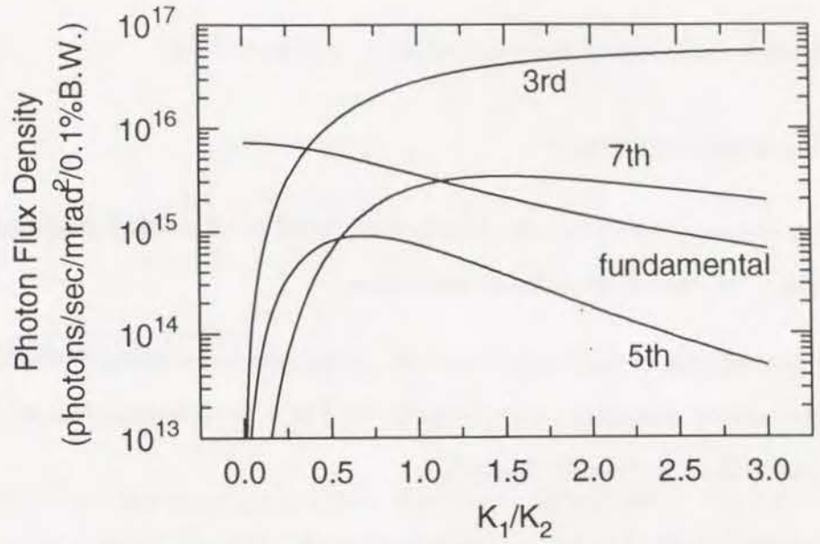

Figure 7.5. K-ratio dependence of the photon flux density.

helical undulators 1 and 2. As described in section 6.7, the K ratio, K_x/K_y, can be made hold almost unity for all the values of the available gap, therefore the dependence only on the K ratio, K_1/K_2, is important.

Figure 7.5 shows the dependence of the photon flux density for various harmonics on the K ratio, K_1/K_2. When $K_1/K_2 = 0$, the device is reduced to an ordinary helical undulator having the period length of λ_u. Therefore, the photon flux density for harmonics except the fundamental is equal to zero at $K_1/K_2 = 0$. As the increase of the K ratio, the photon flux density for harmonics other than the fundamental increases, while that for the fundamental degrades. As for the third harmonic, the increase is monotonous. This is natural because the increase of the K ratio means the increase of K_1, which is the K value of the helical undulator 1. When $K_1/K_2 = \infty$, the device is reduced to an ordinary helical undulator having the period length of $\lambda_u/3$. Therefore, harmonics except the third will vanish at $K_1/K_2 = \infty$. As for the fifth and seventh harmonics, the photon flux density has its maximum at $K_1/K_2 \sim 0.6$ and $K_1/K_2 \sim 1.5$, respectively. What is interesting is that each harmonic has its maximum not at $K_1/K_2 = 1$ but at $K_1/K_2 \neq 1$. This is quite

important when determining the value of the gap in operation.

7.5 Conclusions

In this chapter, various characteristics of rhombus-undulator radiation were investigated. The results are summarized below.

1. The degradation of the degree of circular polarization according to the increase of the angular divergence is remarkable for $(4n + 1)$-th harmonics, while that for $(4n + 3)$-th harmonics is small.

2. The electric field of radiation forms a pulse even if the K value is not so high. This is due to the fact that the maximum deflection angle is equal to $2K/\gamma$, not K/γ. As a result, higher harmonics appear in the spectrum effectively.

3. The photon flux density for the fundamental (the third harmonic) degrades (increases) monotonously as the K ratio. On the other hand, those for other harmonics have its maximum at some values of the K ratio.

If the ratio, K_1/K_2, can be varied arbitrarily, it is more preferable to set K_1/K_2 to the value at which the target higher harmonic becomes most intense. In this point of view, the magnet configuration shown in Fig. 6.2 (b) is better than Fig. 6.2 (a).

Chapter 8

Conclusions

Two novel IDs were proposed in this thesis, which would improve the disadvantages of ordinary IDs. One is the figure-8 undulator for linear polarization with low on-axis power density and the other is the rhombus undulator for high-energy photons with a circular polarization.

The figure-8 undulator is the ID which has an advantage that the on-axis power density is quite low even when high K values are applied. This is quite important for the SR facility using an electron beam with an extremely high energy to supply low-energy photons with a linear polarization, for example, VUV and SX. In particular, for the long straight section, such as the 30-m straight section at the SPring-8, the figure-8 undulator should be used as the ID for linear polarization since the heat problem may be quite serious for planar undulators.

The helical undulator, in addition to the figure-8 undulator, is preferable for supplying low-energy photons. In this case, the polarization is circular. Therefore, users who want linearly-polarized photons can use the figure-8 undulator, while other users who want circularly-polarized photons can use the helical undulator. For the IDs to be installed in the long-straight section, however, another problem may limit the available energy range.

In the case of the ID which has the horizontal field, such as the helical and figure-8 undulators, there is a possibility that the power radiated at the entrance of the ID may damage the vacuum chamber if the vertical aperture of the vacuum chamber

between the gap of the ID is small and the total length of the ID is long. For example, let us consider the case that the vertical aperture of the vacuum chamber is 15 mm and the total length of the ID is 30 m. In this case, the minimum aperture for SR emitted at the entrance is calculated as 15(mm)/2/30(m) = $\pm 250(\mu m)$. If the electron energy is 8 GeV, this correspond to $\pm 3.9/\gamma$. Remembering the fact that the power radiated from the ID has the angular width of $K_{x,y}/\gamma$, the maximum horizontal K value should be smaller than 3.9. Therefore, the maximum K value is equal to about 3.0 in the case of the helical undulator, which limits the available energy of photons.

In the case of the figure-8 undulator, however, K_y does not have to be equal to K_x necessarily. Therefore, K_y can be set to a value as high as the magnetic configuration and other mechanical support arrow, which means that the available energy is not limited. We can say from this fact that the figure-8 undulator should be adopted as the ID for the long straight section in an SR facility for suppressing the heat load.

The rhombus undulator is the ID which has the advantage that higher harmonics with a circular polarization can be obtained even when K values are low. This device is fitted for an SR facility using an electron beam with a medium energy to supply VUV and SX with a circular polarization. The radiation from the elliptical and crossed undulators also contains higher harmonics with a circular polarization but the intensity of higher harmonics obtained from the elliptical undulator is not sufficiently high and the achievable degree of polarization is quite low in the case of the crossed undulator. On the other hand, the degree of circular polarization obtained from the rhombus undulator is sufficiently high even for the large angular divergence of the beam. In addition, the intensity of higher harmonics is larger than that of the elliptical undulator. Therefore, the users who want the high degree of polarization should adopt the rhombus undulator. What is preferable with respect to the rhombus undulator is that it can be used as a simple helical undulator, which

makes it possible to cover a quite wide range of energies, for example, from 2 eV to 1000 eV.

The essence of the two IDs proposed in this thesis is to obtain linearly (circularly) polarized SR in the energy region where circularly (linearly) polarized SR can be obtained easily. In other words, the proposed IDs have the roll to convert the circular (linear) polarization to the linear (circular) polarization. It should be noted that there is another method to convert linear or circular polarization using the Bragg diffraction. Although this technique can convert linear or circular polarization easily by using an ordinary crystal monochromator, the available energy range may be between 2 keV and 20 keV and cannot be used in the range of VUV and SX. Therefore, we can say that the figure-8 and rhombus undulators are regarded as to be quite valuable because they can cover the energy range of SR which has never been available only by using ordinary IDs.

Appendix A

Calculation of the Spectrum Obtained from Various IDs

Here, the photon flux density for each harmonic obtained from various types of undulator are calculated using the equations derived in section 2.3.

A.1 Planar undulator

Substituting (2.85) and (2.41), the exponent in equation (2.34) is calculated as

$$-i\omega_1 k\left(t' - \frac{\boldsymbol{n}\cdot\boldsymbol{r}}{c}\right) = -i(k\omega_0 t' - X\sin\omega_0 t' + Y\sin 2\omega_0 t'), \tag{A.1}$$

with

$$X = \frac{2kK\gamma\theta\cos\phi}{1+K^2/2+\gamma^2\theta^2}, \tag{A.2}$$

$$Y = \frac{kK^2}{4(1+K^2/2+\gamma^2\theta^2)}. \tag{A.3}$$

Neglecting the term of the order γ^{-2}, we have

$$Q_{kx} = \frac{K}{\gamma\omega_0}\int_0^{2\pi}\cos\eta\,\mathrm{e}^{-i(k\eta - X\sin\eta + Y\sin 2\eta)}d\eta, \tag{A.4}$$

$$Q_{kz} = \int_0^{2\pi}\frac{1}{\omega_0}\,\mathrm{e}^{-i(k\eta - X\sin\eta + Y\sin 2\eta)}d\eta, \tag{A.5}$$

where we have replaced $\omega_0 t'$ by η. Integrals in equations (A.4) and (A.5) can be expressed by the Bessel function $J_n(x)$. Bessel function is defined as

$$J_n(x) = \sum_{j=0}^{\infty}\frac{(-1)^j}{j!}\frac{(x/2)^{n+2j}}{(n+j)!}. \tag{A.6}$$

Using the generating function for the Bessel functions

$$\mathrm{e}^{z(t-1/t)/2} = \sum_{n=-\infty}^{\infty} t^n J_n(z), \tag{A.7}$$

we obtain the relation

$$\mathrm{e}^{ix\sin y} = \sum_{n=-\infty}^{\infty} J_n(x)\,\mathrm{e}^{iny}. \tag{A.8}$$

Using the relation (A.8), equations (A.4) and (A.5) are rewritten as

$$\begin{aligned} Q_{kx} &= \frac{K}{\gamma\omega_0}\sum_{q=-\infty}^{\infty}\sum_{p=-\infty}^{\infty} J_q(X)J_p(Y) \\ &\quad\times\int_0^{2\pi}\cos\eta\exp[-i\eta(k-q+2p)]d\eta, \end{aligned} \tag{A.9}$$

$$\begin{aligned} Q_{kz} &= \frac{1}{\omega_0}\sum_{q=-\infty}^{\infty}\sum_{p=-\infty}^{\infty} J_q(X)J_p(Y) \\ &\quad\times\int_0^{2\pi}\exp[-i\eta(k-q+2p)]d\eta. \end{aligned} \tag{A.10}$$

Integrating directly, we have

$$Q_{kx} = \begin{cases} \dfrac{\pi K}{\gamma\omega_0}; & q = 2p+k\pm 1, \\ 0; & q \neq 2p+k\pm 1, \end{cases} \tag{A.11}$$

$$Q_{kz} = \begin{cases} \dfrac{2\pi}{\omega_0}; & q = 2p+k, \\ 0; & q \neq 2p+k. \end{cases} \tag{A.12}$$

Introducing a new function S_j defined as

$$S_j = \sum_{p=-\infty}^{\infty} J_p(Y)J_{2p+K+j}(X), \tag{A.13}$$

the components of $\boldsymbol{Q}$ are calculated as

$$\begin{aligned} Q_{kx} &= \frac{\pi K}{\gamma\omega_0}(S_{-1}+S_1), \\ Q_{ky} &= 0, \\ Q_{kz} &= \frac{2\pi}{\omega_0}S_0. \end{aligned} \tag{A.14}$$

Substituting into equation (2.49), we have

$$F_{k\parallel} = \frac{ik\omega_1^2 e}{8\pi^2\epsilon_0 c}\,\mathrm{e}^{-i\omega_1 kR_0/c}\frac{\pi}{\omega_0}\left[-\frac{K}{\gamma}(S_{-1}+S_1)+2S_0\theta\cos\phi\right], \tag{A.15}$$

$$F_{k\perp} = \frac{ik\omega_1^2 e}{8\pi^2\epsilon_0 c}\,\mathrm{e}^{-i\omega_1 kR_0/c}\frac{2\pi}{\omega_0}S_0\theta\sin\phi. \tag{A.16}$$

From above equations, it is found that each harmonic is linearly polarized because $F_{k\parallel}$ and $F_{k\perp}$ have the same phase. The photon flux density for the k-th harmonic is calculated as

$$\frac{d^2P_k}{d\Omega d\omega} = \frac{e^2\gamma^2}{4\pi\epsilon_0 c}(f_x^2+f_y^2), \tag{A.17}$$

with

$$f_x(\gamma\theta,\phi) = \xi[2S_0\gamma\theta\cos\phi - K(S_1+S_{-1})]P_N, \tag{A.18}$$

$$f_y(\gamma\theta,\phi) = 2\xi S_0\gamma\theta\sin\phi P_N, \tag{A.19}$$

$$\xi = \frac{k}{1+K^2/2+\gamma^2\theta^2}. \tag{A.20}$$

A.2 Elliptical undulator

Substituting equations (2.104) and (2.105), the exponent in equation (2.34) is calculated as

$$\begin{aligned} & -i\omega_1 k\left(t'-\frac{\boldsymbol{n}\cdot\boldsymbol{r}}{c}\right) \\ = \; & -i(k\omega_0 t' - A\sin\omega_0 t' + B\cos\omega_0 t' + Y\sin 2\omega_0 t'), \end{aligned} \tag{A.21}$$

with

$$A = \frac{2kK_y\gamma\theta\cos\phi}{1+K_x^2/2+K_y^2/2+\gamma^2\theta^2}, \tag{A.22}$$

$$B = \frac{2kK_x\gamma\theta\sin\phi}{1+K_x^2/2+K_y^2/2+\gamma^2\theta^2}, \tag{A.23}$$

$$Y = \frac{k(K_y^2-K_x^2)}{4(1+K_x^2/2+K_y^2/2+\gamma^2\theta^2)}. \tag{A.24}$$

In the same manner as the planar-undulator case, we have

$$\begin{aligned} Q_{kx} &= \frac{\pi K_y}{\gamma\omega_0}(S_{-1}+S_1), \\ Q_{ky} &= -\frac{\pi K_x}{\gamma\omega_0}(S_{-1}-S_1), \\ Q_{kz} &= \frac{2\pi\beta}{\omega_0}S_0, \end{aligned} \tag{A.25}$$

with

$$S_j = \sum_{p=-\infty}^{\infty} J_p(Y)J_{k+2p+j}(X)\,\mathrm{e}^{-i(k+2p+j)\zeta}, \tag{A.26}$$

$$X = \frac{2\gamma\theta\sqrt{K_x^2\sin^2\phi+K_y^2\cos^2\phi}}{1+\gamma^2\theta^2+K_x^2/2+K_y^2}, \tag{A.27}$$

$$\zeta = \tan^{-1}\left(\frac{K_x}{K_y}\tan\phi\right). \tag{A.28}$$

The two components of $\boldsymbol{F}_k$ are calculated as

$$F_{k\parallel} = \frac{ik\omega_1^2 e}{8\pi^2\epsilon_0 c}\,\mathrm{e}^{-i\omega_1 kR_0/c}\frac{\pi}{\omega_0}\left[-\frac{K_y}{\gamma}(S_{-1}+S_1)+2S_0\theta\cos\phi\right], \tag{A.29}$$

$$F_{k\perp} = \frac{ik\omega_1^2 e}{8\pi^2\epsilon_0 c}\,\mathrm{e}^{-i\omega_1 kR_0/c}\frac{2\pi}{\omega_0}\left[i\frac{K_x}{\gamma}(S_{-1}+S_1)+2S_0\theta\sin\phi\right]. \tag{A.30}$$

From above equations, the photon flux density for the k-th harmonic is calculated as

$$\frac{dP_k}{d\Omega d\omega} = \frac{e^2\gamma^2N^2}{4\pi\epsilon_0 c}(|f_x|^2+|f_y|^2), \tag{A.31}$$

with

$$f_x(\gamma\theta,\phi) = \xi[2S_0\gamma\theta\cos\phi - K_x(S_1+S_{-1})]P_N, \tag{A.32}$$

$$f_y(\gamma\theta,\phi) = \xi[2S_0\gamma\theta\sin\phi - iK_y(S_1+S_{-1})]P_N, \tag{A.33}$$

$$\xi = \frac{k}{1+K_x^2/2+K_y^2+\gamma^2\theta^2}. \tag{A.34}$$

A.3 Figure-8 undulator

A.3.1 Ideal case

In calculating $\boldsymbol{Q}_k$ by equation (2.34), it should be noted that the period T' and the frequency ω_1 should be replaced by $2T'$ and $\omega_1/2$, respectively. This is originated from the fact that the practical period length of the device is not λ_u but $2\lambda_u$, which is the period length of the vertical undulator. In addition, N should be replaced by $N/2$ in calculating the photon flux density by equations (2.39) and (2.40) because the practical number of periods is not N but $N/2$.

Substituting equations (3.8) and (3.9), the exponent in equation (2.34) is calculated as

$$\begin{aligned} &-i(\omega_1/2)k\left(t'-\frac{\boldsymbol{n}\cdot\boldsymbol{r}}{c}\right) \\ &= \begin{cases} -i[k\omega_0 t'/2 + Y(\cos\omega_0 t'-1) - X\sin\omega_0 t'] \\ \quad ; 4n\pi \le \omega_0 t' < 2(2n+1)\pi, \\ -i[k\omega_0 t'/2 + Y(1-\cos\omega_0 t') - X\sin\omega_0 t'] \\ \quad ; 2(2n+1)\pi \le \omega_0 t' < 4(n+1)\pi, \end{cases} \end{aligned} \tag{A.35}$$

with

$$X = kK\xi\gamma\theta\cos\phi, \tag{A.36}$$

$$Y = kK\xi\gamma\theta\sin\phi, \tag{A.37}$$

$$\xi = \frac{k}{1+K^2+\gamma^2\theta^2}, \tag{A.38}$$

where n is an integer.

Replacing $\omega_0 t'$ by η, we have

$$\begin{aligned} Q_{kx} &= \frac{K}{\gamma\omega_0}\left[\mathrm{e}^{iY}\int_0^{2\pi}\cos\eta\,\mathrm{e}^{-i(k\eta/2+Y\cos\eta-X\sin\eta)}d\eta\right. \\ &\qquad \left. + \mathrm{e}^{iY}\int_{2\pi}^{4\pi}\cos\eta\,\mathrm{e}^{-i(k\eta/2-Y\cos\eta-X\sin\eta)}d\eta\right], \\ Q_{ky} &= \frac{K}{\gamma\omega_0}\left[\mathrm{e}^{iY}\int_0^{2\pi}\sin\eta\,\mathrm{e}^{-i(k\eta/2+Y\cos\eta-X\sin\eta)}d\eta\right. \\ &\qquad \left. - \mathrm{e}^{iY}\int_{2\pi}^{4\pi}\sin\eta\,\mathrm{e}^{-i(k\eta/2-Y\cos\eta-X\sin\eta)}d\eta\right], \\ Q_{kz} &= \frac{1}{\omega_0}\left[\mathrm{e}^{iY}\int_0^{2\pi}\mathrm{e}^{-i(k\eta/2+Y\cos\eta-X\sin\eta)}d\eta\right. \\ &\qquad \left. - \mathrm{e}^{iY}\int_{2\pi}^{4\pi}\mathrm{e}^{-i(k\eta/2-Y\cos\eta-X\sin\eta)}d\eta\right]. \end{aligned} \tag{A.39}$$

From equation (A.8), we have

$$\mathrm{e}^{ix\cos y} = \mathrm{e}^{ix\sin(y+\pi/2)} = \sum_{n=-\infty}^{\infty} i^n J_n(x)\,\mathrm{e}^{iny}. \tag{A.40}$$

Using equations (A.8) and (A.40), Q_{kx} is calculated as follows,

$$\begin{aligned} &Q_{kx} \\ &= \frac{K}{\gamma\omega_0}\left[\mathrm{e}^{iY}\int_0^{2\pi}\cos\eta\,\mathrm{e}^{-ik\eta/2}\sum_p(-i)^p J_p(Y)\,\mathrm{e}^{ip\eta}\sum_q J_q(X)\,\mathrm{e}^{iq\eta}d\eta\right. \\ &\quad \left. + \mathrm{e}^{-iY}\int_{2\pi}^{4\pi}\cos\eta\,\mathrm{e}^{-ik\eta/2}\sum_p i^p J_p(Y)\,\mathrm{e}^{ip\eta}\sum_q J_q(X)\,\mathrm{e}^{iq\eta}d\eta\right] \\ &= \frac{K}{2\gamma\omega_0}\left[\mathrm{e}^{iY}\sum_p\sum_q(-i)^p J_p(Y)J_q(X)\right. \\ &\quad \int_0^{2\pi}\left[\mathrm{e}^{i\eta(1-k/2+p+q)} + \mathrm{e}^{i\eta(-1+k/2+p+q)}\right]d\eta \\ &\quad + \mathrm{e}^{-iY}\sum_p\sum_q i^p J_p(Y)J_q(X) \\ &\quad \left.\int_{2\pi}^{4\pi}\left[\mathrm{e}^{i\eta(1-k/2+p+q)} + \mathrm{e}^{i\eta(-1+k/2+p+q)}\right]d\eta\right] \\ &= \begin{cases} \dfrac{\pi K}{\gamma\omega_0}(S_{-1}^+ + S_1^+); & k = \text{even number}, \\ \dfrac{2iK}{\gamma\omega_0}(R_{-2}^- + R_2^-); & k = \text{odd number}, \end{cases} \end{aligned} \tag{A.41}$$

with

$$f_p^{\pm}(Y) = (-i)^p \, \mathrm{e}^{iY} \pm i^p \, \mathrm{e}^{-iY}, \tag{A.42}$$

$$S_j^{\pm} = \sum_p J_{k/2-p+j}(X) J_p(Y) f_p^{\pm}, \tag{A.43}$$

$$R_j^{\pm} = \sum_p \sum_q \frac{1}{2p+2q-k+j} J_p(Y) J_q(X) f_p^{\pm}. \tag{A.44}$$

In the same manner, other components of $\boldsymbol{Q}_k$ are calculated as

$$Q_{ky} = \begin{cases} -\dfrac{i\pi K}{\gamma\omega_0}(S_{-1}^- - S_1^-); & k = \text{even number}, \\ -\dfrac{2K}{\gamma\omega_0}(R_{-2}^+ - R_2^+); & k = \text{odd number}, \end{cases} \tag{A.45}$$

$$Q_{kz} = \begin{cases} \dfrac{2\pi}{\omega_0} S_0^+; & k = \text{even number}, \\ \dfrac{4i}{\omega_0} R_0^-; & k = \text{odd number}. \end{cases} \tag{A.46}$$

Substituting into equation (2.49), we obtain

$$F_{k\parallel} = \frac{ik(\omega_1/2)^2 e}{8\pi^2\epsilon_0 c} \, \mathrm{e}^{-i(\omega_1/2)kR_0/c} \times \begin{cases} \left[-\dfrac{\pi K}{\gamma\omega_0}(S_{-1}^+ + S_1^+) + \dfrac{2\pi\theta\cos\phi}{\omega_0} S_0^+ \right] \\ \quad ; k = \text{even number}, \\ \left[-\dfrac{2iK}{\gamma\omega_0}(R_{-2}^- + R_2^-) + \dfrac{4i\theta\cos\phi}{\omega_0} R_0^- \right] \\ \quad ; k = \text{odd number}, \end{cases} \tag{A.47}$$

$$F_{k\perp} = \frac{ik(\omega_1/2)^2 e}{8\pi^2\epsilon_0 c} \, \mathrm{e}^{-i(\omega_1/2)kR_0/c} \times \begin{cases} \left[\dfrac{i\pi K}{\gamma\omega_0}(S_{-1}^- - S_1^-) + \dfrac{2\pi\theta\sin\phi}{\omega_0} S_0^+ \right] \\ \quad ; k = \text{even number}, \\ \left[\dfrac{2K}{\gamma\omega_0}(R_{-2}^+ - R_2^+) + \dfrac{4i\theta\sin\phi}{\omega_0} R_0^- \right] \\ \quad ; k = \text{odd number}. \end{cases} \tag{A.48}$$

From above equations, the photon flux density for the k-th harmonic is calculated as

$$\frac{dP_k}{d\Omega d\omega} = \frac{e^2\gamma^2(N/2)^2}{4\pi\epsilon_0 c}(|f_x|^2 + |f_y|^2), \tag{A.49}$$

with

$$f_x = P_N \begin{cases} -\dfrac{K}{2}(S_{-1}^+ + S_1^+) + \gamma\theta\cos\phi S_0^+; & k = \text{even number}, \\ -iK(R_{-2}^- + R_2^-) + 2i\gamma\theta\cos\phi R_0^-; & k = \text{odd number}, \end{cases} \tag{A.50}$$

$$f_y = P_N \begin{cases} \dfrac{iK}{2}(S_{-1}^- - S_1^-) + \gamma\theta\sin\phi S_0^+; & k = \text{even number}, \\ K(R_{-2}^+ - R_2^+) + 2i\gamma\theta\sin\phi R_0^-; & k = \text{odd number}, \end{cases} \tag{A.51}$$

$$\begin{aligned} P_N &= \frac{\sin\pi(N/2)\omega/(\omega_1/2)}{\pi(N/2)(\omega/(\omega_1/2) - k)} \\ &= \frac{\sin\pi N\omega/\omega_1}{\pi N(\omega/\omega_1 - k/2)}. \end{aligned} \tag{A.52}$$

From equation (A.52), it is found that the peak energy for the k-th harmonic is $k\omega_1/2$. This looks strange. For convenience, we introduce a new harmonic number n defined as $n = k/2$. Since k is an integer, n contains not only integers but also half-odd integers.

A.3.2 Practical case

In calculating the photon flux density using equations (2.34), (2.39) and (2.40), T', ω_1 and N should be replaced by $2T'$, $\omega_1/2$, and $N/2$, respectively. This is due to the same reason as the ideal case.

Substituting (3.24) and (3.25), the exponent in equation (2.34) is calculated as

$$\begin{aligned} &-i(\omega_1/2)k\left(t' - \frac{\boldsymbol{n}\cdot\boldsymbol{r}}{c}\right) \\ &= -i\left(\frac{k\omega_0 t'}{2} - X\sin\frac{\omega_0 t'}{2} + Y\sin\omega_0 t' + Z\sin 2\omega_0 t'\right), \end{aligned} \tag{A.53}$$

with

$$X = 4\xi K_x \gamma\theta \sin\phi, \tag{A.54}$$

$$Y = \xi\left[\frac{K_x^2}{2} - 2K_y\gamma\theta\cos\phi\right], \tag{A.55}$$

$$Z = \frac{\xi K_y^2}{4}, \tag{A.56}$$

$$\xi = \frac{k/2}{1 + K_x^2/2 + K_y^2/1 + \gamma^2\theta^2}. \tag{A.57}$$

Replacing $\omega_0 t'$ by η, we have

$$Q_{kx} = \frac{K_y}{\gamma\omega_0}\int_0^{4\pi} \cos\eta\, \mathrm{e}^{i(k\eta - X\sin\eta/2 + Y\sin\eta + Z\sin 2\eta)} d\eta. \tag{A.58}$$

Using the relations for Bessel functions (A.8), we have

$$Q_{kx} = \frac{2\pi K_y}{\gamma\omega_0}(S_2 + S_{-2}), \tag{A.59}$$

with

$$S_j = \sum_p \sum_q J_{k+2q+4p+j}(X) J_q(Y) J_p(Z). \tag{A.60}$$

In the same manner, we have

$$Q_{ky} = \frac{2\pi K_x}{\gamma\omega_0}(S_1 + S_-), \tag{A.61}$$

$$Q_{kz} = \frac{4\pi}{\omega_0} S_0. \tag{A.62}$$

As well as the ideal case, we introduce a new harmonic number n defined as $n = k/2$. The photon flux density for the n-th harmonic is calculated as

$$\frac{d^2 P_n}{d\Omega d\omega} = \frac{e^2\gamma^2 N^2}{4\pi\epsilon_0 c}(f_x^2 + f_y^2), \tag{A.63}$$

with

$$f_x = \xi[2S_0\gamma\theta\cos\phi - K_y(S_2 + S_{-2})]P_N, \tag{A.64}$$

$$f_y = \xi[2S_0\gamma\theta\sin\phi - K_x(S_1 + S_{-1})]P_N. \tag{A.65}$$

Appendix B

Effects Due to the Angular Divergence

Let us consider the effect of the angular divergence on the spectrum and the degree of polarization. As shown in Fig. B.1, radiation emitted from an electron which has a slope θ with respect to the beam axis is observed with an emission angle θ by an observer on axis. Considering this fact, the photon flux density is calculated as

$$\frac{d^2P_k}{d\Omega d\omega} = \frac{e^2\gamma^2N^2}{4\pi\epsilon_0 c}(S_{xx}+S_{yy}), \tag{B.1}$$

$$S_{ab} = \int_{-\infty}^{\infty} d\xi \int_{-\infty}^{\infty} d\eta \; g(\xi,\eta) f_a^*(u,\alpha) f_b(u,\alpha), \tag{B.2}$$

where $g(\xi,\eta)$ is the probability distribution function of the beam and

$$u = \gamma\sqrt{(\theta_x-\xi)^2+(\theta_y-\eta)^2}, \tag{B.3}$$

$$\alpha = \tan^{-1}\left(\frac{\theta_x-\xi}{\theta_y-\eta}\right). \tag{B.4}$$

If the probability distribution function is of the Gaussian type, g is expressed as

$$g(\xi,\eta) = \frac{1}{2\pi\sigma_{x'}\sigma_{y'}}\exp\left(-\frac{\xi^2}{\sigma_{x'}^2}-\frac{\eta^2}{\sigma_{y'}^2}\right), \tag{B.5}$$

where $f_{x,y}$ are the functions defined by equation (2.51) and $\sigma_{x',y'}$ are the horizontal and vertical angular divergences. Expressing ξ and η by u and α, equation (B.2) is

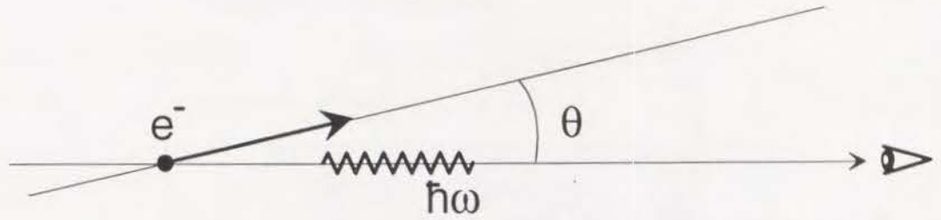

Figure B.1. Radiation emitted from an electron which has a slope with respect to the beam axis.

rewritten as

$$S_{ab} = \frac{1}{2\pi\gamma^2\sigma_{x'}\sigma_{y'}}\int_0^{\infty} u du \int_{-\pi}^{\pi} d\alpha f_a^*(u,\alpha) f_b(u,\alpha) \exp\left[-\frac{(u\cos\alpha-\gamma\theta\cos\phi)^2}{2\gamma^2\sigma_{x'}^2}-\frac{(u\sin\alpha-\gamma\theta\sin\phi)^2}{2\gamma^2\sigma_{y'}^2}\right]. \tag{B.6}$$

The degree of linear and circular polarization, P_L and P_C are given by

$$P_L = \frac{S_{xx}-S_{yy}}{S_{xx}+S_{yy}}, \tag{B.7}$$

$$P_C = \frac{2\mathrm{Im}(S_{xy})}{S_{xx}+S_{yy}}. \tag{B.8}$$

Appendix C

Development of the In-vacuum Undulator

As well as the brilliance, the tunability is one of the most important features of the undulator. Because the energy of the fundamental radiation depends on the K value, or the magnetic field, the strong magnetic field is desired for sufficient tunability of the undulator.

In order to obtain the strong field in the ID, the gap between the magnet arrays should be as small as possible. The minimum gap of the ordinary ID is considered to be the sum of the vertical aperture and the thickness of the vacuum chamber. If the magnet arrays are placed in the vacuum chamber, the minimum gap is just equal to the minimum vertical aperture not to cause the loss of the beam life time. Such a type of undulator is called an in-vacuum undulator [50].

Recently, the construction of the pilot in-vacuum undulator to be installed in the SPring-8 has been almost finished. This undulator has the period length of 32 mm, the number of periods of 140 and the minimum gap of 8 mm. The magnet material is the rare earth iron boron called NEOMAX33UH, an anisotropic sintered magnet composed basically of neodymium, iron and boron, produced by Sumitomo Special Metals co., ltd. with the remanent field of 1.15T. The available energy of the fundamental radiation obtained from this undulator is between 6 keV and 18 keV. Taking the use of the third harmonic into account, up to 40 keV is available.

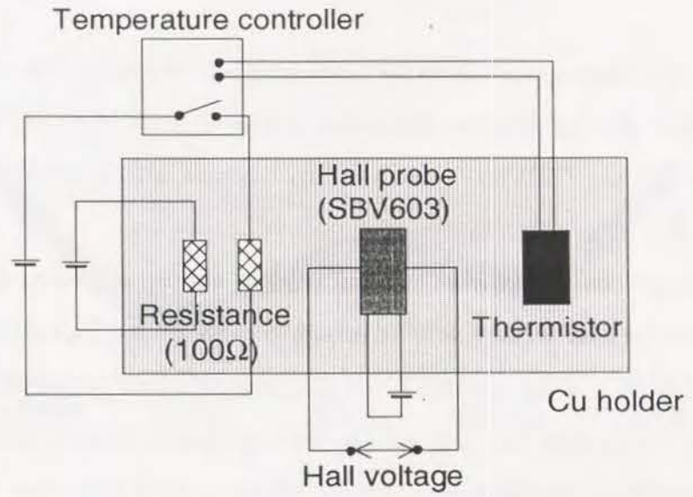

Figure C.1. Schematic illustration of the constructed apparatus.

The technology of the in-vacuum undulator can be applied not only to ordinary undulators but also to the novel IDs proposed in this thesis. Therefore, it is interesting to review the development of the in-vacuum undulator for the future construction of the figure-8 and rhombus undulators.

There are many techniques to be developed in realizing the in-vacuum undulator. Among them, two techniques, i. e., the magnetic field correction and the ultra-high-vacuum system, are important. Here, these two techniques are described.

C.1 Field measurement and correction

C.1.1 Construction of the field-measuring system

First, the system to measure the magnetic field accurately is described. In general, the magnetic field in the ID is measured by the Hall probe. Because the output of the Hall probe is sensitive to temperature, it is necessary to place the Hall probe in a temperature-stabilized environment for the accurate measurement of the magnetic field. Figure C.1 shows the schematic illustration of the constructed apparatus to measure the magnetic field. Four elements were contained in the copper

holder. By flowing currents in the resistances and adjusting them by the temperature controller, the temperature inside was stabilized at 28.00±0.01 °C. The type of the Hall probe was "SBV603", produced by Siemens with a temperature coefficient of -0.1%/K.

Because the output from the Hall probe is not the absolute value of the magnetic field but the Hall voltage, it is necessary to calibrate the Hall probe. The calibration was made by placing the Hall probe in a magnetic field generated by an electromagnet and comparing the Hall voltage with the magnetic field measured by an NMR (Nuclear Magnetic Resonance) probe: the calibration curve was then obtained by a least-square fitting of the calibration data with an 11th-order polynomial.

It is necessary to investigate the variation of the measurement according to the passage of time because the field measurement in the ID takes a lot of time, typically 3 hours. In order to investigate the variation, the magnetic field at the fixed position where the magnetic field was 3926 Gauss was measured for 6 hours and it was found that the variation was within 0.2 Gauss, which was correspondent to 5.1×10^{-3}%. This can be considered to be negligibly small.

C.1.2 Result of the field measurement

The magnetic field was measured at the gap of 15 mm. The simplest way to estimate the quality of the magnetic field is to calculate the electron orbit inside. Figure C.2 shows the electron orbit calculated using the measured field. It was found from the figure that there were many points where the orbit was deflected remarkably (they are often called kicks). Because these kicks would degrade the coherence between radiation waves emitted at various points of the trajectory, some correction should be made.

C.1.3 Method of correction

The simplest way to correct the magnetic field in the ID is to place a thin steel plate (shim) onto the surface of the magnet block whose magnetization is weaker

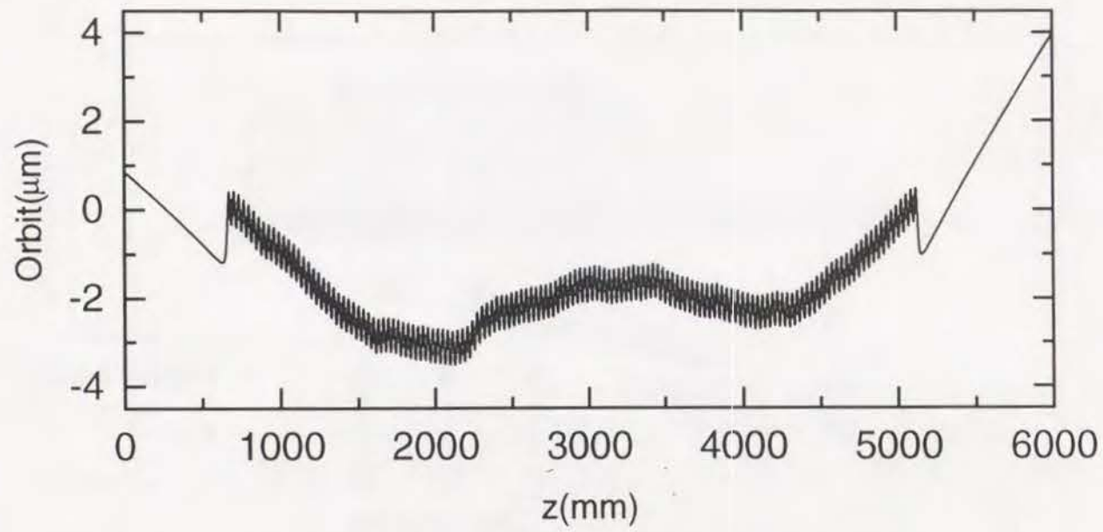

Figure C.2. Electron orbit calculated using the measured field of the in-vacuum undulator at the gap of 15 mm.

than the average. This technique is called "shimming" and widely used for the field correction of the ID [48]. As well as the shimming, shifting the magnet block upward or downward is an effective method to correct the magnetic field. Although it is possible to correct the magnetic field easily by using these two techniques, they do not fit to the field correction of the in-vacuum undulator. The reason is as follows: It is well known that an electromagnetic field is created whenever a relativistic charged particle travels near a material that is not perfectly smooth. This is called a wake field which, in turn, can act back on the particles traveling behind the one that created it [49]. If the wake field lasts for a sufficiently long time, it will affect the particles in trailing bunches in successive turns, which causes the instability of the electron beam. Therefore, the shimming and shifting techniques cannot be used because they cause the roughness on the surface of the magnet arrays near which the electron beam travels.

The method adopted for the field correction of the in-vacuum undulator was to insert chip magnets into the holder which held the permanent magnet block, as shown in Fig. C.3. There were three holes in the holder, into which up to two chip

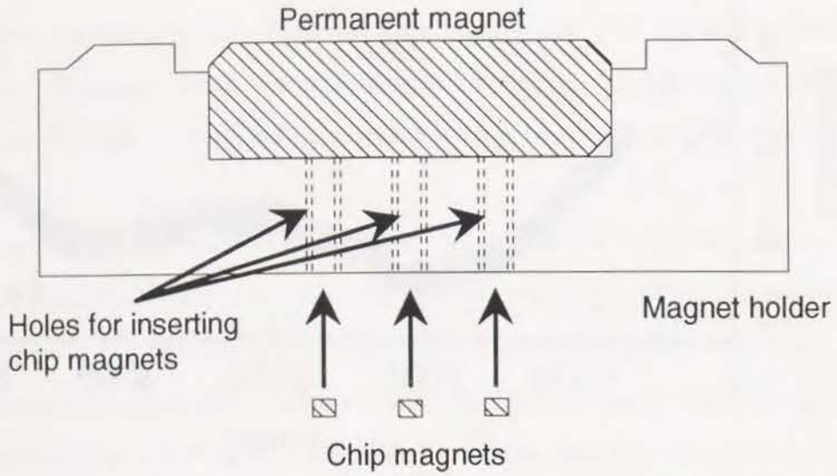

Figure C.3. Schematic illustration of the magnet holder and chip magnets to correct the magnetic field.

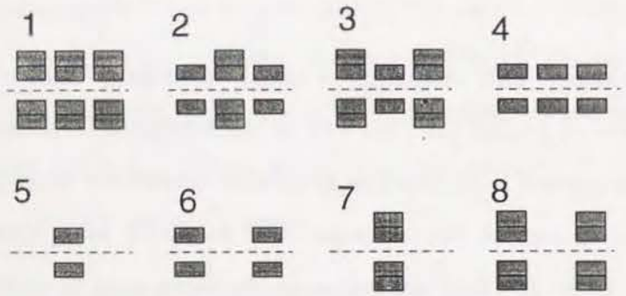

Figure C.4. Arrangement of inserting chip magnets. Eight cases are shown.

magnets could be inserted. If the peak magnetic field of the specific pole was weaker (strong) than the average, the chip magnet(s) should be inserted at the position of that pole in the direction where the force between the magnet block and the chip magnet was attractive (repulsive). Unlike the shimming, this method never causes the roughness on the surface of the magnet arrays.

In order to investigate the effect of inserting the chip magnets, the field integral for each pole, I_n, defined by

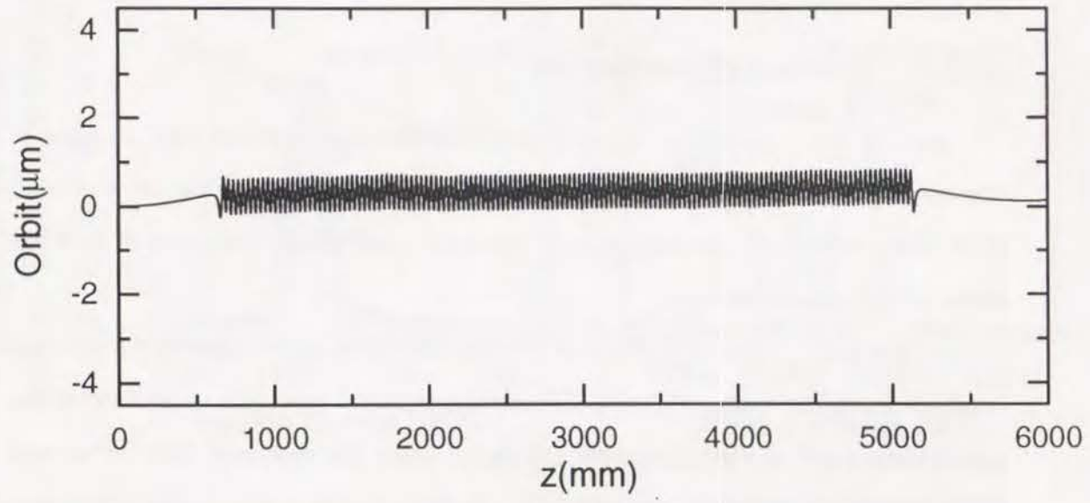

Figure C.5. Electron orbit calculated using the measured field after correction.

$$I_n = \int_{z_n}^{z_{n+1}} B_y(z)dz, \tag{C.1}$$

was calculated before and after inserting chip magnets. Here, z_n is the n-th point where B_y becomes equal to zero and I_n means the deflection caused by the n-th pole. Taking the subtraction of I_n before and after inserting chip magnets, the effect was calculated as the variation of I_n. The effect was investigated in eight cases of arrangements of inserting chip magnets, as shown in Fig. C.4. The typical value of I_n was about 4000 G·cm and the maximum variation of I_n was about 60 G·cm or 1.5% of I_n, which can be considered to be sufficient for the field correction because the standard deviation of I_n was found to be 0.79%.

In addition to the correction of each pole of the magnet described above, the end correction was also done. This means that pairs of magnets were placed at the entrance and the exit of the undulator, such that the center of the electron wiggle corresponded to the undulator axis.

C.1.4 Results of correction

For the field correction, the chip magnets were inserted into 180 positions of the magnet pole. Figure C.5 shows the electron orbit calculated using the measured field after correction. As can be seen, the kicks have almost disappeared and the orbit looked almost straight.

In order to investigate the effect of the field correction quantitatively, the spectral analysis should be made. Figure C.6 shows the expected spectrum of the fundamental radiation and the 9th harmonic calculated using the measured field before and after correction. In the same figure, the ideal spectrum is also shown. The electron energy was assumed to be 8 GeV and the average current 100 mA. As for the fundamental radiation, the intensities of both cases were almost equivalent to the ideal one. On the other hand, the intensity of the 9th harmonic after correction was twice as that before correction, which showed that the method of correction was quite effective. After the field correction, the magnet was baked at the temperature between 130°C and 135°C throughout the baking process of the vacuum test of the in-vacuum undulator, to be described later. Then the magnetic field was measured again and it was found that the difference between the magnetic fields before and after the bakeout was too small to be concerned.

C.2 Ultrahigh-vacuum system

In order to install the undulator in the storage ring, it is necessary to develop a system which can achieve ultrahigh vacuum (UHV; below 10^{-10} Torr). There are two problems to be solved. One is to suppress outgassing from the surfaces of the rare earth magnets due to their porous structure. The other is irreversible demagnetization of the magnets during the UHV bakeout. Since the demagnetization of NEOMAX33UH begins to occur at the temperature higher than 150 °C, the temperature for the bakeout should be lower than 150 °C.

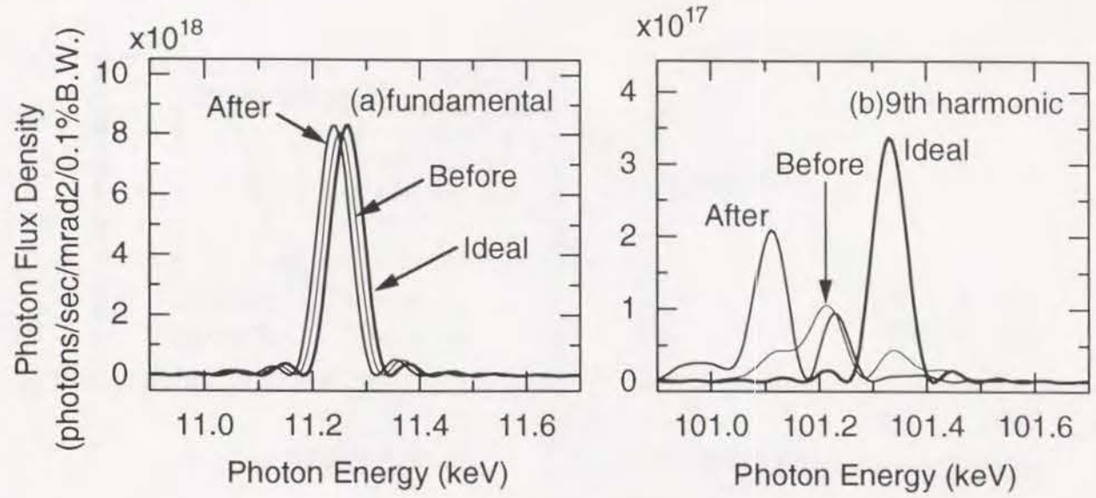

Figure C.6. Expected spectra calculated using the measured field before and after correction in the case of (a) the fundamental and (b) the 9th harmonic. The ideal case is also shown.

C.2.1 Vacuum test of the magnet material coated with TiN

A simple way to suppress outgassing from the magnet is to coat the surface with a specific material. In the case of the SPring-8 in-vacuum undulator, titanium nitride (TiN) was adopted as a material to coat the surface.

In order to test the performance of the TiN coating, the achievable pressure of the vacuum chamber containing the samples of the TiN-coated magnet material was measured and compared to that not containing the samples. Figure C.7 shows the schematic illustration of the experimental apparatus. Four kinds of pump were attached. Among them, the titanium getter pump and the sputter ion pump played an important role to realize UHV. Both pumps utilize titanium as the getter of the remaining gas. In order to monitor UHV, two types of vacuum gauge were attached. One was the Bayard Alpert nude gauge (BA gauge) and the other was the extractor gauge (EX gauge). Both the BA and EX gauges monitor the current of the ion created by the process that the molecule of the remaining gas is ionized by the electrons emitted from the cathode. In such a measurement of the pressure, there

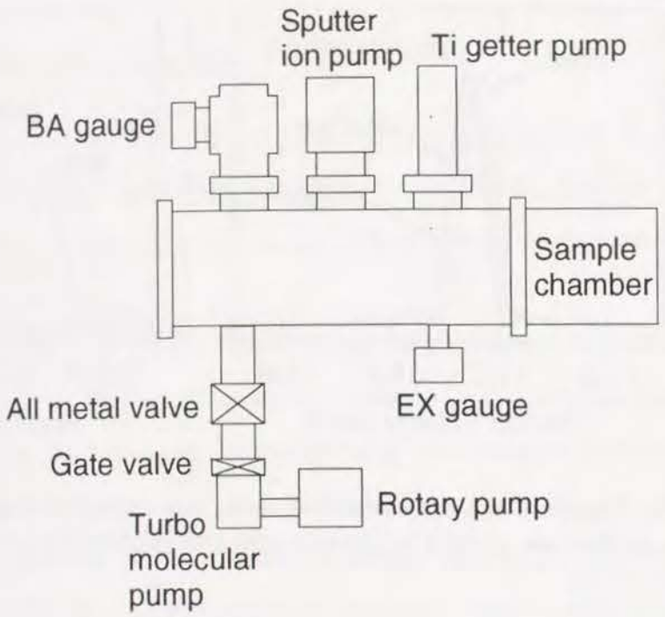

Figure C.7. Experimental apparatus to test the performance of the TiN coating.

is a background called an x-ray limit. This is due to the fact that Bremsstrahlung emitted from the electron when it collides with the anode, in turn, irradiates the collector which collects the ion current and causes the photoemission. It is known from experience that the x-ray limit of the BA gauge is about 2.0×10^{-11} Torr and that of the EX gauge is 1.0×10^{-12} Torr.

The size and the shape of the samples were the same as the magnet block which would be practically used in the in-vacuum undulator. The number of pieces was 60 and the surface area was about 1000 cm^2. In order to avoid the irreversible demagnetization during the UHV bakeout, it is necessary to apply the aging process to the magnets at the temperature somewhat higher than that of the UHV bakeout. In fact, the aging temperature was set to 145 °C, taking into account that the demagnetization of NEOMAX33UH begins to occur at the temperature higher than 150°C. Therefore, the temperature of UHV bakeout should be lower than 145 °C. Actually, the temperature of the sample chamber containing the magnet samples

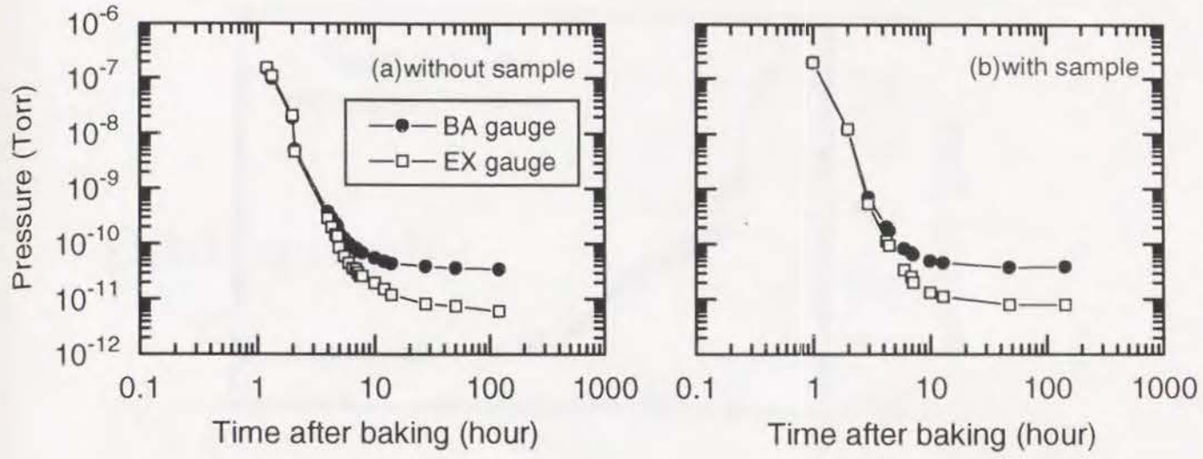

Figure C.8. Pressure of the chamber as a function of time after the bakeout (a) containing no samples and (b)containing 60 magnet blocks.

was stabilized at 135±1°C during the baking process of the vacuum test.

Figures C.8 (a) and (b) show the pressure of the test chamber measured by the BA and EX gauges with and without the samples as a function of time after the bakeout, respectively. Due to the x-ray limit as mentioned previously, the apparent vacuum measured by the BA gauge was worse than that measured by the EX gauge in the range below 10^{-10} Torr. It was found from the figure that the achievable vacuum of the test chamber was about 6×10^{-12} Torr and that there was no difference between two cases with and without the samples. Therefore, we can say that the TiN-coated magnet blocks can be introduced in UHV without any degradation of the vacuum.

C.2.2 Vacuum test of the in-vacuum undulator

After the magnetic field measurement and correction, the magnet arrays were assembled into the vacuum chamber. In order to realize UHV, 12 non-evaporated getter pumps and 6 sputter ion pumps were attached. The temperature of the magnet should be lower than 145 °C during the bakeout, however, high temperature for the bakeout is necessary for good vacuum. Therefore, the temperature of the

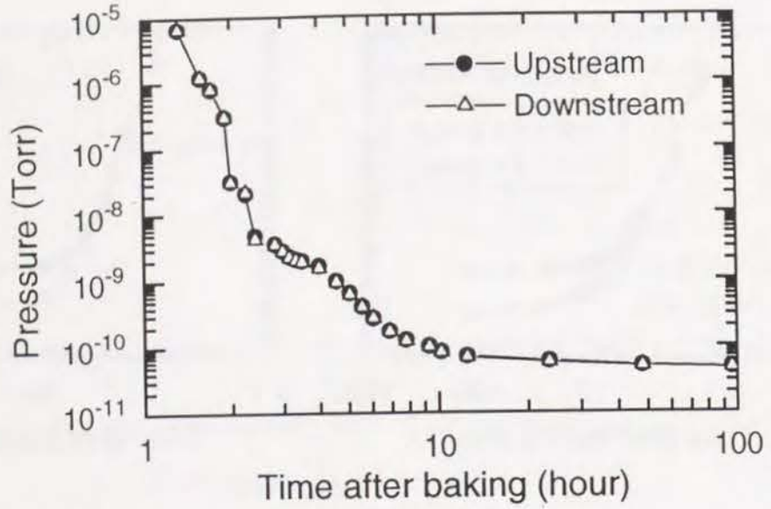

Figure C.9. Pressure measured by the BA gauges attached at the upstream and downstream parts of the chamber of the in-vacuum undulator as a function of time after the bakeout.

magnet was stabilized between 130°C and 135°C by means of adjusting the flux of the cooling water which flowed inside copper pipes laid around the aluminum I-beam assembling the magnet array. The typical temperature of the vacuum chamber was about 200°C.

Since the vacuum chamber of the in-vacuum undulator was long (4.5 m) and consisted of three parts, i. e., upstream, midstream and downstream, two BA gauges were attached at the upstream and downstream parts to monitor the vacuum over a wide area of the chamber. Figure C.9 shows the pressure of the vacuum chamber measured by these two gauges as a function of time after the bakeout. It was found from the figure that there was no difference between the pressures measured upstream and downstream and that the achievable pressure was about 4.3×10^{-11} Torr. Because this value contained the background, the actual pressure was considered to be about 2.0×10^{-11} Torr, which was sufficient to be installed in the storage ring.

Bibliography

[1] J. D. Jackson, *Classical Electrodynamics*, (Wiley, New York, 1965).

[2] J. Shwinger, Phys. Rev. 75(1949)1912.

[3] A. A. Sokolov and I. M. Ternov, *Synchrotron Radiation*, (Pergamon, Oxford, 1968)

[4] G. K. Green, Brookhaven National Laboratory, Report No. 50522 (1976).

[5] D. H. Tomboulian and P. L. Hartman, Phys. Rev. 102(1956)1423.

[6] E. M. Rowe, IEEE Trans. Nucl. Sci. NS-20(1973)973.

[7] H. Kitamura, Rev. Sci. Instrum. 66(1995)2007.

[8] H. Motz, J. App. Phys. 22(1951)527.

[9] H. Motz, W. Thon, and R. N. Whitehurst, J. Apl. Phys. 24(1953)856.

[10] D. Attwood, K. Halbach and K. J. Kim, Science 228(1985)1265.

[11] D. F. Alferov, Y. A. Bashmakov and P. A. Cherenkov, Sov. Phys. Usp. 32(1989)200.

[12] S. Krinsky, IEEE Trans. Nucl. Sci. NS-30(1983)3078.

[13] P. Elleaume, Rev. Sci. Instrum. 63(1992)321.

[14] K. J. Kim, Proc. US Particle Accelerator Summer School (1986).

[15] B. M. Kincaid, J. App. Phys. 48(1977)2684.

[16] for example, L. D. Landau and E. W. Lifshitz, *The Classical Theory of Fields*, (Pergamon, Oxford, 1971)

[17] K. Halbach, Nucl. Instrum. Meth. 169(1980)1.

[18] K. Halbach, Nucl. Instrum. Meth. 187(1981)109.

[19] K. Halbach, K. Chin, J. Hoyer, E. Winick, H. Cronin, R. Yang, IEEE Trans. Nucl. Sci. NS-28(1981)3136.

[20] K. Halbach, J. Physique, C1(1983)211.

[21] for example, E. Wolf and W. Born, *Principles of Optics*, (Pergamon, Oxford, 1970)

[22] M. B. Moissev, M. N. Nikitin and N. I. Fedosev, Sov. Phys. J. 21(1978)232.

[23] K. J. Kim, Nucl. Instrum. Meth. 219(1984)425.

[24] J. Bahrdt, A. Gaupp, W. B. Peatman, F. Schäfers and Ch. Wang, Proc. SPIE 2010(1993)168.

[25] B. W. Batterman and D. H. Bilderback, X-ray monochromators and mirrors, chap. 4 in: *Handbook on Synchrotron Radiation*, eds. G. S. Brown and D. E. Moncton (North-Holland, Elsevier, The Netherlands, 1991)

[26] H. Kitamura, Jpn. J. Appl. Phys. 19(1980)L185.

[27] P. Elleaume, Nucl. Insturm. Meth. A291(1990)371.

[28] B. Diviacco and R. P. Walker, Nucl. Instrum. Meth. A292(1990)517.

[29] S. Sasaki, K. Miyata and T. Takada, Jpn. J. Appl. Phys. 31(1992)L1796.

[30] X. M. Maréchal, T. Tanaka and H. Kitamura, Rev. Sci. Instrum. 66(1995)1937.

[31] S. Kimura, M. Kamada, H. Hama, X. M. Maréchal, T. Tanaka and H. Kitamura, Proc. Int. Conf. VUV'95 (VUV11), to be published.

[32] C. Germain, Nucl. Instrum. Meth. 21(1963)17.

[33] T. R. McGuire and R. I. Potter, IEEE Trans. Mag. 11(1975)1018.

[34] A. Schuhl, F. Nguyen Van Dau and J. R. Childress, Appl. Phys. Lett. 66(1995)2751.

[35] J. M. Ortega, C. Bazin, D. A. G. Deacon, C. Depauteix, P. Elleaume, Nucl. Instrum. Meth. 206(1983)281.

[36] R. P. Walker, M. W. Pool, D. G. Taylor, J. Physique, C1(1984)321.

[37] X. M. Maréchal, J. Chavanne and P. Elleaume, ESRF internal report, SR/ID-90-37.

[38] E. T. Scharlemann, J. Appl. Phys., 58(1985)2154.

[39] M. Takabe, M. Ogoshi, M. Marushita, H. Sakae, K. Araki, S. Mandai, T. Keishi and A. Kobayashi, Nucl. Instrum. and Meth. A331(1993)736.

[40] Y. Wasa, T. Suzuki, T. Kusaka, K. Inoue, Y. Kawata, A. Kobayashi and T. Keishi, Nucl. Instrum. and Meth. A331(1993)715.

[41] P. Elleaume, ESRF internal report, SR/ID-89-33.

[42] M. Sands, Proc. Int. School "Enrico Fermi", 1971.

[43] V. Garczynski, Nucl. Instrum. Meth., A324(1993)7.

[44] J. Goulon, P. Elleaume and D. Raoux, Nucl. Instrum. Meth., A254(1987)192.

[45] S. Yamamoto and H. Kitamura, Jpn. J. App. Phys., 26(1987)L1613.

[46] S. Yamamoto, T. Shioya, S. Sasaki and H. Kitamura, Rev. Sci. Instrum., 60(1989)2672.

[47] H. Kitamura and S. Yamamoto, Rev. Sci. Instrum., 63(1992)1104.

[48] J. Chavanne and P. Elleaume, Synchrotron Radiation News 8(1995)18.

[49] M. Furman, J. Byrd and S. Chattopadhyay, Beam Instabilities, chap. 12 in: *Synchrotron Radiation Sources - A Primer*, ed. H. Winick (World Scientific, Singapore, 1994)

[50] S. Yamamoto, T. Shioya, M. Hara, H. Kitamura, X. W. Zhang, T. Mochizuki, H. Sugiyama and M. Ando, Rev. Sci. Instrum. 63(1992)400.

List of Publications

Chapter 3

[1] T. Tanaka and H. Kitamura, "Figure-8 undulator as an insertion device with linear polarization and low on-axis power density", Nucl. Instrum. and Meth. A364(1995)368

Chapter 4

[2] T. Tanaka and H. Kitamura, "Characteristics of figure-8-undulator radiation", J. Electron Spectroscopy and Related Phenomena, in press.

[3] T. Tanaka and H. Kitamura, "Analysis of figure-8-undulator radiation", J. Synchrotron Radiation, 3(1996)47

Chapter 5

[4] X. M. Maréchal, T. Tanaka and H. Kitamura, "An elliptical wiggler for SPring-8", Rev. Sci. Instrum. 66(1995)1937

[5] S. Kimura, M. Kamada, H. Hama, X. M. Maréchal, T. Tanaka and H. Kitamura, "Design of a helical undulator for UVSOR", J. Electron Spectroscopy and Related Phenomena, in press.

Chapter 6 and 7

[6] T. Tanaka and H. Kitamura, "A novel insertion device for circularly polarized radiation", submitted to J. Synchrotron Radiation.

Others

[7] T. Tanaka, T. Awata, A. Itoh, N. Imanishi, T. Yamanaka, M. Oyamada, S. Urawasa and T. Nakazato, "Resonance effects of transition radiation emitted from thin-foil stacks", Nucl. Instrum. and Meth. B93(1994)21

[8] M. Yamamoto, T. Fujisawa, M. Nakasako, T. Tanaka, T. Uruga, H. Kimura, H. Yamaoka, Y. Inoue, H. Iwasaki, T. Ishikawa, H. Kitamura and T. Ueki, "Conceptual design of SPring-8 contract beamline for structural biology", Rev. Sci. Instrum., 66(1995)1833

[9] A. Itoh, N. Imanishi, F. Fukuzawa, N. Hamamoto, S. Hanawa, T. Tanaka, T. Ohdaira, M. Saitoh, Y. Haruyama and T. Shirai, "Single-, double- and triple-electron capture cross sections for multicharged slow carbon ions in H_2, CH_4, C_2H_6 C_3H_8 and CO_2 molecules", J. Phys. Soc. Jpn., 64(1995)3255

[10] T. Awata, K. Yajima, T. Tanaka, M. Imai, A. Itoh, N. Imanishi, M. Oyamada, S. Urasawa, T. Nakazato, K. Yoshida, K. Nakayama and A. P. Potylitsin, "Resonance effects of transition radiation emitted from thin foil stacks using electron beam", Radiation Physics and Chemistry, to be published.